Infrared Analysis of Dusty Plasmas and
Finite Dust Clusters Under Strong Magnetic Fields

I n a u g u r a l d i s s e r t a t i o n

zur

Erlangung des akademischen Grades eines

Doktors der Naturwissenschaften
(Dr. rer. nat.)

der

Mathematisch-Naturwissenschaftlichen Fakultät

der

Universität Greifswald

vorgelegt von

Harald Robert Krüger

Greifswald, den 7. September 2021

Dekan:	Prof. Dr. Gerald Kerth
1. Gutachter:	Prof. Dr. André Melzer
2. Gutachter:	Prof. Dr. Jan Benedikt
Tag der Promotion:	1. Dezember 2021

Contents

1 Introduction

Dusty plasmas occur in different types and shapes, from astrophysical phenomena [1–6] like in the rings of Saturn and Jupiter, to the manufacturing of semiconductors [7–9]. Dusty plasmas consist of nano- to micrometric particles in addition to the neutral gas atoms, electrons and ions of a regular plasma [10–14]. Due to the flux of electrons and ions, the particles most often gain a negative charge and hence, interact strongly with each other and the other plasma species. The scientific investigation of laboratory dusty plasmas began in the 1990s with the discovery of the plasma crystal [15–17].

The interaction of particles, ions and electrons is mainly influenced by the particle charge, making it one of the most important properties of a dusty plasma. In this thesis a novel charge diagnostic based on the infrared absorption properties of the particles has been developed. Moreover, charge measurements at various magnetic field strengths have been performed. To experimentally determine the dust charge, the interaction of the particles with each other or with external perturbations has usually been exploited. The dust charge then is revealed from the particle dynamics, i.e. particle positions and velocities are necessary. One of the first developed charge diagnostics for single micrometric particles, the resonance method, relies on the response of the particles to an external perturbation [18–21]. For spatially extended systems that support waves, the dispersion relation of the waves can be used to analyze the particle charges [22–25].

The charge in nanodusty plasma experiments is of high interest, because often high particle densities occur in nanodusty plasmas. Due to the high density, a large amount of the electrons from the plasma can be bound to the particles and hence, the electron density is reduced in the surrounding plasma. This results in reduced electron currents to the particles and hence, reduced particle charges [26–28]. In nanometric dusty plasmas, single-particle tracking is not possible, but a measurement of the dust charge is possible by investigation of dust-density wave properties [29]. Nevertheless, in the absence of waves, a new method to determine the dust charge is necessary.

In thesis article A1, I aim to investigate the suitability of an optical resonance as a charge diagnostics. Heinisch et al. suggested to use the charge dependent phonon resonance of the dust material to determine the charge [30, 31]. In their work, Heinisch et al. presented calculations for a variety of materials exhibiting this resonance in the infrared wavelength range. In their calculations, surplus charges on the particles caused a shifting of the resonance towards higher wavenumbers.

First of all, a suitable particle material has to be found that exhibits the charge-dependent resonance in a wavenumber range suitable for an IR spectrometer. In addition, the material needs to be available in form of nanoparticles. IR spectroscopic diagnostics are no common diagnostics in the dusty plasma community. Hence, the question arises, whether an experimental setup can be built that confines enough dust particles in the line of sight to measure a significant absorption and hence, allows an investigation of the

dusty plasma with an IR spectrometer. Is it possible to detect a shift of the resonance? And can a particle charge be derived from such a measurement?

In dusty plasma experiments micrometric particles made of melamine-formaldehyde (MF) are standard [32–34]. Spherical MF particles are available in a large range of sizes. However, it has been reported that particles shrink and the surfaces become rougher under plasma exposition [21, 34–36]. This happens not only in reactive discharges with gases like oxygen but also with inert gases like argon. The analysis of the chemical structure of the particles is of interest. In thesis article A2, I discuss the suitability of FTIR spectroscopy to investigate the chemical structure of MF particles under plasma exposition. Recently, the influence of the temperature on MF particles has been investigated in non-plasma environments [37, 38], where changes in the chemical structure have been found. In thesis article A2, the influence of the temperature on the changes in the chemical structure during plasma exposure will be studied. With this analysis, the question whether the temperature in the plasma causes the changes in the chemical structure or additional processes like plasma etching are the reason for the behavior is to be investigated.

In thesis article A3, the particle charge under strong magnetic fields will be explored. In plasmas with strong magnetic fields, ions and electrons are magnetized, while micrometric dust particles are not directly influenced by the magnetic field [39–42]. Since the charging of dust particles in the plasma depends on the electron and ion fluxes onto the particles, an experimental investigation of the influence of the magnetic field on the particle charge is of high interest. From the particle-particle interaction in finite dust systems the charge can be measured [43–47]. First of all, I want to find out whether the cluster behaves similarly under strong magnetic fields as without magnetic fields and whether the normal modes of the cluster can be retrieved. There, we want to focus on the magnetic fields where electrons and ions magnetize and see if the behavior of the cluster or the particle charge exhibit changes at these neuralgic fields.

In a first part of this thesis, the fundamental principles of dusty plasma physics will be discussed. The experimental setup and the diagnostics will be introduced in Chapt. 3. The results of the thesis articles A1-A3 are given in Chapt. 4. A short summary of the results is found in Chapt. 5.

2 Physics Basics

This dissertation mainly deals with particles confined in a plasma environment. Plasma physics offers a vast range of different types, from hot fusion plasmas to low temperature plasmas. This chapter will give an insight into the physical background of low-temperature radio frequency (rf) plasmas with a focus on dusty plasmas. In addition, an introduction into Mie scattering for the purpose of a charge diagnostic is given.

2.1 Plasma

Following Irving Langmuirs suggestion from 1928, an ionized gas with free electrons and ions with a collective behavior is called a plasma [48]. One of the most important characteristics of plasmas is the quasineutrality meaning balanced charges. In a simple plasma containing only one ion species with a charge of one elementary charge ($q = +e$), the quasineutrality can be described as

$$n_\mathrm{e} = n_\mathrm{i} \tag{2.1}$$

with the electron density n_e and the ion density n_i [14]. Collective behavior can be seen, e.g., when a test charge $+Q$ is added to the plasma. The electrons and ions shield the test charge resulting in a reduced Coulomb interaction. Then, the potential of the test charge $\Phi(r)$ at the distance r can be described as

$$\Phi(r) = \frac{Q}{4\pi\varepsilon_0 r}\exp(-r/\lambda_\mathrm{D}) \tag{2.2}$$

with the dielectric constant ε_0 and the shielding constant λ_D which is called Debye length. This Debye length is defined for the different species by

$$\lambda_{\mathrm{D}_k} = \sqrt{\frac{\varepsilon_0 k_\mathrm{B} T_k}{n_k e^2}} \ , \tag{2.3}$$

where the different species are k = e,i for electrons and ions and with the Boltzmann constant k_B and the kinetic temperature T_k. For typical radio frequency (rf) discharges the electron Debye length is of the order of $\lambda_\mathrm{De} \approx 500\,\mu\mathrm{m}$ and the ion Debye length is about a tenth of this, $\lambda_\mathrm{Di} \approx 50\,\mu\mathrm{m}$[1].

The response time of an electron or ion to reach its equilibrium position after an external perturbation, e.g. a test charge has entered the system, can be estimated as the ratio of Debye length and thermal velocity $v_k \approx \sqrt{k_\mathrm{B} T_k/m_k}$ with the mass of the particle

[1] In low temperature plasma rf discharges, typical values for the temperatures are $T_\mathrm{e} = 2.5\,\mathrm{eV}$, $T_\mathrm{i} \approx 300\,\mathrm{K}$ and for the densities $n_\mathrm{e} \approx n_\mathrm{i} \approx 5 \cdot 10^{14}\,\mathrm{m}^{-3}$.

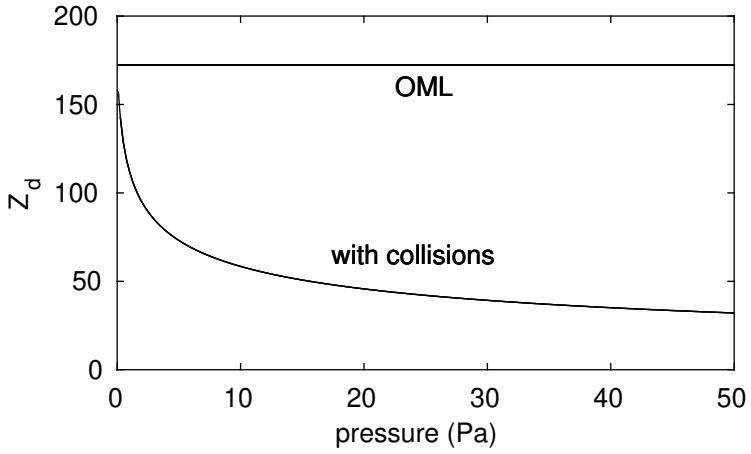

Figure 2.1: Charge of a particle of 40 nm radius in dependence of the argon gas pressure following the OML model and the advanced collision model by Khrapak et al. [49]. The used parameters are $T_e = 2.5\,\mathrm{eV}$, $T_i = 300\,\mathrm{K}$, $n_e = n_i = 5 \cdot 10^{14}\,\mathrm{m}^{-3}$ and $\phi_{fl} = -2.4\,\mathrm{V}$ in the OML case [50].

m_k. Due to the higher mass of the ions, this response time is far longer for ions than for electrons. The reciprocal of this response time is called the plasma frequency [14]

$$\omega_{\mathrm{P}_k} = \sqrt{\frac{n_k e^2}{\varepsilon_0 m_k}} \ . \tag{2.4}$$

In low temperature plasma discharges, the plasma frequency typically is of the order of GHz for electrons and a few MHz for argon ions. When rf plasma discharges are used, a usual driving frequency is $f_{\mathrm{RF}} = 13.56\,\mathrm{MHz}$. With this frequency lying between the electron plasma frequency and the ion frequency, electrons can follow the electric field in each rf period. This way, electrons are heated and gain temperatures far above room temperature. In contrast, the ions only react to the time averaged electric field and do not heat up considerably.

In dusty plasmas, the plasma not only consists of electrons, ions and neutral gas atoms, but also of an additional species of particles in the range from nanometers to a few micrometers. Due to the flux of electrons and ions onto the particles, the particles gain a charge and hence, are interacting with each other, ions and electrons via the shielded coulomb interaction and with external electric fields via the electric field force. In analogy to the electrons and ions, the dust particles have a plasma frequency

$$\omega_{\mathrm{P_d}} = \sqrt{\frac{Q_\mathrm{d}^2 n_\mathrm{d}}{\varepsilon_0 m_\mathrm{d}}} \tag{2.5}$$

with the particle charge Q_d, the particle number density n_d and the particle mass m_d. Depending on the size and mass of the particles, the frequency ranges from only 1 Hz to about 100 Hz.

2.2 Particle Charge

As mentioned before, the charge of the particles Q_d is of major relevance for the behavior of the particles in the plasma environment. Hence, we will now take a deeper look into

the charging mechanism of the dust particles. In the plasma environment, a particle is exposed to the flux of electrons and ions. The potential ϕ_{fl} at which both fluxes I_k are equal is called the floating potential [14, 51]

$$\sum_k I_k(\phi_{\mathrm{fl}}) = \frac{\mathrm{d}Q_{\mathrm{d}}}{\mathrm{d}t} = 0 \ . \tag{2.6}$$

To determine the charge, we have to investigate the fluxes on the particle. The standard approach by Mott-Smith and Langmuir for this investigation is called the *orbital motion limit* (OML) model [52]. First, we consider the electrons and ions to be of a Maxwellian velocity distribution that interact collisionless via the Coulomb potential of the dust particle. Exploiting the conservation of energy and momentum, the ion flux can be determined as

$$I_{\mathrm{i}} = \pi a^2 n_{\mathrm{i}} e \sqrt{\frac{8 k_{\mathrm{B}} T_{\mathrm{i}}}{\pi m_{\mathrm{i}}}} \left(1 - \frac{e\phi_{\mathrm{fl}}}{k_{\mathrm{B}} T_{\mathrm{i}}}\right) \tag{2.7}$$

with the radius of the particle a. Keeping in mind that the particles gain a negative charge in the first place due to the higher mobility of the electrons, the electron flux onto the particle is limited to fast electrons that can reach the negatively charged particle against the repulsive Coulomb interaction,

$$I_{\mathrm{e}} = -\pi a^2 n_{\mathrm{e}} e \sqrt{\frac{8 k_{\mathrm{B}} T_{\mathrm{e}}}{\pi m_{\mathrm{e}}}} \exp\left(\frac{e\phi_{\mathrm{fl}}}{k_{\mathrm{B}} T_{\mathrm{e}}}\right) \ . \tag{2.8}$$

This model assumes a Maxwellian velocity distribution for the electrons and ions as well as collisionless ion trajectories which is often not given in plasma discharges [50]. When dealing with plasmas at typical gas pressures especially ion-neutral charge exchange collisions influence the ion flux onto the particle significantly. Fast ions, that would pass by the particle without being collected, collide with neutrals from the background gas. In this collision, the ions lose kinetic energy and are accelerated towards the particle, then. This increases the ion flux onto the particle. With increasing gas pressure the mean free path l_{mfp} of the ions decreases, and hence, more ion-neutral collisions occur, resulting in a stronger ion flux. This effect can be attributed by an additional term in the ion flux as [49, 53]

$$I_{\mathrm{i}} = \pi a^2 n_{\mathrm{i}} e \sqrt{\frac{8 k_{\mathrm{B}} T_{\mathrm{i}}}{\pi m_{\mathrm{i}}}} \left(1 - \frac{e\phi_{\mathrm{fl}}}{k_{\mathrm{B}} T_{\mathrm{i}}} + 0.1 \left(\frac{e\phi_{\mathrm{fl}}}{k_{\mathrm{B}} T_{\mathrm{i}}}\right)^2 \frac{\lambda_{\mathrm{D}}}{l_{\mathrm{mfp}}}\right) \ . \tag{2.9}$$

The floating potential can now be acquired by numerically equalizing the electron and ion currents for given ion and electron densities, temperatures and masses. To obtain a particle charge from the potential, the particle is treated as a capacitor with the capacitance $C = 4\pi\varepsilon_0 a$ for particle radii $a \ll \lambda_{\mathrm{D}}$ which is usually given [54]. The charge then results in

$$Q_{\mathrm{d}} = Z_{\mathrm{d}} e = 4\pi\varepsilon_0 a \phi_{\mathrm{fl}} \tag{2.10}$$

where Z_{d} is the charge number. As can be seen, the charge linearly depends on the particle radius a. To put both the basic OML model and the advanced model containing ion-neutral collisions into perspective typical charges in dependence of the gas pressure

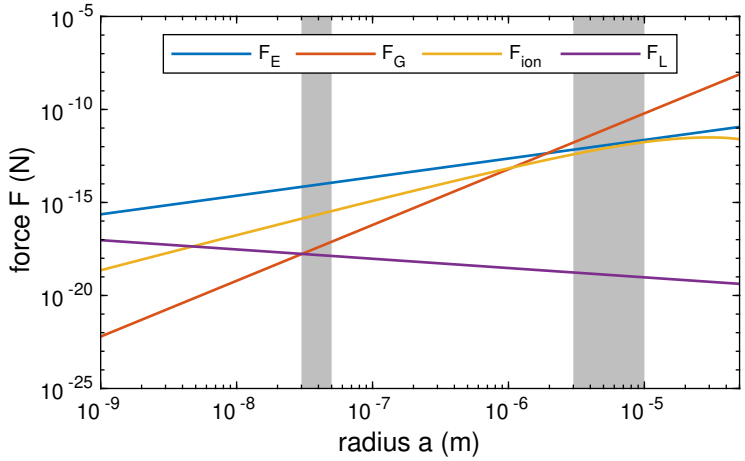

Figure 2.2: Overview of the forces acting on the dust particles inside an argon plasma in dependence of the particle radius. The highlighted areas represent the ranges of particle sizes used in this thesis. The following parameters have been used: $E = 1000\,\mathrm{V/m}$, $\rho_\mathrm{d} = 1500\,\mathrm{kg/m^3}$, $T_\mathrm{e} = T_\mathrm{i} = 1\,\mathrm{eV}$, $v_{\mathrm{th_i}} = u_\mathrm{i} = 400\,\mathrm{m/s}$, $T_\mathrm{d} = 300\,\mathrm{K}$ and $B = 1\,\mathrm{T}$.

are calculated and shown in Fig. 2.1. For a particle of 40 nm radius in an argon discharge the charge can be estimated to be about 170 elementary charges using the OML model. Taking collisions into account, the charge number becomes significantly lower and reaches $Z_\mathrm{d} \approx 60$ at a gas pressure of 10 Pa and $Z_\mathrm{d} \approx 40$ at a gas pressure of 50 Pa. For low pressures $p < 10\,\mathrm{Pa}$, the charge number rapidly increases towards the charge number estimated by the OML model.

Besides the ion-neutral collisions there are a few other mechanisms influencing the charge on the particle, e.g. secondary electron emission by the impact of fast electrons [55], streaming ions in the plasma sheath [56] or photoelectron emission by UV absorption [2]. These mechanisms are of minor interest for this dissertation and, hence, will not be discussed in detail.

2.3 Forces on the Dust Particles

There is a variety of forces acting on the particles in a plasma environment. Here, a short overview of the most relevant forces will be given.

Electric Field Force The electric field in the plasma and also possible external electric fields interact with the charge of the particles via the electric field force

$$\vec{F}_\mathrm{E} = Q_\mathrm{d} \cdot \vec{E} = 4\pi\varepsilon_0 a \phi_\mathrm{fl} \vec{E} \ . \tag{2.11}$$

Due to the linear dependence of the charge on the particle radius a, also the electric field force depends linearly on the particle radius.

Gravitational Force The particles are also subject to the gravitational force. The mass m of a particle scales with the third power of the radius and hence, so does the gravitational force

$$\vec{F}_\mathrm{G} = m \cdot \vec{g} = \frac{4}{3}\pi a^3 \rho_\mathrm{d} \vec{g} \tag{2.12}$$

with the particle mass density ρ_d and $\vec{g}$ being the gravitational acceleration.

Ion Drag Force Another force acting on the particles is the ion drag force caused by ions streaming past a (negatively charged) dust particle. The high ionization rate at the center of a discharge and the resulting ion density gradient causes a diffusion process towards the outer parts of the plasma. These streaming ions interact with the dust particles in two ways. The first interaction is the direct collision where the streaming ions transfer their momentum to the dust. Depending on the ions' thermal velocity $v_{\mathrm{th_i}}$ and the ions' drift velocity u_i according to Barnes et al., this part of the ion drag force can be written as [57]

$$\vec{F}_\mathrm{dir} = \pi a^2 m_\mathrm{i} v_\mathrm{s} n_\mathrm{i} \left(1 - \frac{2e\phi_\mathrm{fl}}{m_\mathrm{i} v_\mathrm{s}^2}\right) \cdot \vec{u}_\mathrm{i} \tag{2.13}$$

where $v_\mathrm{s} = \sqrt{v_{\mathrm{th_i}}^2 + u_\mathrm{i}^2}$ is the mean velocity of the ions. The second part of the ion drag force is due to the Coulomb interaction of the passing ions whose trajectories are deflected in the field of the dust. The ions drag the particle in the direction of the ion flow. This Coulomb part of the ion drag force can be described by

$$F_\mathrm{C} = \frac{2\pi a^2 e^2 \phi_\mathrm{fl}^2}{m_\mathrm{i} v_\mathrm{s}^3} n_\mathrm{i} \vec{u}_\mathrm{i} \ln\left(\frac{\lambda_\mathrm{D}^2 + b_{\pi/2}^2}{b_\mathrm{c}^2 + b_{\pi/2}^2}\right) \tag{2.14}$$

with the impact parameter for 90° deflection $b_{\pi/2} = ae\phi_\mathrm{fl}/m_\mathrm{i} v_\mathrm{s}$ and the critical impact parameter [57]

$$b_\mathrm{c}^2 = a^2 \left(1 - \frac{2e\phi_\mathrm{fl}}{m_\mathrm{i}\, v_\mathrm{s}^2}\right) \quad . \tag{2.15}$$

The total ion drag force is then given by

$$\vec{F}_\mathrm{ion} = \vec{F}_\mathrm{dir} + \vec{F}_\mathrm{C} \quad . \tag{2.16}$$

For small ion drift velocities, the Coulomb part is dominant. When the ion drift velocity exceeds the thermal velocity by a factor of about 10, the direct impact part is getting more dominant since the interaction time of the passing ions becomes too short to significantly contribute to the ion drag. However, the simplified model by Barnes et al. presented here [57] neglects some effects: only Coulomb collisions within one Debye length are considered while ions interact with the highly charged particle over far longer distances. In addition, the velocity combination of drift and thermal term needs to be described by a shifted Maxwellian distribution. These factors have been accounted for by the advanced models of Khrapak et al. [58] and Hutchinson [59]. Nevertheless, the general trend of the ion drag force with the velocity for the mentioned models is quite similar. Additionally it is reasonable to mention the dependence of the ion drag force on the second power of the radius.

Lorentz Force In the presence of a magnetic field, the interaction of the particle charge with this field $\vec{B}$ becomes interesting. In general, the Lorentz force acts perpendicular to the velocity $\vec{v}_\mathrm{d}$ of the particles and the magnetic field,

$$\vec{F}_\mathrm{L} = Q_\mathrm{d} \vec{v}_\mathrm{d} \times \vec{B} = 4\pi\varepsilon_0 a \phi_\mathrm{fl} \vec{v}_\mathrm{d} \times \vec{B} \quad . \tag{2.17}$$

Just as the electric field force, the Lorentz force scales linearly with the particle radius.

Particle confinement As mentioned before, the variety of forces acting on the particles scale differently with the particle radius. To get a sense of this behavior, the forces are shown over a wide range of particle radii for typical low temperature rf discharges in Fig. 2.2. In addition to the forces the ranges of particle radii discussed in this thesis are marked: A range around 40 nm radius where the electric field force is predominant and the gravitational force only plays a minor role, and a range from 3 µm to 10 µm where the gravitational force is dominating while ion drag force and electric field force are of the same order of magnitude, but much smaller. As can be seen, the Lorentz force induced by a magnetic field is negligible for both highlighted ranges of particle radius. However, there is an indirect influence of the magnetic field on the particles in dusty plasmas which will be discussed in the next section.

Due to the unequally strong forces on to the particles, the confinement of the particles is different for the two size ranges. In the nanometer range, the particles are distributed over the whole plasma volume. In the micrometer range, the gravitational force is dominant and hence, the particles find a stable position in the sheath region of the plasma where gravitational and electric field force are equal.

Additional forces Additional forces on the particles that can occur in dusty plasmas are the neutral drag force [60], the thermophoretic force as a result of a temperature gradient [61] and forces induced by laser manipulation [62]. However, these forces do not play a major role in this present thesis.

2.4 Particles in Magnetic Fields

The Lorentz force is not a dominant force in dusty plasmas with magnetic fields with up to 5 T and hence, the dynamics of the dust particles is barely influenced by the magnetic field due to the Lorentz force. However, the presence of a magnetic field still causes changes in the behavior of the dust particles [11, 12, 41, 63–68]. Therefore, it is necessary to consider the electron and ion components of the dusty plasma and check their interaction with the magnetic field. To indicate the strength of the interaction with the magnetic field, two parameters can be used: First, the Hall parameter puts the Lorentz force and friction timescale into relation,

$$h_k = \frac{\omega_{\mathrm{c}_k}}{\nu_{\mathrm{n}_k}} \ , \tag{2.18}$$

resulting in the ratio of the cyclotron frequency ω_{c_k} and the collision frequency with the neutral gas background ν_{n_k} of the species k = e,i,d. When the Hall parameter becomes larger than one, meaning that the particle can perform one gyro-orbit without colliding with the background gas, effects of the magnetic field are considered to become observable [40].

A second measure for the influence is given by the magnetization

$$M_i = \frac{\omega_{\mathrm{c}_k}}{\omega_{\mathrm{p}_k}} \ , \tag{2.19}$$

putting both the cyclotron frequency and the plasma frequency into relation. With this parameter collective modes can be classified and described [69]. It is sufficient to apply magnetic fields of a few milliteslas to magnetize the electrons ($h_\mathrm{e} > 1$, $M_\mathrm{e} > 1$). To

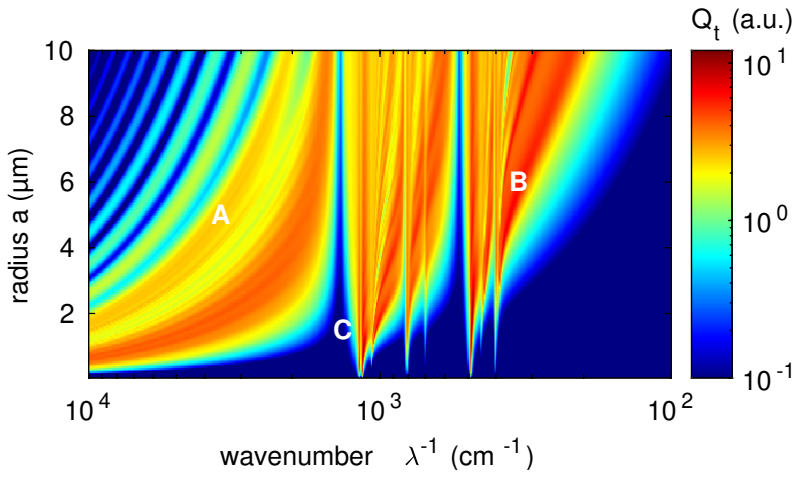

Figure 2.3: Calculated extinction efficiency Q_t of SiO_2 particles at different particle radii and wavenumbers of the incident light. Three different features occur: (A) ripple and interference structure, (B) ordinary and (C) anomalous resonances. The calculations have been made in analogy to Ref. [31], using notations and optical constants of SiO_2 from Refs. [78–83].

magnetize the ions, magnetic fields of the order of a few hundred milliteslas have to be applied and to magnetize nanometric dust particles magnetic fields of at least 5 T are necessary. For larger dust particles even higher fields have to be used. However, superconducting magnets to produce such high fields are not easily available. Nevertheless, due to the magnetized electrons and ions at fields of up to 5 T, the ion and electron dynamics is altered compared to plasmas without magnetic fields. For example, a slow rotation of the dust cloud is excited at low magnetic fields due to the Hall component of the streaming ions [39, 70, 71]. For stronger magnetic fields up to a few Teslas, experiments and simulations showed ion-induced wakefields [64, 72, 73] as well as filamentation [63, 74, 75] and structures imposed from the electrode [76, 77].

2.5 Light Scattering by Charged Particles

The scattering of light by small particles is described by Mie theory as a solution of Maxwell's equations [84–86]. The scattering behavior of the particles mainly depends on the relation of the size of the particles and the wavelength of the incident light. For small particle radii compared to the wavelength, the scattering intensity strongly depends on the wavelength. This regime is called the Rayleigh regime. In the range where particle radius and wavelength are of the same order, the so called Mie regime, radially distributed oscillations of the scattering intensity occur which are sensitive to the particle radius. For larger particles compared to the wavelength, the solutions of Mie theory result in geometric optics. In this thesis I will now focus on the charge dependence of the particles' scattering behavior.

The light scattering behavior of spheres in the infrared spectral range can show charge dependent phonon resonances, as calculations from Heinisch et al. have indicated [30, 31]. In their work, they pointed out that this phenomenon could be a novel approach to determine the particle charge in dusty plasmas. The effect arises when the surplus electrons on a particle cause a charge dependent polarizability $\alpha(\omega)$. This polarizability

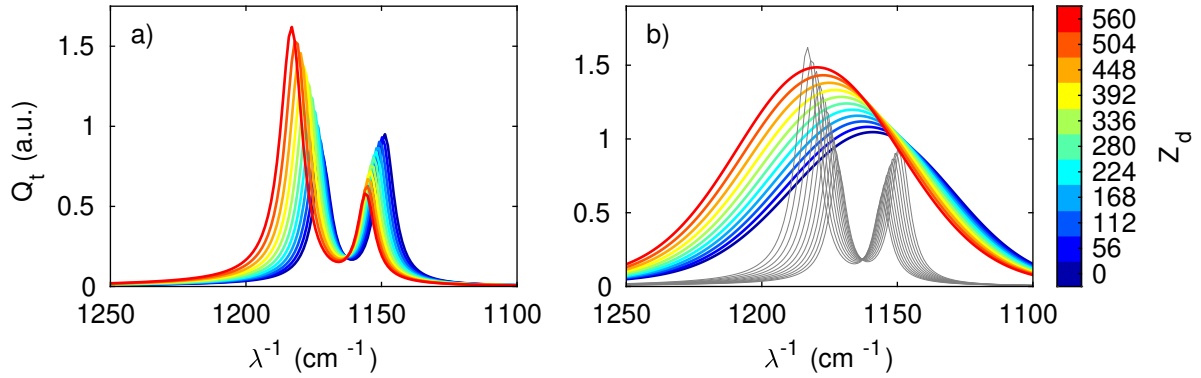

Figure 2.4: a) Extinction efficiency Q_t of two phonon resonances of SiO_2 nanoparticles ($a = 40\,\mathrm{nm}$) for different numbers of elementary charges on the particle. b) Convolution of the extinction efficiency from a) and a Gaussian to compensate particle size and density distributions and material inhomogeneities.

enters the refractive index

$$N = \sqrt{\epsilon(\omega) + \alpha(\omega)} \ , \tag{2.20}$$

where ϵ is the dielectric function of the sphere and ω the light frequency. The dielectric function is specific to each single material and hence, needs to be calculated individually for every material. These calculations have been done for a variety of different materials like PbS, LiF, MgO, Cu_2O and Al_2O_3. All of these show a shifting of the phonon resonance towards higher wavenumbers with increasing particle charges. However, for experiments those materials cannot be used easily. Either the absolute wavenumber position of the phonon resonances are in the range where usual FTIR spectrometers can barely operate (PbS, LiF, MgO, Cu_2O) or the material itself is hard to obtain in form of nano- or microparticles (α-Al_2O_3, [87]). Nevertheless, from our experiments we found silica (SiO_2) particles to be suitable, thus we look into the scattering behavior of SiO_2, here. In this work, I performed the calculation of the IR absorption features of such silica particles, as it has been found that the phonon resonance of this material is in a useful wavenumber range and the material is commercially available in form of nanoparticles.

In analogy to the approach by Heinisch et al. [30, 31] calculations of the extinction efficiency for different wavenumbers and silica particle radii have been performed, see thesis article A1 (Sec. 6.3). For that, we have used optical constants of SiO_2 given in Refs. [78–81] and notations from Refs. [82, 83]. The calculated extinction efficiency Q_t of SiO_2 is shown in Fig. 2.3. We see different features in this scattering behavior: Above wavenumbers of $\lambda^{-1} > 1.5 \cdot 10^3\,\mathrm{cm}^{-1}$ and hence, above the highest transverse optical (TO) phonon frequency, a typical ripple and interference structure of Mie scattering can be seen [31, 85] (marker A), as well as ordinary (marker B) and anomalous (marker C) resonances below the TO phonon frequency. Especially the anomalous resonances have been reported to be strongly sensitive to surplus electrons on the particles for other materials. We now check for this effect with SiO_2 and hence, focus on the charge dependency of this third feature in the scattering behavior of the SiO_2 particles (marker C).

Taking different charge numbers of the particles into account, the charge dependent extinction efficiency is calculated. Figure 2.4 shows this extinction efficiency for a particle of 40 nm radius in the wavenumber range of the two anomalous resonances with highest energies. The two resonances both shift towards higher wavenumbers with increasing particle charge. This shift is about $20\,\mathrm{cm}^{-1}$ for the resonance at $1180\,\mathrm{cm}^{-1}$ and about

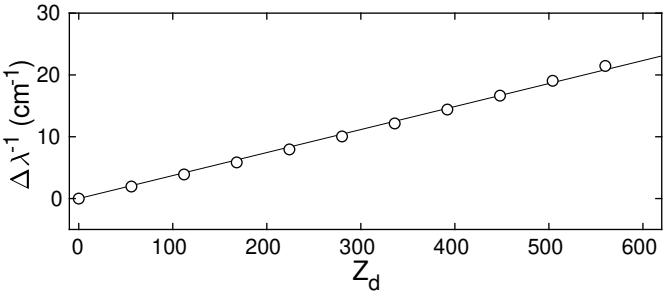

Figure 2.5: Calculated shift of the convoluted absorption peaks in dependence of the particle charge. The line indicates a linear fit to the shift.

$10\,\mathrm{cm}^{-1}$ for the resonance at $1150\,\mathrm{cm}^{-1}$. Hence, a shift of the resonances can be confirmed in analogy to the other materials mentioned before. The order of this shift differs for different particle sizes and the corresponding particle charges. For micron sized particles, this shift becomes indistinguishable on the one hand and the resonances itself are getting broader and overlap more strongly with neighboring resonances on the other hand, see Fig. 2.3. Therefore, it is reasonable to use small, nanoscaled particles, where the resonance shifts strong enough to be detectable.

However, in addition to the shift of the resonance, we found that the absolute amplitude changes with the charge as well. While the amplitude of the higher energetic resonance increases, the amplitude of the lower energetic resonance decreases with increasing particle charge, see Fig. 2.4a).

In the experiment, only one broad resonance has been detected, see Sec. 4.1. Hence, taking into account uncertainties like a particle size and charge distribution as well as material inhomogeneities broadening the signal, it seems reasonable to also consider this in the calculation. Therefore, the calculated extinction efficiency is convoluted with a rather broad Gaussian curve. This results in one broad absorption peak, see Fig. 2.4b). Using this convoluted absorption, the shift of the calculated signal can be determined with regard to the signal of uncharged particles, see Fig. 2.5. The shift $\Delta\lambda^{-1}$ of the signal increases nearly linearly with increasing particle charge Z_d. A linear fit to the calculated shifts can then be used to retrieve charges from the measurements. For details, see thesis article A1.

3 Experimental Setup and Diagnostics

In the context of this thesis two major experimental setups have been used: One setup where the discharge chamber has been integrated into the beam path of an FTIR spectrometer for optical diagnostics in the infrared wavelength range to measure the IR response of the particles in the plasma and one setup where the plasma chamber has been integrated in the bore of a superconducting magnet to measure the charging of dust particles under strong magnetic fields.

3.1 FTIR Experiment

The two used setups consist of two different plasma chambers designed and adapted for the used diagnostics and surrounding environment. For the experiments described in thesis articles A1 and A2 (Secs. 6.2 and 6.3), the plasma chamber has been integrated into the beam path of an FTIR spectrometer, see Fig. 3.1. To obtain sufficient absorption from the particles confined in the plasma using the spectrometer, a rather long interaction length is useful. Hence, a plasma chamber with an inner diameter of 400 mm and an electrode of 300 mm diameter has been chosen. This size is rather large compared to typical dusty plasma setups where the electrode usually only has a diameter of the order of 100 mm [88–90]. Due to the large size of the chamber the FTIR beam has to be decoupled from the spectrometer and an external detector is used. Nevertheless, the internal sample compartment can still be used for measurements of dust samples not exposed to the plasma. The whole optical path of the FTIR spectrometer including the internal sample compartment is evacuated to reduce impurities in the line of sight by ambient air and water.

The plasma chamber is evacuated to base pressures of about 10^{-4} Pa. Operation gas pressures are of the order of $1 - 100$ Pa. The plasma is driven as an asymmetric rf discharge with one powered electrode at 13.56 MHz. In experiments with microparticles, an additional potential barrier is placed on the electrode to confine as many particles in the line of sight of the FTIR as possible. In contrast, the experiments with nanoparticles are carried out with an additional grounded electrode with a diameter of 200 mm in a distance of 35 mm above the powered electrode, but without the potential barrier. For the different particle species, different methods for immersion of the dust in the discharge are used. The microparticles are inserted by dust dispensers shaking the material in a small container through a sieve with 20 µm grid size [91]. In contrast, the nanoparticles are injected with a gas jet setup, see Refs. [92–94].

One major diagnostic in this thesis is the *Fourier Transform Infrared* (FTIR) spectrometry [95]. A Bruker Vertex 80v FTIR spectrometer is used for the measurement of the infrared absorption of SiO_2 (thesis article A1) and MF (thesis article A2) particles confined in the plasma by an external detector. In addition, the internal detector of

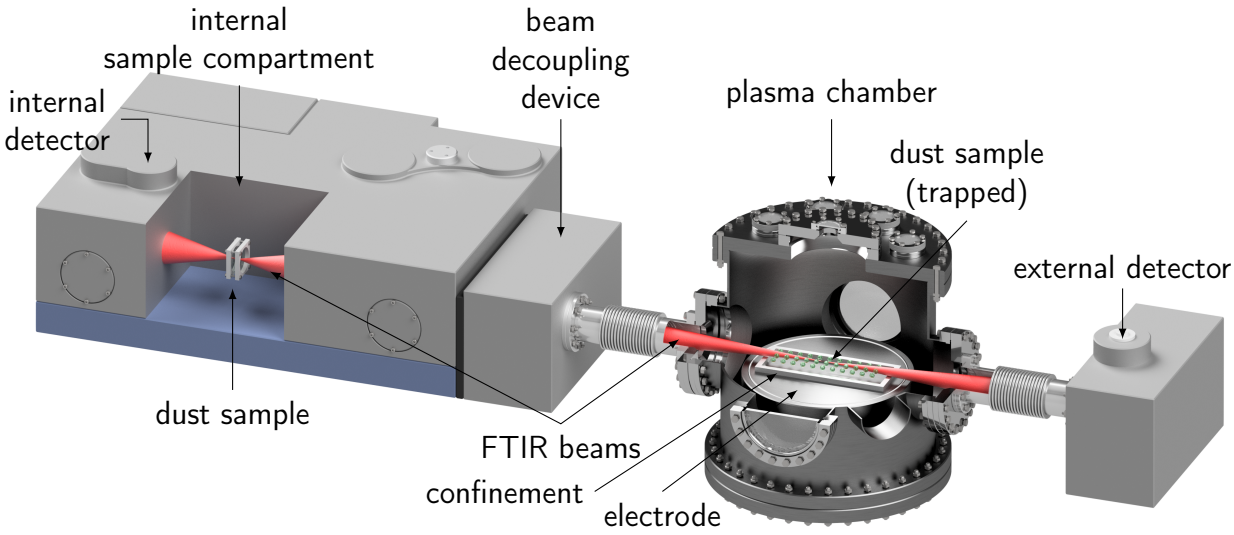

Figure 3.1: Scheme of the experimental setup with the Bruker Vertex 80v FTIR spectrometer. The FTIR spectrometer offers one internal detector for small samples and an external detector allowing the plasma chamber to be placed in the FTIR beam.

the spectrometer is used for reference samples without plasma exposure and heated dust samples, to investigate the influence of the particle temperature compared to the plasma impact on the IR absorption. For this purpose, a sample holder is equipped with two KBr glass plates. Between the glass plates a thin film of the dust is positioned. For heating purposes high power resistors are connected to the sample holder and PT-1000 temperature sensors are used to monitor the temperature. For details, see thesis article A2 (Sec. 6.3).

To determine the temperature of the particles confined inside the plasma, the fluorescence of Rhodamine-B doped MF particles is exploited [35, 96, 97]. The fluorescence is excited by a green laser at a wavelength of 532 nm. The fluorescent emission is located at around 590 nm and shows a temperature-dependent fluorescence signal. A VIS spectrometer (Ocean Optics USB 2000+) is used to determine the emission spectra of the fluorescent particles. Using a reference sample heated in the same sample holder mentioned in the previous section a temperature calibration can be done. Then, the measurement of the fluorescence emission signal can be correlated with the temperature of the particles in the plasma. For details, see thesis article A2 (Sec. 6.3).

3.2 Magnet Experiment

For the experiments with the superconducting magnet another geometry is needed. Due to the bore diameter in the center of the magnet of only 140 mm a very small chamber with an outer diameter of 120 mm has to be used, see Fig. 3.2a). An asymmetric rf discharge is ignited between the lower powered electrode of 80 mm diameter and the walls of the chamber. An illumination laser is guided through a port in the top of the chamber and redirected by a mirror mounted inside the chamber on one of the chamber walls. This illumination allows the observation of a horizontal plane of the particles confined in the plasma sheath by a camera through a window on the top, see Fig. 3.2b). The argon gas

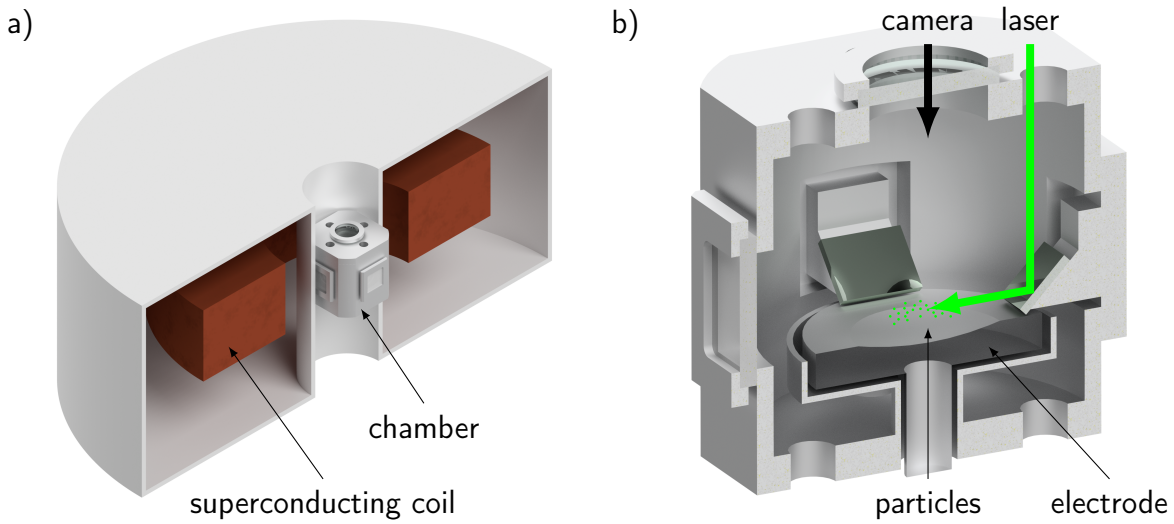

Figure 3.2: Sketch of the experimental setup of experiments with a superconducting magnet. a) Superconducting magnet and plasma chamber positioned inside the bore of the magnet. b) Plasma chamber with illuminated particles confined above the lower electrode. The camera is observing the particles through a window from the top.

pressure in operation is at 6 Pa and the applied plasma power 5 W. The superconducting magnet can be ramped up to a maximum axial magnetic field of 5.8 T.

The most common diagnostics in the field of dusty plasmas is video imaging. By illuminating the confined particles with a (widened) laser sheet, the light scattered by the particles is recorded. Then, the particle position $\vec{r}_i$ can be determined from the images using several approaches [98, 99]. Trajectories of the particles can then be reconstructed by linking the particle positions of successive frames resulting in a time series of $\vec{r}_i(t)$ for each particle. The particle velocity can be obtained from $\vec{v}_i(t) = \dot{\vec{r}}_i(t) = \Delta\vec{r}_i/\Delta t$, with the difference of two particle positions in two successive frames $\Delta\vec{r}_i$ and the inverse frame rate Δt. In this thesis this method is used to track a two-dimensional particle cluster. For details, see thesis article A3 (Sec. 6.4).

4 Results

FTIR spectroscopy is a novel approach to investigate dusty plasmas. For charge measurements, this diagnostics offers new possibilities to nanodusty plasmas where other charge diagnostics are not applicable. In this chapter, I will introduce this diagnostics as a method to determine particle charges in dusty plasmas with silica (SiO_2) nanoparticles, see Sec. 4.1.

Melamine-formaldehyde (MF) particles are widely used in laboratory dusty plasma experiments. FTIR spectroscopy will also be presented as a method to investigate the influence of the plasma exposition of MF particles on their chemical structure in Sec. 4.2.

The particle charge is not only of interest in nanodusty plasmas, but also in dusty plasmas under strong magnetic fields. The influence of strong magnetic fields on the charging of the particles will be discussed in Sec. 4.3.

4.1 Charge Measurement of SiO_2 Nanoparticles Using Infrared Absorption (A1)

The charge particles gain in a dusty plasma is of highest interest. The charge plays a decisive role in the confinement, the dynamics of the particles and the interaction between the particles. Hence, charge diagnostics are key diagnostics in dusty plasmas. For microparticles several methods have been developed and described. For single particles, the resonance method has been used [18–21]. There, an external periodic electric field superposes the field of the plasma discharge. Then, the resonant response of the particle to the electric field is exploited to derive the charge. For particles forming clusters [45, 100], the analysis of the normal modes leads to the particle charges [25, 101, 102]. In even larger systems containing hundreds or thousands of particles potentially forming waves can be exploited to find the particle charge [22–24, 29, 103]. This diagnostics is applicable to dusty plasmas with micron sized particles as well as nanometric dust. However, for systems with nanometric particles that do not support waves, there is no charge diagnostics, yet.

In thesis article A1 such a charge diagnostics for nanodusty plasmas is presented. We developed a method where the charge dependent IR absorption of the transverse optical phonon in the infrared wavelength range is used [104]. With silica nanoparticles of 40 nm radius, we found a suitable material for this investigation. SiO_2 exhibits a charge dependent optical phonon resonance as our calculations in Sec. 2.5 have shown.

The general setup of the experiment is described in Sec. 3.1. The particles are confined in between the lower powered and the upper grounded electrode. Using the FTIR spectrometer, the IR transmission of the dusty plasma is measured. As already shown in

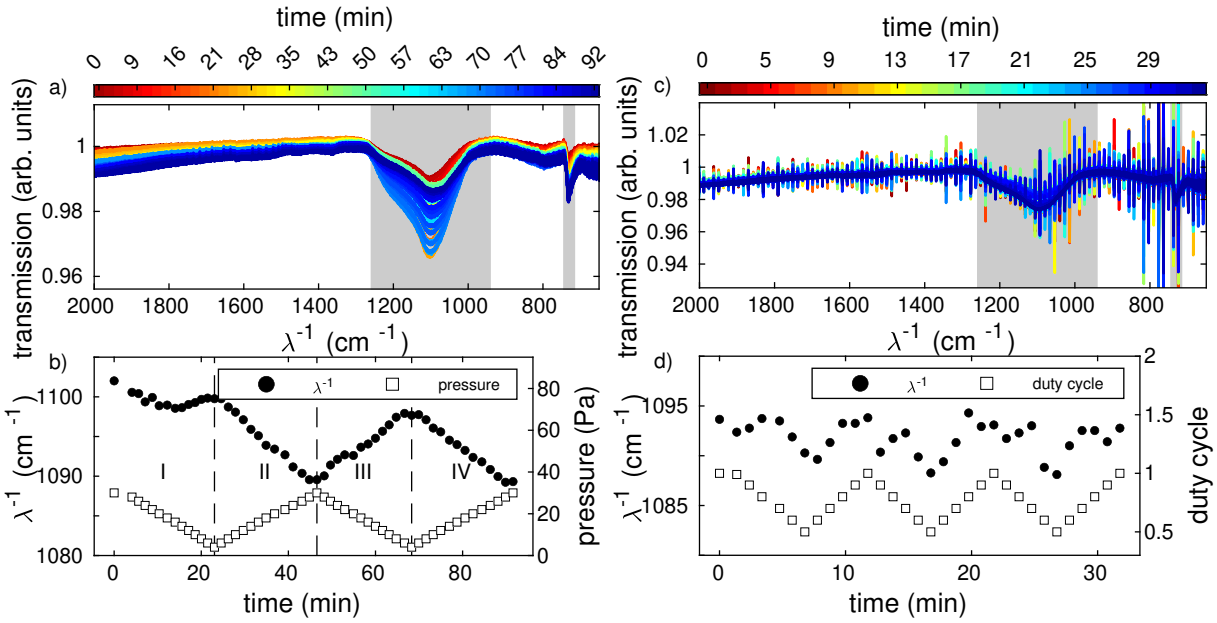

Figure 4.1: a) Transmission spectra of SiO_2 nanoparticles at different gas pressures. b) Shift of the absorption peak of the phonon resonance (circles, left axis) and argon gas pressure (squares, right axis) in dependence of the time. c) Transmission spectra of SiO_2 nanoparticles in a pulsed plasma at different duty cycles. d) Shift of the absorption peak of the phonon resonance (circles, left axis) and duty cycle (squares, right axis) in dependence of the time.

our calculations in Sec. 2.5 the relevant absorption peaks are expected to be located in the range $1000\,\mathrm{cm}^{-1} < \lambda^{-1} < 1200\,\mathrm{cm}^{-1}$.

Two approaches have been used to cause a change in the particle charge that should lead to shifts of the absorption features: by changing the argon gas pressure and by pulsing the plasma at 100 Hz at different duty cycles (for details see thesis article A1). The IR transmission spectra are shown in Fig. 4.1a) and c) for the pressure variation and the variation of the duty cycle, respectively. Two relevant absorptions can be detected in the FTIR spectra. One broad absorption peak between $1000\,\mathrm{cm}^{-1}$ and $1200\,\mathrm{cm}^{-1}$ and a second, smaller absorption peak at about $730\,\mathrm{cm}^{-1}$. The focus will now be laid on the broad absorption at $1100\,\mathrm{cm}^{-1}$. The position of minimum transmission is determined for every recorded spectrum.

The corresponding positions are displayed as circles in Fig. 4.1b) and d). The argon gas pressure in the first approach has been varied from 30 Pa to 4 Pa back and forth in four phases [I-IV], as indicated by the squares and the right axis. As can be seen, the position of minimum transmission first changes from above $1100\,\mathrm{cm}^{-1}$ at 30 Pa to slightly below $1100\,\mathrm{cm}^{-1}$ at 4 Pa in phase I. In phase two, the position shifts down to roughly $1090\,\mathrm{cm}^{-1}$ at 30 Pa. Phases III and IV nearly reproduce the same results as phase II. A clear correspondence between the change of the pressure and the shifting of the absorption position can be detected, here. However, the first phase does not really comply with that. In another measurement at constant pressure, the time evolution has been investigated. It has been found that the whole signal drifts with the time. This behavior is expected to be an artifact of the spectrometer. However, using this time drift as a calibration, the position of minimum transmission can be corrected.

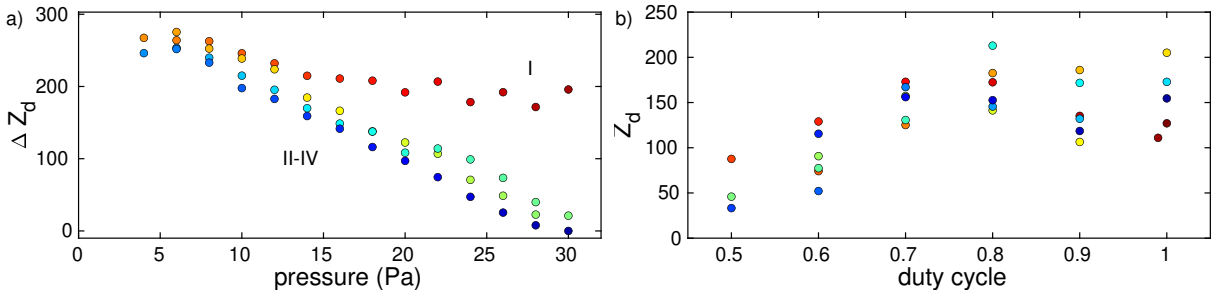

Figure 4.2: Derived a) relative charge in dependence of the argon gas pressure and b) absolute charge in dependence of the duty cycle.

For the second approach, the duty cycle has been varied between 1 and 0.5 several times. Again, the position of minimum transmission has been determined and is shown in Fig. 4.1d) (left axis) alongside the duty cycle (right axis). Although the positions scatter rather strongly compared to the pressure variation experiment, it can be seen that the signal follows the general trend of the duty cycle. While the position of minimum transmission is at about $1095\,\mathrm{cm}^{-1}$ for duty cycles close to 1, the position at minimum duty cycle of 0.5 is at about $1090\,\mathrm{cm}^{-1}$.

As a first result, a clear shift of the position of minimum transmission can be detected for both approaches. Now, to relate these changes in the position with a particle charge, the calculations from Sec. 2.5 are used.

Due to the time-drift correction of the shift, the absolute position of the signal is lost and only relative shifts with respect to one point of measurement can be considered. For the pressure variation measurements, the last measurement at 30 Pa has been used as a reference, here. Now, the calculated shifts can be used as a calibration to determine the particle charges relative to the charge at 30 Pa, see Fig. 4.2a). The relative charge difference has its maximum at minimum pressure with up to 300 elementary charges and decreases linearly towards the reference at 30 Pa. Only in ramping phase I this behavior is still not fitting as good as for the other three ramping phases, although the shifts have been corrected for the time drift.

For the pulsed experiments, the time drift has been subtracted accordingly. In contrast to the pressure variations, absolute approximations of the charge are possible, here, since by pulsing the plasma with different duty cycles a linear dependency of the charge on the duty cycle can be expected. The positions of the absorption minima (and hence, the corresponding dust charges) have been extrapolated from the measured duty-cycle range of $0.5 - 1$ to a duty-cycle of 0 corresponding to zero charge. The absolute charge in dependence of the duty cycle is shown in Fig. 4.2b). The maximum charge at a duty cycle of 1 is about 170 elementary charges, while the minimum charge at a duty cycle of 0.5 is about 70 elementary charges. The results scatter rather strong, but a general trend of the charge linearly depending on the duty cycle can be confirmed.

To put this into perspective, using OML theory [52] particles of 40 nm radius would gain about 170 elementary charges in an argon plasma with an electron temperature of $T_\mathrm{e} = 3\,\mathrm{eV}$ [105]. This suits rather fine for the highest duty-cycles, see Fig. 4.2b).

Taking ion-neutral collisions into account, the particle charge becomes dependent on the gas pressure [49, 53, 106], see Sec. 2.2. Within the gas pressure range between 4 Pa and 30 Pa a change in the charge of about 40 elementary charges would be expected, see Fig. 2.1. The determined charge difference from the pressure variation approach is about half a magnitude higher.

Comparing the results of both approaches and considering the rather large scatter of the results from the pulsing method, a very small absolute charge at 30 Pa can be extrapolated. In a rule of thumb assumption, $Z_{\mathrm{d}}(30\,Pa) \approx 50$ would fulfill the $Z \sim 1/p$ behavior sufficiently [49].

4.2 Infrared Absorption of MF Microparticles in a Dusty Plasma (A2)

Melamine-formaldehyde (MF) particles are a widely used species in dusty plasma experiments. Their benefits for these experiments are based on their spherical geometry and their availability in many different sizes with narrow size distributions in the micrometer range [107]. However, the plasma also impacts the particles. As reported in several works, the size of the particles can decrease during long plasma exposition due to outgassing and etching, see e.g. [35, 36]. Also, the roughening of the surface of particles in the plasma has been reported lately [108]. Hence, it is of big interest to further investigate the changes in the particles chemical structure induced by the plasma. When it comes to the chemical structure of these particles, FTIR spectroscopy is one approach to get a deeper insight.

In thesis article A2, an FTIR spectrometer has been used to study the chemical evolution of the particles [97]. Therefore, the IR absorption of the particles has been measured in-situ, as described in Sec. 3.1. The plasma has been ignited at an argon gas pressure of 3 Pa, and different plasma powers in the range between 3 W and 60 W have been applied. The measured IR absorption spectra for the different plasma powers are shown in Fig. 4.3a). The interesting spectral range of the IR spectra of MF is between 1800 cm^{-1} and 750 cm^{-1}. Here, several chemical specific absorption peaks can be found, as marked in Fig. 4.3a). At first glance, the major differences between the different applied plasma powers seem to be only changing absorption strengths. However, this is rather a result from the changing in the confinement position of the particles over this wide range of plasma power. But a deeper look reveals some interesting changes in the actual position of the absorption maxima, see Fig. 4.3b). For nearly all marked absorption regions (i)-(viii) a power dependent wavenumber shift can be seen in the range between 2 W and 60 W [peak (vi) will be discussed later]. The absorption peaks show a general trend of a shift towards smaller wavenumbers for powers up to 23 W and a reversed trend for higher powers returning almost to the starting position of minimum transmission at low powers. However, the strength of this shift differs a lot between the strongest shifts for peaks (iv) and (vii) of around 20 cm^{-1} and the smallest shifts for peak (viii) of only 1.5 cm^{-1}.

One approach to explain this shifting is based on the temperature dependence of the IR absorption of materials like MF. For other materials, like MgO, it has been found that the absorption peaks drift towards smaller wavenumbers with increasing temperature [37, 38, 109, 110]. Hence, we have performed FTIR measurements of our dust sample (without plasma) at different temperatures (see Sec. 3.1) to be able to compare the influence of the plasma to the influence of the temperature. For that purpose, the particles have been heated from room temperature up to 180°C and IR spectra have been taken during this heating process. Afterwards, the position of minimum transmission has been determined in analogy to the plasma-exposed sample. In Fig. 4.4 the shift in dependence of the temperature is shown for the previously mentioned peaks (i)-(viii). In this measurement, also peak (vi) was clearly identifiable and hence, is shown here as well. Peaks (ii)-(vi) all together show a shift towards smaller wavenumbers with increasing temperature. Similar

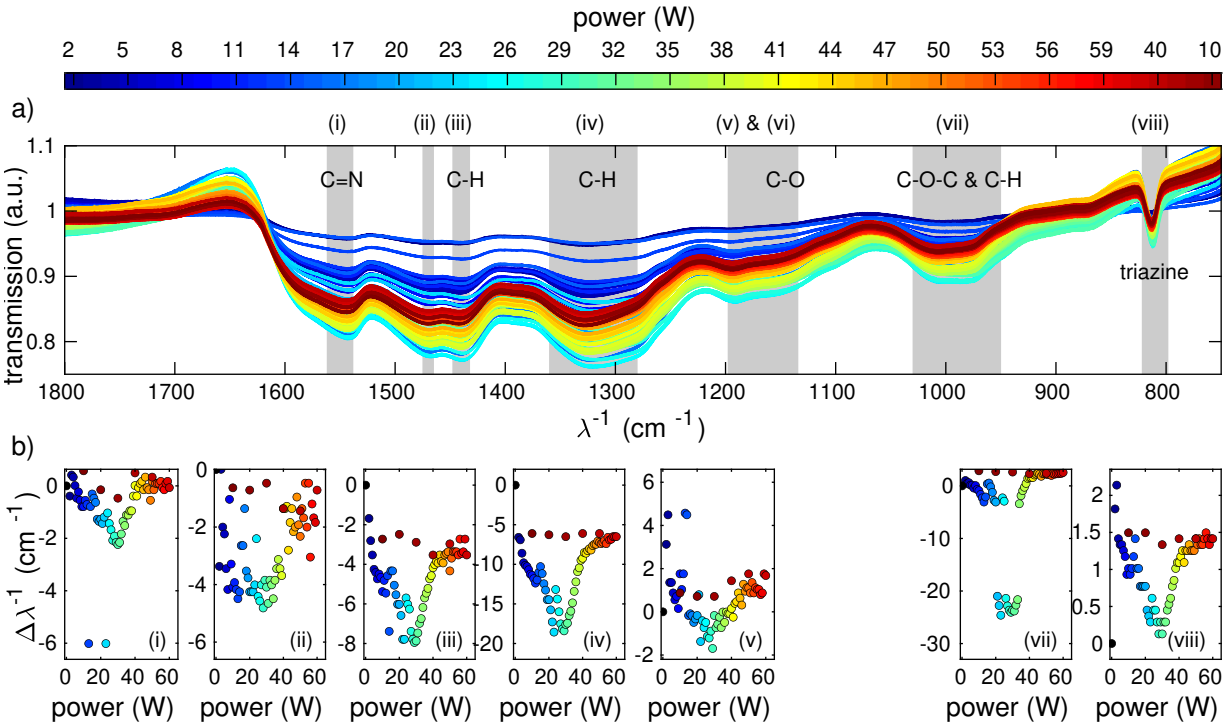

Figure 4.3: a) Infrared transmission spectra of MF microparticles in a plasma at different plasma powers. The identification of the molecular vibrations stems from [109]. b) Shift of the position of minimum transmission for the different absorption peaks in dependency of the plasma power.

as for the plasma-exposed sample (Fig. 4.3), different strengths of the shifts have been determined. Again, peak (v) shifts the strongest, while peak (iii) shifts the least. However, there are three peaks behaving differently: peaks (i) and (viii) shift only very little without a distinct direction of the shift and peak (vii) shifts towards higher wavenumbers, hence in the opposite direction compared to the other peaks.

To put both measurements, the one in the plasma environment and the one at different temperatures, into perspective, an additional measurement of the particles' temperature in the plasma seems reasonable. As indicated in Sec. 3.1, the fluorescence of Rhodamine-B doped MF particles has been used to determine the particle bulk temperature [35, 96, 97]. Over the power range from 5 W to 50 W the temperature of the particles in the plasma discharge rises from about 50°C at minimum power to more than 100°C.

Now, within this temperature range, the corresponding shifts of the IR absorption peaks in Fig. 4.4 are smaller than the shifts derived from the plasma-exposed particles in Fig. 4.3. In addition, a decrease of the temperature for powers above 23 W cannot be confirmed. Hence, the temperature alone cannot be the single reason of the shifting behavior of the plasma-exposed particles seen in Fig. 4.3.

However, a look into the (chemical) structure of the absorption peaks reveals further interesting details, see Fig. 4.5. The top row represents the temperature treated sample, while the two lower rows show the measurements of the plasma-exposed particles. The latter measurements have been separated into two rows (bottom row: $2\,\mathrm{W} < P < 23\,\mathrm{W}$, middle row: $24\,\mathrm{W} < P < 60\,\mathrm{W}$), for the sake of clarity. The peaks (i) emerging from the C=N bond, (iv) [C_{Ar}-N] and (viii) [triazine ring] [37] only show minor changes in both

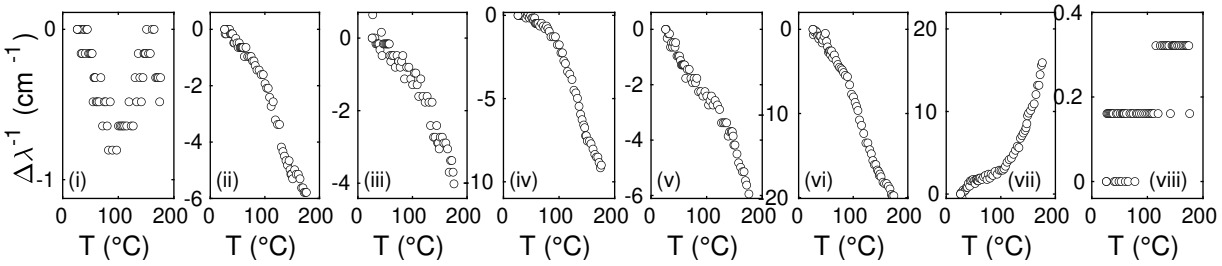

Figure 4.4: Shift of the position of minimum transmission of heated MF particles without plasma exposition in dependence of the applied heating temperature at the same peaks as in Fig. 4.3.

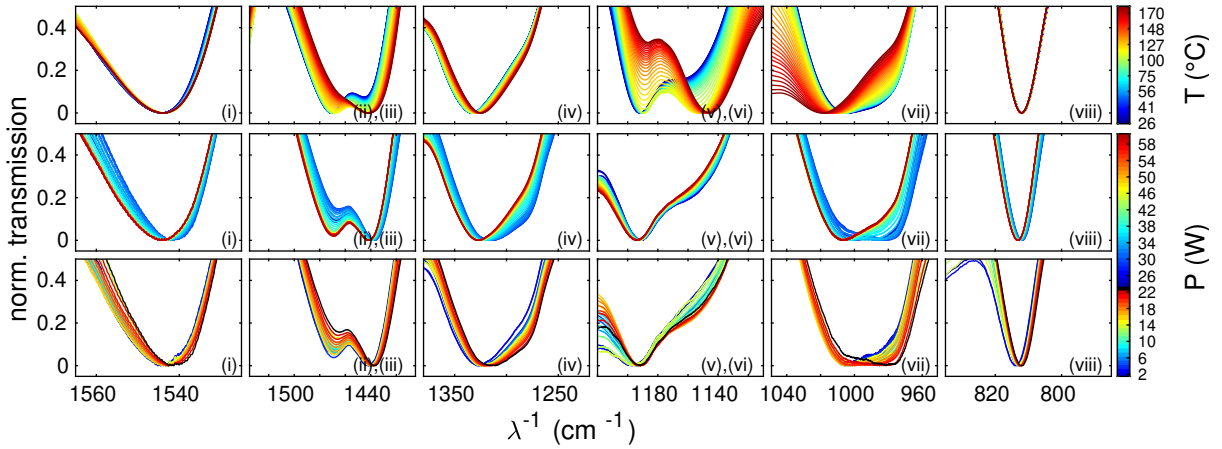

Figure 4.5: Structural analysis of the peaks marked in Fig. 4.3. The single peaks have been normalized to 1 at maximum and 0 at minimum transmission. Peaks (ii,iii) as well as peaks (v,vi) are handled together. First row represents the temperature dependent measurement, second and third row represent the power dependent measurements (2nd row: 24 W−60 W, 3rd row: 2 W−23 W).

samples. This can be attributed to the rather central position of these bonds in the MF resin. Only the knee at 1275 cm^{-1} of peak (iv) indicates chemical changes during plasma exposure, which cannot be seen in the heated sample.

Nevertheless, peaks (ii,iii,v-vii) behave quite differently. In the double peak structure (ii,iii) [CH_2, CH_3] the dominance of peak (ii) switches to peak (iii) with increasing temperature while peak (ii) nearly vanishes. In contrast, in the plasma environment peak (iii) is dominant all the time while peak (ii) becomes more dominant, but does not reach the absorption strength of peak (iii). The other double peak structure (v,vi) is based on a secondary amines C-N stretch (v), as well as C_R-N stretching and asymmetric C-O-C (vi) vibrations [111]. The peak (vi) occurs in the heated sample only at higher temperatures and seems to vanish immediately at plasma exposure. Peak (vii) has a rather broad minimum for low temperatures. With increasing temperatures the C-O stretching at 980 cm^{-1} gets less prominent and the whole peak moves towards higher wavenumbers in contrast to all other peaks. In the plasma environment, the C-O-C structure is getting more prominent with increasing power up to 23 W and decreases again afterwards.

In general, a trend of shifts towards lower wavenumber with increasing powers up to 23 W has been seen for all peaks in the plasma-exposed sample while for higher powers the shifts have been detected to reverse again.

The peak structures (ii,iii,v-vii) that exhibit major changes correspond to single C bond vibrations further at the edge of the MF resin, while the first mentioned rather stable peaks (i,iv,viii) correspond to central bonds.

In conclusion, the IR absorptions of MF particles inside a plasma and in a heated environment have been studied and compared. Taking into account a large number of absorption peaks in the fingerprint region of the spectrum, a general shift of the absorption peak positions towards lower wavenumbers with increasing temperature (without plasma) has been detected. Similar behavior has been seen for the particles confined in the plasma environment for powers of up to 23 W. For higher powers, a shift back towards positions corresponding to lower powers has been observed. A structural analysis of the peaks revealed the different influence of the chemical bonds associated with the peaks. More central bonds of the MF molecule like in the triazine ring were less influenced by the plasma and temperature exposition, while more peripheral vibrations have revealed changes in the chemical structure. These chemical changes occurred in different ways depending on the heated or the plasma-exposed sample. Therefore, a plasma chemical influence on the particles confined in the plasma is made accountable for the mentioned changes in the chemical structure of the MF particles. This is in good agreement with other works where the outgassing, etching, shrinking and roughening of the particles surface of MF and other plastic materials has been investigated [21, 33, 35, 36, 108].

4.3 Finite Dust Clusters Under Magnetic Fields (A3)

Under strong magnetic fields with fields between 5 and 10 T the electrons and ions are magnetized, while micron sized dust particles are not magnetized, as mentioned in Sec. 2.4. Due to the influence of the magnetic field on electrons and ions, the charging of dust particles under strong magnetic fields is interesting to investigate. Lately, superconducting magnets have become available and, hence, allow experiments at high field strengths. While some experiments on dust under magnetic fields have been performed previously [63, 65, 66, 112], now, in thesis article A3, the charge of dust particles has been measured over a wide range of magnetic fields.

In this article, a two dimensional dust cluster has been confined in a harmonic potential. The plasma chamber has been positioned into the bore of a superconducting magnet. The magnetic field has been ramped up from zero to 5.8 T. The cluster under investigation consisted of $N = 34$ particles. At a magnetic field of 170 mT one particle left the layer of the cluster and was aligned below one of the particles of the cluster. Due to the wakefield attraction the particle stayed there for the rest of the measurements [113, 114]. Hence, the particle size of the investigated cluster decreased down to $N = 33$.

The dynamics of these clusters can be described in terms of their normal modes. Starting with the total energy

$$E = \frac{1}{2} m\omega_0^2 \sum_{i=1}^{N} r_i^2 + \frac{Q^2}{4\pi\varepsilon_0} \sum_{i>j} \exp(-r_{ij}/\lambda_\mathrm{D}) \tag{4.1}$$

where r_i is the distance of particle i to the center of mass of the cluster, $r_{ij} = |\vec{r}_i - \vec{r}_j|$ is the interparticle distance and ω_0 is the confinement frequency of the two dimensional

harmonic confinement. Then, the energy can be written as

$$\hat{E} = \sum_{i=1}^{N} \hat{r}_i^2 + \sum_{i>j} \frac{1}{\hat{r}_{ij}} \exp(-\hat{r}_{ij}\kappa) \tag{4.2}$$

in units of the normalized radius

$$r_0 = \sqrt[3]{\frac{Q^2}{4\pi\varepsilon_0} \frac{2}{m\omega_0^2}} \tag{4.3}$$

and energy

$$E_0 = \frac{1}{2} m\omega_0^2 r_0^2 \tag{4.4}$$

with $\kappa = r_0/\lambda_\mathrm{D}$, $\hat{E} = E/E_0$ and $\hat{r} = r/r_0$ [101, 102]. Hence, the cluster behavior only depends on the screening strength κ and N. From the absolute values of r_0 and ω_0, the screening length and the particle charge can be derived. The modes ℓ are determined by the dynamical matrix containing the second derivative of the total energy with respect to all particles and coordinates and its eigenvector $\vec{e}_\ell$ characterizing the oscillation pattern and the eigenvalue λ_ℓ characterizing the mode frequency $\omega_\ell^2 = \lambda_\ell \omega_0^2/2$ [50, 115].

The camera recorded the positions of the laser illuminated particles for 5 s for each magnetic field setting. The resulting trajectories of the particles are shown in Fig. 4.6 for five different field strengths. At magnetic fields of $B = 0\,\mathrm{T}$ and $B = 10\,\mathrm{mT}$, the position of the particles in the cluster changes only slightly. Starting at $B = 100\,\mathrm{mT}$, the particles start moving stronger while still being bound to their original equilibrium position within the cluster. At even higher fields, the cluster starts rotating. During the rotation only a few particles switch positions within the cluster. From the obtained trajectories the particle velocities are determined. Then, a normal mode analysis is performed [43, 44, 101, 102] by decomposing the velocities $\vec{v}_i(t)$ into their contribution to each eigenmode

$$v_\ell(t) = \sum_{i=1}^{N} \vec{v}_i(t) \cdot \vec{e}_{\ell,i} \ . \tag{4.5}$$

The spectrum can then be derived from the spectral power density

$$S_\ell(\omega) = \frac{2}{T} \left| \int_{-T/2}^{T/2} v_\ell(t) \exp(\mathrm{i}\omega t)\, \mathrm{d}t \right|^2 \ . \tag{4.6}$$

The normal mode analysis results in a spectral power density $S_\ell(\omega)$ for each of the $2N$ modes ℓ. This spectral power density is shown in Fig. 4.7 for four different magnetic field strengths. In general, the frequency of the highest power density increases from 0 at the first mode to about 8 Hz at the highest mode numbers. In the presence of a magnetic field additional features occur. At mode number 20 the breathing mode is excited for magnetic fields of $B = 130\,\mathrm{mT}$ and $B = 510\,\mathrm{mT}$, as well as a vortex-antivortex mode at mode number 35. For higher magnetic fields this mode is getting less dominant, again. At mode number 40 a wakefield mode can be identified for fields above 170 mT, due to the structural change and the particle confined below the cluster-layer. In addition, the sloshing modes (last two modes in Fig. 4.7) naturally are present at all magnetic fields.

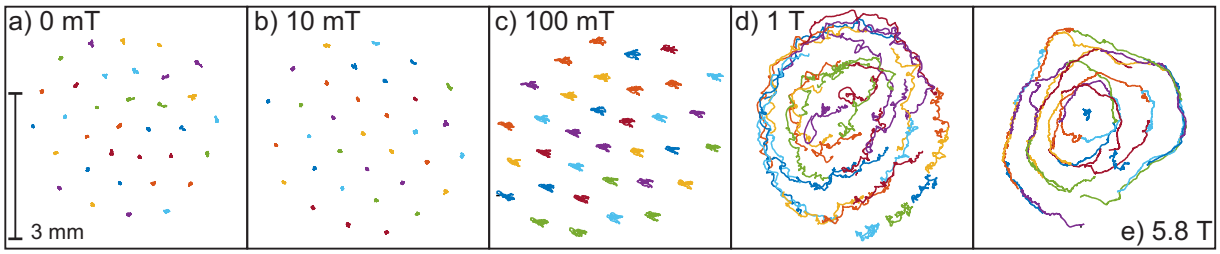

Figure 4.6: Particle trajectories of a cluster with $N = 34$ confined particles at different magnetic field strengths.

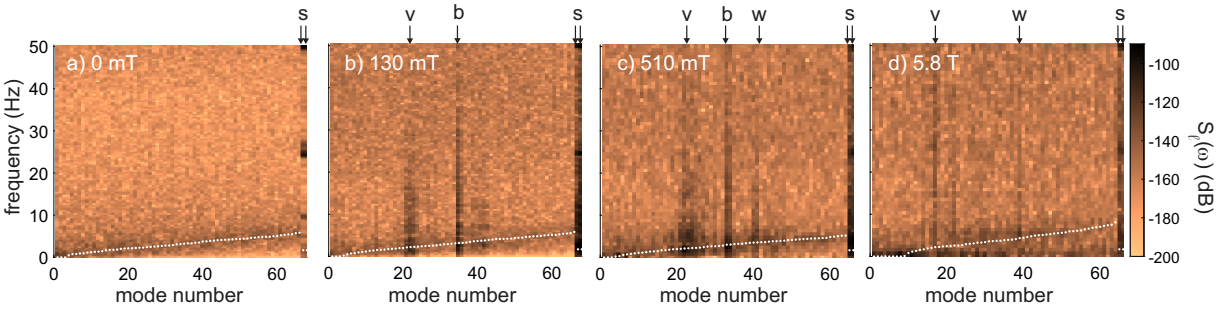

Figure 4.7: Spectral power density for the $2N$ modes in dependence of the frequency. The white dots indicate the fit of the theoretical mode spectrum. s: sloshing mode, v: vortex-antivortex mode, b: breathing mode, w: wakefield mode.

Now, two approaches are used to determine the particle charges and the screening length. The dynamics of all $2N$ modes only depend on the charge $Q_\mathrm{d} = Z_\mathrm{d} e$, the screening length λ_D and the confinement frequency ω_0. In the first approach, the confinement frequency ω_0 is obtained from the sloshing mode. Then, the particle charge Q_d and the screening length are used as fit parameters to fit the theoretical mode spectrum to the measured spectral power density. The corresponding fits are shown in Fig. 4.7 as white dots. As can be seen, the fitted theoretical spectra closely follow the measured data. Hence, the resulting fit parameters Q_d and λ_D are expected to be well determined.

The second approach takes into account that the sloshing mode cannot be easily detected for all field strengths. Here, a value for the screening strength $\kappa = r_0/\lambda_\mathrm{D}$ is prescribed. Then, Q_d and ω_0 are determined from the fit. In this case, $\kappa = 1$ is chosen.

The results for both methods are shown in Fig. 4.8 for the charge number. It can be seen that both methods show a particle charge in the range from 9000 to 12000 elementary charges with only small fluctuations, which is a reasonable particle charge for this particle size of 9.55 µm [23, 102, 116]. The only major difference between both methods is the decreased charge around 0.1 T from the method with ω_0 from the sloshing modes. Using different values for κ only slightly changes the results. The determined rather constant particle charges are in good agreement with experiments from Carstensen et al. [64]. However, simulations show a slight decrease of the particle charge towards higher fields [117–119]. Nevertheless, the experiments are still in good agreement with these simulations since the charges change only little with the variation of the magnetic field.

Considering the magnetic fields where magnetization M_k and Hall parameter h_k for electrons and ions reach unity, one finds interesting coincidences. The positions are marked in Fig. 4.8. A slight decrease of the particle charge is seen until $M_\mathrm{e} = 1$. Between $M_\mathrm{e} = 1$ and $h_\mathrm{i} = 1$ the particle charge increases again. From the method where the sloshing

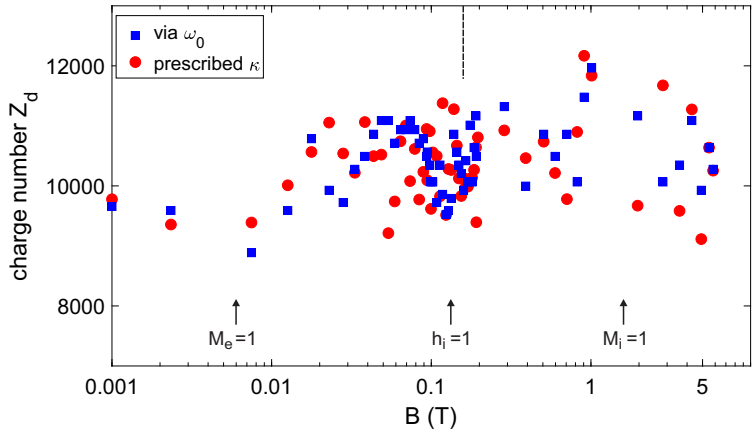

Figure 4.8: Charge number Z_d retrieved from one method where the confinement frequency ω_0 is extracted from the sloshing modes (blue squares) and one where a prescribed κ is used (red circles).

modes are used to determine ω_0, a dip in the charge at $h_\mathrm{i} = 1$ is derived. Although these features coincide, it is difficult to explain the physical process. This is due to many factors contributing in diverse ways. The particles are trapped in the plasma sheath where strong electric fields occur and a directed supersonic ion flow dominates in addition to the complexity of the magnetic field itself.

5 Summary

Charge measurements in different situations in dusty plasmas have been explored. In the first part of this thesis, a novel approach for charge measurements in nanodusty plasmas has been presented. In this approach, the charge-dependent phonon resonance of the particles was used to determine the particle charge. In calculations based on the work of Heinisch et al. [30], I have shown that silica nanoparticles are suitable for an experimental investigation of the phonon resonance, since the particles exhibit the relevant charge-dependent shift of the resonance. The resonance is located in a handy wavenumber range where FTIR spectrometers can measure the absorption sufficiently. In addition, silica is commercially available in form of nanoparticles with 40 nm radius.

For the experiments, a large plasma chamber has been integrated into the beam path of an FTIR spectrometer. I have shown that the absorption of the nanoparticles in the IR wavelength range can be detected and the absorption of the phonon resonance can be identified. I was able to induce a change in the particle charge by changing the background gas pressure and by modifying the duty-cycle.

By changing these parameters, a clear dependence of the absorption peak position on the charge was found. By combining both the calculations of the shift with the particle charge and the measured shifts, I was able to deduce particle charges for both approaches. The determined particle charges can be classified to lie in a reasonable range for particles with a size of 40 nm.

In the second part, the influence of plasma exposure on the chemical structure of melamine-formaldehyde particles has been investigated. An FTIR spectrometer has been used to identify several absorption peaks in the fingerprint region. By varying the plasma power, a shift of some of the absorption peaks was found. In general, a shift towards lower wavenumbers with increasing plasma power of up to 23 W was detected. For higher powers, this shift reversed close to the starting positions. The particle temperature can cause some of the behavior seen in the plasma exposed sample, but especially not the reversed shifts for higher powers. A further structural analysis then showed that central bonds of the MF resin only changed little, while the more peripheral bonds changed significantly, which was attributed to processes like plasma etching.

The focus of the third part of this thesis was on dusty plasmas under strong magnetic fields. Therefore, a finite-dust cluster was confined in an harmonic potential and the whole discharge was placed in the center of a superconducting magnet. By analyzing the normal modes of the two-dimensional cluster, we were able to deduce particle charges. The variation of the magnetic field over a wide range of field strengths from 0 to 5.8 T showed that the particle charge was rather constant for all fields, which is in good agreement with other works. However, small changes occurred at field strengths where different stages of magnetization of electrons and ions are expected.

In this thesis, I have shown the advantages and suitability of FTIR methods for the investigation of the particle charge in nanodusty plasmas and for the analysis of the

chemical structure of dust particles in the plasma environment. The non-invasivity of this novel method in dusty plasmas may not only be applicable to scientific laboratory plasmas, but also to the industry for monitoring purposes, as well as for the investigation of astrophysical dusty plasmas.

The investigation of dusty plasmas under strong magnetic fields shows relevance towards fusion plasmas. Dust particles enter the plasma in fusion devices as a result of the interaction of the plasma with surfaces of the walls and other components. Hence, the investigation of the influence of these particles with the strong magnetic confinement fields is also of high interest.

6 Thesis Articles

6.1 Author Contributions

A1 H. Krüger, E. Thiessen, F. X. Bronold, H. Fehske, and A. Melzer, Charge measurement of SiO_2 nanoparticles in an RF-plasma by IR absorption, *Phys. Rev. E*, submitted (2021).

H. Krüger prepared and conducted the experiments. H. Krüger and E. Thiessen performed the calculations of the extinction. H. Krüger analyzed the data and wrote the manuscript. All authors contributed to the data interpretation and co-edited the manuscript.

A2 H. Krüger, E. Sündermann, and A. Melzer, Investigation of the IR absorption of trapped MF particles in a dusty plasma, *Plasma Sources Sci. Technol.* in press (2021).

H. Krüger prepared the experiments. H. Krüger conducted the experiments supported by E. Sündermann. H. Krüger analyzed the data and wrote the manuscript. All authors contributed to the data interpretation and co-edited the manuscript.

A3 A. Melzer, H. Krüger, S. Schütt, and M. Mulsow, Finite dust clusters under strong magnetic fields, *Phys. Plasmas* **26**, 9 (2019).

All authors jointly installed the magnet. S. Schütt and H. Krüger prepared the dusty plasma experiment. A. Melzer, H. Krüger and S. Schütt jointly performed the experiments. A. Melzer analyzed the data and wrote the manuscript. All authors contributed to the data interpretation and co-edited the manuscript.

6.2 A1 - Charge measurement of SiO_2 nanoparticles in an RF-plasma by IR absorption

Harald Krüger, Elena Thiessen, Franz Xaver Bronold, Holger Fehske, and André Melzer

Physical Review E, submitted (2021)

Charge measurement of SiO_2 nanoparticles in an RF-plasma by IR absorption

Harald Krüger, Elena Thiessen, Franz Xaver Bronold, Holger Fehske, and André Melzer
*University of Greifswald, Institute of Physics, Felix-Hausdorff-Str. 6, 17489 Greifswald, Germany**
(Dated: June 30, 2021)

We have performed measurements of the IR absorption of SiO_2 nanoparticles confined in an argon radio-frequency plasma discharge using an FTIR spectrometer. By varying the gas pressure of the discharge and duty cycle of the applied radio-frequency voltage we observed a shift of the absorption peak of SiO_2. We attributed this shift to charge-dependent absorption features of SiO_2. The charge-dependent shift has been calculated for SiO_2 particles and from comparisons with the experiment the particle charge has been retrieved. With the two different approaches of changing the gas pressure and altering the duty cycle we are able to deduce a relative change of the particle charge with pressure variations and an absolute estimate of the charge with the duty cycle.

I. INTRODUCTION

Complex plasmas consist of electrons, ions, neutral gas atoms and additional massive particles. The size of these particles usually ranges between nanometers and 10 µm in radius. Due to the flux of electrons and ions from the plasma onto the particles, the particles gain a charge. Since the electrons are more mobile, this charge is usually negative. The fact that these particles constitute further, observable plasma species has led to the rapid development of the field of complex plasmas in the last three decades [1–5]. For a long time, the focus of research in this topic has been put on microparticles with the complex plasma as a model system for atomic or molecular systems due to the rather simple access to properties like the position and velocity of the particles [6–12]. However, the investigation of nanometric particles in a plasma discharge has become more important recently. For example, particle growing mechanisms, electron depletion effects and dust clouds in strong magnetic fields have been investigated [13–19].

Since the particle charge is of fundamental interest for basically every process in dusty plasmas, several approaches have been made to measure it. One example is the resonance method for single particles [20–23]. Here, the electric field in the plasma is superposed by an external periodic electric field. From the resonant response of the particles to the changing electric field, the charge can be derived. In another approach thermally excited normal modes are measured in a cluster with a few particles. Comparing the frequency relations of different modes from experiment and theory allows to access the particle charge [24–26]. For many-particle systems that support waves the charge can be derived from the analysis of the wave dispersion [27–30]. Nevertheless, all these methods are usually only applicable for dust systems with micron sized particles where single particle trajectories can be followed by video diagnostics.

Hence, there is a need for a charge diagnostic for (three-dimensional) dust systems with nanoscaled particles. In their approach, Tadsen *et al.* exploited dust-acoustic waves in nanodusty plasmas to gain information on the particle charge [31]. However, the presence of waves is not always assured.

Therefore, Heinisch *et al.* have suggested a drastically different approach, where the charge-dependent absorption of infrared light by nanoscaled particles is exploited [32, 33]. They have shown analytically, that the electrons residing as charges on the particles cause a change in the effective refractive index of the particles. With this change in the refractive index, the light scattering behavior, especially in the infrared wavelength regime of the particles, is shifted and hence, can be used to determine the charge of the particles. Heinisch *et al.* have performed calculations for a variety of materials ($Al_2O_3, Cu_2O, LiF, MgO, PbS$). For these materials it is found that the absorption line of the transverse optical phonon in the infrared spectral range shifts towards higher wavenumbers with increasing particle charge. As a rule, the shift is of the order of $10\,cm^{-1}$ for a particle of 50 nm radius. However, most of the relevant lines for these materials are at wavenumbers far below $1000\,cm^{-1}$. In principle, the shift should be observable using Fourier transform infrared (FTIR) absorption, but this is a difficult region for FTIR spectrometers. Only aluminum oxide seems to have an absorption in a suitable wavenumber range, however, the required α-Al_2O_3 nanoparticles are difficult to obtain due to technical difficulties in manufacturing processes [34]. Another material that is available and has an absorption in a suitable wavenumber range is silicon dioxide (SiO_2). In this work, we demonstrate a charge diagnostic exploiting the charge-dependent shift of the phonon absorption in experiments and calculations using SiO_2 as a well suited material.

The paper is structured as follows. In the next section we give an overview of the experimental setup. In Sec. III we study the absorption of the nanometric SiO_2 dust in the plasma by FTIR spectroscopy. There, we observe and measure the shift of the phonon absorption with changing plasma conditions. In addition, we perform corresponding calculations of the charge-dependent shift for SiO_2 in Sec. IV. Afterwards, we combine the measurements and calculations to deduce dust charges for the SiO_2 particles. Finally, Sec. VI summarizes our

* harald.krueger@physik.uni-greifswald.de

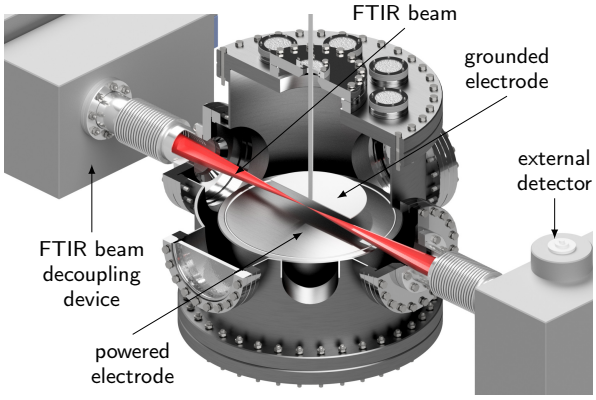

FIG. 1. Scheme of the experimental setup with the Bruker Vertex 80v FTIR spectrometer, the FTIR decoupling device, the plasma chamber with one large powered electrode and the FTIR detector.

results.

II. EXPERIMENTAL SETUP

For our experiments, we use a low-temperature radio-frequency plasma discharge ignited in a vacuum chamber with an inner diameter of 40 cm. A lower, powered electrode with a diameter of 30 cm is separated from the upper, grounded electrode with a diameter of 20 cm by a distance of 3.5 cm. Argon is used as a background gas at operating pressures between 4 Pa and 30 Pa. The rf generator supplies discharge powers of up to 50 W. To measure the charge-dependent shift in the infrared a Bruker Vertex 80v FTIR spectrometer is connected to the discharge chamber via two ports, to guide the FTIR beam through the plasma. In addition to the FTIR measurements inside the plasma chamber, the FTIR is equipped with another, internal compartment that is used for measurements of samples that are not being exposed to the plasma environment. The entire FTIR beam paths are under vacuum. A scheme of the experimental setup can be seen in Fig. 1. For additional information, see [35].

We run the FTIR spectra at a spectral resolution of $0.08\,\mathrm{cm}^{-1}$. Each FTIR spectrum is averaged over 100 single scans. The measurement time for a spectrum is about 60 seconds.

We use commercially available silica (SiO_2) nanoparticles of around 40 nm radius [36]. The particles are inserted into the plasma via gas jet injection [37–39]. The nanoparticles then form a three dimensional, extended dust cloud where individual particles can no longer be distinguished. The light scattered by the cloud from a sheet of laser light is used to monitor the evolution of the dust cloud.

While other dust materials like PMMA or MF show a significant outgasing and shrinking during long term plasma exposition, SiO_2 particles are stable in the plasma environment and the plasma does not cause a reduction of particle size [40].

To reduce the influence of external parameters (optical constants, different response of the internal and external FTIR detectors etc.) we seek for experiments where the charge of the particles is changed using one and the same dust cloud.

As shown by Ratynskaia *et al.* [41] and Khrapak *et al.* [42], the (absolute value of the) particle charge is seen to be reduced with increasing gas pressure due to stronger ion-neutral collisions that increase the ion flux to the particle. Hence, in our experiments, we have varied the neutral gas pressure of the plasma. With this, we expect the particle charge to change and to be able to see a change in the IR absorption of the material in the discharge. The IR spectra are measured for neutral gas pressures in the range from 4 Pa to 30 Pa.

A second approach is to induce a change in the charge by pulsing the plasma. Thereby, we switch "on" and "off" the plasma at a frequency of 100 Hz and the particles gain and loose their charge periodically. The frequency of 100 Hz is low enough to charge and uncharge the particles nearly completely. We have verified using OML (orbital motion limit) model charging current calculations [43, 44] that charging and decharging processes are so fast compared to the pulsing frequency that they do not play a role, here. Now, changing the duty cycle of the plasma offers the opportunity to vary the charge. Hence, the temporally averaged charge is nearly proportional to the relative "on"-time-fraction of the plasma. Therefore we can generate a series of different charge numbers for the particles in the plasma and compare the IR spectra with those of the continuously driven plasma. As expected [21], we find only a very minor influence of the plasma power on the absorption.

III. FTIR MEASUREMENTS

A. Pressure variations

We now present the measurements of the FTIR spectra of the confined dust in the plasma environment. In our experimental approach, we sweep the argon gas pressure from 30 Pa to 4 Pa back and forth several times. The measured FTIR absorption spectra are shown in Fig. 2a. The spectra are displayed in the range from $2000\,\mathrm{cm}^{-1}$ to $600\,\mathrm{cm}^{-1}$. A total of 53 measurements on the same cloud have been done. The absorption amplitude is of the order of a few percent. The interesting absorption structure is located at around $1100\,\mathrm{cm}^{-1}$, where the transmission shows a rather broad local minimum. In what follows, we focus on this structure (marked by the gray background).

On the one hand, the absolute absorption reduces with increasing measurement time. This can mainly be accounted for as a feature from the FTIR spectrometer and the number of particles in the line of sight of the FTIR

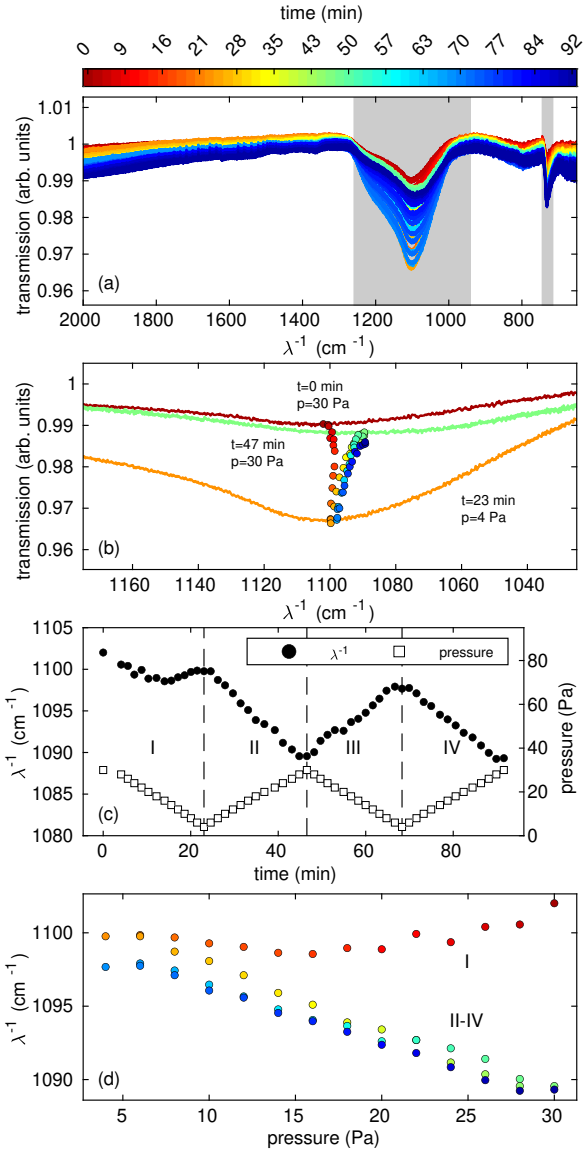

FIG. 2. (a) Transmission spectra of SiO_2 nanoparticles confined in an argon rf-discharge at a plasma power of 15 W at different argon gas pressures in the range from 4 to 30 Pa. (b) Transmission minima of the absorption peaks at around 1100 cm^{-1} with three spectra at $t = 0, 23, 47$ min. (c) Position of minimal transmission (circles, left axis) and argon gas pressure (squares, right axis) in dependency of the time of the measurement. (d) Position of minimal transmission in dependency of the argon gas pressure.

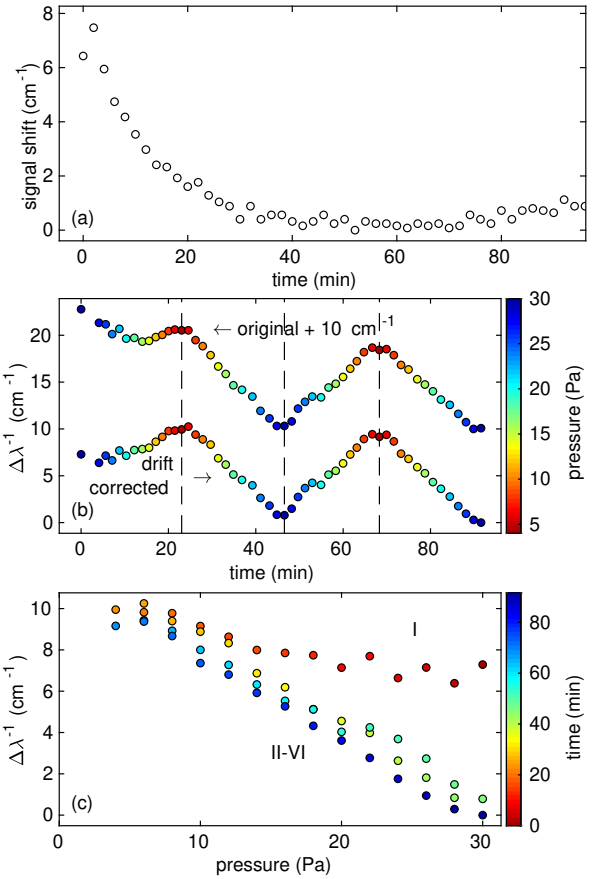

FIG. 3. (a) Time resolved shift of the absorption peak position at a constant pressure of 30 Pa after particle injection. (b) Time resolved change of the particle absorption peak at different pressures (color coded) in original and drift-corrected version. The original time series has been offset by $\Delta\lambda^{-1} = +10\,cm^{-1}$ for clarity. (c) Corrected shift of the absorption peak position in dependence of the gas pressure.

beam. On the other hand, we are primarily interested in the wavenumber position of the absorption structure. Therefore, a more detailed view is given in Fig. 2b.

Here, the position of minimal transmission is shown for every measurement. To more accurately determine the minimum position of the absorption, the minimum has been determined after fitting a polynomial to the absorption signal in the selected spectral range and then using the minimum of the fit. In addition, three spectra at different times ($t = 0, 23, 47$ min) are shown as a reference.

The position of maximum absorption of the charged dust in the plasma depending on the measurement time is displayed in Fig. 2c together with the corresponding pressure values. In the first pressure scan I (30 Pa down to 4 Pa) the absorption minimum shifts from 1103 cm^{-1} to 1100 cm^{-1}, the second scan II (on the same cloud) from 4 Pa to 30 Pa shows a stronger variation of λ^{-1}, where the absorption feature moves from 1100 cm^{-1} to 1090 cm^{-1}. The subsequent scans III (30 Pa down to 4 Pa) and IV (4 Pa to 30 Pa) follow scan II very closely. Obviously, a time-dependent drift of the FTIR signal overlays the

measurement spectrum. Nevertheless, it can easily be seen, that the position of maximum absorption decreases in phases of increasing gas pressure and vice versa, especially for scans II to IV. Fig. 2d shows the dependency of the absorption minimum on the argon gas pressure. Apart from the first pressure ramp, the other pressure ramps clearly indicate an increasing wavenumber of the absorption peak with decreasing pressure.

To evaluate the time-dependent drift of the FTIR signal, we perform additional measurements of this process at constant pressure. The IR absorption is measured at a constant argon gas pressure of 30 Pa every 120 s for over 90 minutes. The position of the absorption peak is determined in analogy to the previous measurement. In Fig. 3a, the absorption minimum is shown. As can be seen, the signal position changes strongly in the first few minutes and decreases from about 8 cm^{-1} at the beginning to roughly zero within 30 min. (The temporal shift with respect to the minimum value at $t = 50$ min is given.) Afterwards, the position of the signal is only weakly shifted.

Now, the original pressure-dependent shift of Fig. 2c is corrected for the temporal drift (Fig. 3a). In Fig. 3b the original shift at varying pressure and the drift-corrected shift are presented. As can clearly be seen, the characteristic ramping structure with increasing and decreasing pressure can be seen in both the original and the drift-corrected version. Now, the drift-corrected version exhibits increasing shifts $\Delta\lambda^{-1}$ with decreasing pressure also for the first pressure ramp. Nevertheless, the values in the first 20 min still do not match the values of the next ramping period as nicely as for the following ramping sections. In addition, we have to mention, that due to the drift-correction, we have lost information about the absolute shift and therefore, can only discuss relative changes in the particles IR absorption. The uncharged dust sample measured in the internal sample chamber of the FTIR as mentioned in Sec. II shows a stable absorption position at $\lambda_0^{-1} = 1092.8\,\mathrm{cm}^{-1}$. Nevertheless, due to the drift of the external detectors' signal we cannot uniquely put both measurements in relation to each other. Hence, we decided to show the shift $\Delta\lambda^{-1}$ with respect to the minimum value at 30 Pa. In Fig. 3c, the drift-corrected shift is shown again in dependency of the applied argon gas pressure. In comparison to Fig. 2c, also the first 13 measurements in the first ramping section (30 Pa to 4 Pa) join in the general trend of an increasing shift with decreasing argon gas pressure.

Before putting this shift of the absorption into relation with a possible change in the charge, we first present another method of changing the particle charge in the plasma.

B. Pulsing

In this experiment, we sweep the duty cycle between 50% and 100% back and forth. Similar to the pressure

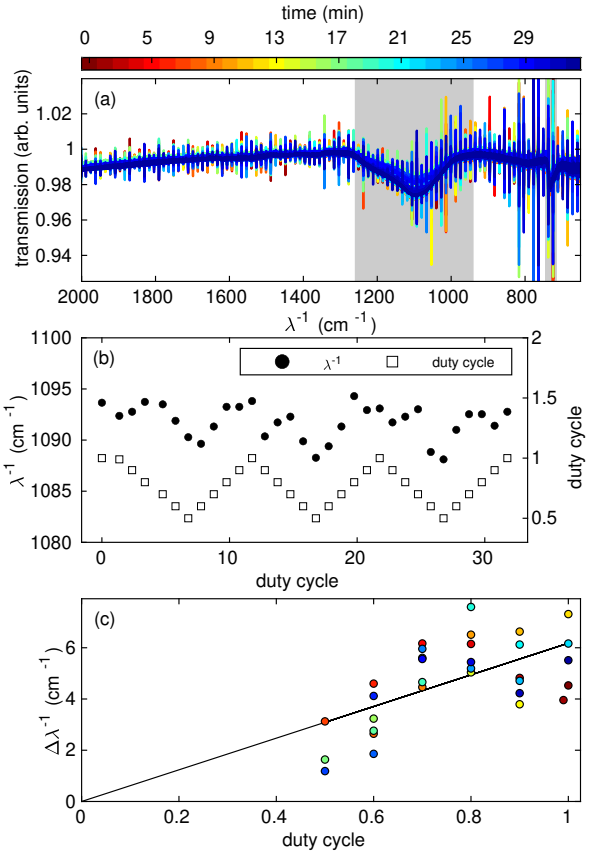

FIG. 4. (a) Transmission spectra of SiO_2 nanoparticles confined in an argon rf-discharge at a plasma power of 50 W at an argon gas pressure of 10 Pa at different pulsing duty cycles with a frequency of 100 Hz. (b) Position of minimal transmission (circles, left axis) and duty cycle (squares, right axis) in dependency of the time of measurement. (c) Shift of the position of minimal transmission in dependence of the duty cycle with linear fit.

variations in Sec. III A, we first show the general spectral overview in Fig. 4a. The spectrum for an applied plasma power of 50 W at an argon gas pressure of 10 Pa and duty cycles between 0.5 and 1 looks very similar to the spectrum from the pressure variation. However, in the detail we do find differences: The absolute absorption is a little weaker and the entire spectrum is overlaid with equidistant spikes. Moreover, the spikes depend on the pulsing frequency, i.e., they are an artifact of the FTIR signal. Nevertheless, since the spikes have a rather small width, they are clearly separated in the main signal and the absorption minimum is still easily and reliably measurable.

In analogy to the pressure variations, we determine the position of minimal transmission and plot them against the time of the measurement together with the applied duty cycle, see Fig. 4b. The position of minimal trans-

mission ranges between 1095 cm^{-1} at higher duty cycles and 1090 cm^{-1} at lower duty cycles and hence, generally follows the ramping of the duty cycle. Although the shift $\Delta\lambda^{-1}$ does not follow exactly the duty cycle, a general trend of decreasing shift with decreasing duty cycle can be determined. Again, we have subtracted the FTIR's time dependent drift of the signal in analogy to Sec. III A.

Basic simulations of the charging and decharging time scales [43, 44] show, that the time averaged charge is close to linearly depending on the duty cycle for a frequency of 100 Hz. We use this expected linear dependence of particle charge with duty cycle to determine an absolute shift $\Delta\lambda^{-1}$ for the data. Therefore, we perform a linear fit to the data and use the extrapolation to duty cycle 0 % as the zero point of the shift $\Delta\lambda^{-1}$. From that we get an overall shift of $\Delta\lambda^{-1} = 6\,\mathrm{cm}^{-1}$ for a duty cycle of 100 %.

As a result, we now have two ways to determine a characteristic shift of the signal, one relative shift with the pressure, and one absolute shift with the duty cycle. Now, to put the shift of the absorption into perspective with the charge, calculations of the resonance shift are presented in the next section.

IV. THEORETICAL ANALYSIS OF THE RESONANCE SHIFT

In this section, we calculate the absorption properties of charged SiO_2 particles following the approach by Heinisch *et al.* [32, 33]. Due to the positive electron affinity $\chi > 0$ of SiO_2, the surplus electrons on the particles cause a polarizability $\alpha = 4\pi\mathrm{i}\sigma_\mathrm{b}/\omega$, where σ_b is the bulk conductivity and ω is the frequency of the light. This polarizability changes the refractive index of the material to $N = \sqrt{\epsilon + \alpha}$, where ϵ is the complex dielectric function. The extinction efficiency Q_t can be calculated as

$$Q_\mathrm{t} = -\frac{2}{\rho^2}\sum_{n=1}^{\infty}(2n+1)\mathrm{Re}(a_n^r + b_n^r) \ . \tag{1}$$

Following the notation of Bohren and Hunt, the Mie scattering coefficients can be written as [45]

$$a_n^r = \frac{\psi_n(N\rho)\psi_n'(\rho) - N\psi_n'(N\rho)\psi_n(\rho)}{N\psi_n'(N\rho)\xi_n(\rho) - \psi_n(N\rho)\xi_n'(\rho)} \ , \tag{2}$$

$$b_n^r = \frac{\psi_n'(N\rho)\psi_n(\rho) - N\psi_n(N\rho)\psi_n'(\rho)}{N\psi_n(N\rho)\xi_n'(\rho) - \psi_n'(N\rho)\xi_n(\rho)} \ . \tag{3}$$

Here, $\rho = 2\pi a/\lambda$ is the size parameter with the radius a of the scattering particle and the wavelength λ. The Riccati-Bessel functions are defined as

$$\psi_n(\rho) = \sqrt{\frac{\pi\rho}{2}}J_{n+\frac{1}{2}}(\rho) \ , \tag{4}$$

$$\xi_n(\rho) = \sqrt{\frac{\pi\rho}{2}}H^{(1)}_{n+\frac{1}{2}}(\rho) \ , \tag{5}$$

TABLE I. Optical constants of SiO_2. ν_TO, γ, $4\pi\varrho$, ϵ_0 and ϵ_∞ from [47], λ_LO^{-1} from [48, 49] using ν_{TO_7}, m^* from [50].

j	1	2	3	4	5	6	7
ν_TO (cm^{-1})	394	450	697	797	1072	1163	1227
γ	0.007	0.009	0.012	0.009	0.0071	0.006	0.11
$4\pi\varrho$	0.33	0.82	0.018	0.11	0.67	0.010	0.009
λ_LO^{-1} (cm^{-1})	1661.5						
ϵ_0	2.356						
ϵ_∞	4.32						
m^*	0.42 m_e						

with the Bessel function of first kind $J_n(\rho)$ and the Hankel function of first kind $H_n^{(1)}(\rho)$ [46]. Their derivatives with regard to the argument are marked with a prime.

According to Spitzer and Kleinman [47], the complex dielectric function $\epsilon = \epsilon' + \mathrm{i}\epsilon''$ is

$$\epsilon'(\nu) = \epsilon_0 + \sum_j 4\pi\varrho_j\nu_j^2\frac{\nu_j^2 - \nu^2}{(\nu_j^2 - \nu^2)^2 + \gamma_j^2\nu^2\nu_j^2)} \ , \tag{6}$$

$$\epsilon''(\nu) = \sum_j 4\pi\varrho_j\nu_j^2\frac{\gamma_j\nu\nu_j}{(\nu_j^2 - \nu^2)^2 + \gamma_j^2\nu^2\nu_j^2)} \ , \tag{7}$$

using an oscillator approach with the strength ϱ_j, width γ_j and frequency ν_j. In addition, the bulk conductivity becomes

$$\sigma_\mathrm{b}(\omega) = \frac{e^2 n_\mathrm{b}}{m^*}\frac{\mathrm{i}}{\omega + M(\omega)} \tag{8}$$

with the elementary charge e, the bulk electron density n_b, the conduction band effective mass m^* [32]. The memory function is

$$M(\omega) = \frac{4e^2\sqrt{m^*\omega_\mathrm{LO}\delta}(\epsilon_\infty^{-1} - \epsilon_0^{-1})}{3\sqrt{(2\pi\hbar)^3}}\int_{-\infty}^{\infty}\frac{j(-\bar{\nu}) - j(\bar{\nu})}{\bar{\nu}(\bar{\nu} - \nu - \mathrm{i}0^+)}\,\mathrm{d}\bar{\nu} \tag{9}$$

with

$$j(\nu) = \frac{\mathrm{e}^\delta}{\mathrm{e}^\delta - 1}|\nu+1|\mathrm{e}^{-\delta(\nu+1)/2}K_1(\delta|\nu+1|/2) + \frac{\mathrm{e}^\delta}{\mathrm{e}^\delta - 1}|\nu-1|\mathrm{e}^{-\delta(\nu-1)/2}K_1(\delta|\nu-1|/2) \ , \tag{10}$$

where $\nu = \omega/\omega_\mathrm{LO}$, $\delta = \beta\hbar\omega_\mathrm{LO}$, 0^+ is a small floating point number and $K_1(x)$ is a modified Bessel function (MacDonald function) [46].

Now, we use the constants from Tab. I to calculate the dielectric function with (6) and (7). The interesting spectral range is around 1100 cm^{-1}. The bulk conductivity is calculated using the bulk electron density. From OML theory [5, 51], the number of electrons Z_d on our 40 nm radius SiO_2 particles can be estimated to be of the order of a few hundred elementary charges. Hence, for

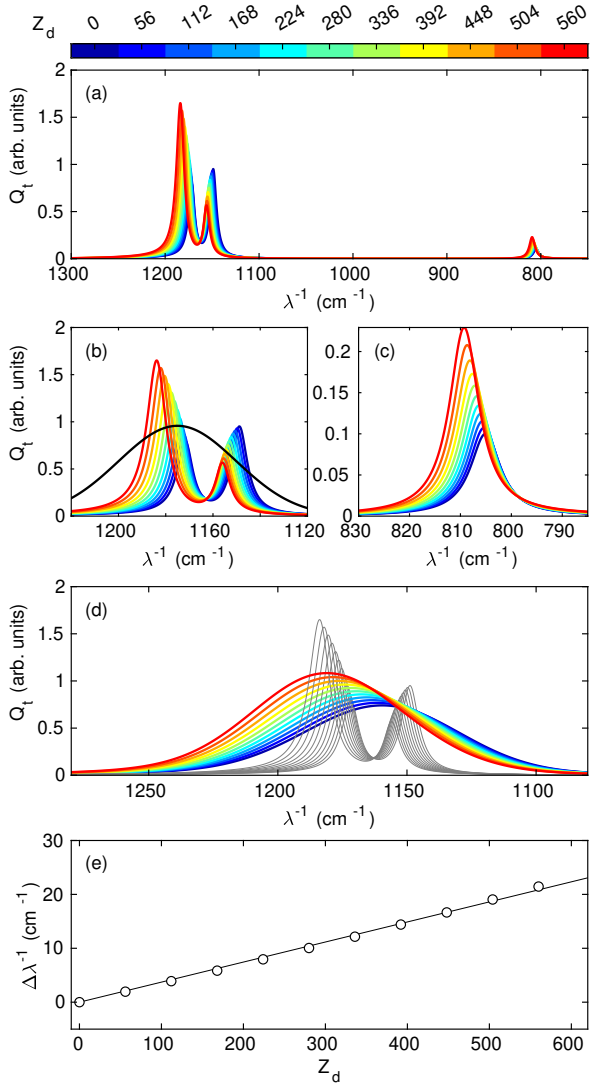

FIG. 5. Calculation of the extinction efficiency Q_t of SiO_2 nanoparticles of 40 nm radius at different charge levels. (a) General overview of the spectra with extinction peaks at around 1180 cm^{-1}, 1150 cm^{-1} and 800 cm^{-1}. (b) Detailed view of the spectra in the spectral range from 1250 cm^{-1} to 1100 cm^{-1} and the used Gaussian (black, not to scale in Q_t-direction). (c) Detailed view of the spectra in the spectral range around 800 cm^{-1}. (d) Convolution of the spectra and the Gaussian from (b) [colored, not to scale in Q_t-direction. Gray curves show the original spectra as in (b)]. (e) Shift of the maximum position of the convolution $\Delta\lambda^{-1}$ in dependence of the particle charge Z_d.

the analysis we assume the charges to be in the range of $0 \leq Z_d \leq 600$. The bulk electron density then is

$$n_b = \frac{Z_d}{V} = \frac{3Z_d}{4\pi a^3} \quad . \tag{11}$$

With that, we now determine the polarizability and the refractive index N of SiO_2 using (2) and (3) to obtain the scattering coefficients and finally using (1) to derive the extinction efficiency Q_t.

The calculated extinction efficiencies are shown in Fig. 5a for various charge numbers on the particle. A major extinction feature is found in form of two peaks at around 1180 cm^{-1} and 1150 cm^{-1}. In addition, a rather small extinction is present at around 800 cm^{-1} (more detailed in Fig. 5c).

It can be seen, that all extinction structures change with the charge on the particles towards larger wavenumbers as expected [32, 33]. The more detailed view in Fig. 5b shows the two peaks around 1180 cm^{-1} and 1150 cm^{-1}. Both peaks shift with dust charge. Moreover, there also is a change of the amplitude of the absorption efficiency with dust charge. While the amplitude of the extinction peak at around 1150 cm^{-1} decreases with the charge, the amplitude of the peak at 1180 cm^{-1} increases with the charge. The shift of the peaks is in the range of about 7 cm^{-1} for the 1150 cm^{-1} extinction and about 11 cm^{-1} for the 1180 cm^{-1} extinction when changing the charge from 0 to 600 elementary charges.

Comparing the calculated (Fig. 5) and measured (Fig. 2) spectra, we see some differences. In our measurements, we only detect a single, rather broad absorption peak around 1100 cm^{-1}, while in the calculations we see two peaks around 1180 cm^{-1} and 1150 cm^{-1}. The width of the measured absorption feature is about 250 cm^{-1}, while the calculated peaks are much narrower with a width of 15 cm^{-1} to 25 cm^{-1}.

Possible reasons for the mentioned differences might be the limited resolution of the FTIR spectrometer, a size (and thus charge) distribution of the dust, material inhomogeneities etc. which all lead to a broadening of the signal.

To take these factors into account, it seems reasonable to convolute the calculated peaks with a Gaussian as indicated in Fig. 5b. The convolution of the calculated extinction efficiencies Q_t and the Gaussian can be seen in Fig. 5d. The Gaussian convoluted calculations now feature a single peak. The convoluted calculations not only react to the individual shift of the two components, but also the change of the amplitudes of the constituent peaks. The shift of the maximum position of the convolution is now larger than the single-peak shifts due to the different change of the amplitudes of the two peaks.

Hence, SiO_2 provides us with the fortunate situation of two close peaks with a charge-dependent changing amplitude, that in the convoluted amplitude results in a larger shift than the two peaks individually. With this combined effect the charge-dependent shift becomes measurable even for the broad peak seen in the experiment.

We finally determine the maximum position of the calculated, Gaussian convoluted combination of the two absorption peaks with changing dust charges, see Fig. 5e. The maximum shifts from 1159 cm^{-1} at zero charge to 1179 cm^{-1} at 600 elementary charges. We see a nearly

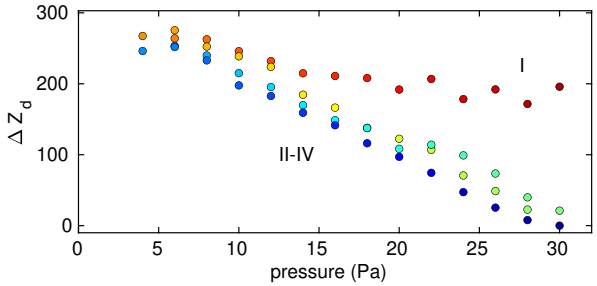

FIG. 6. Derived change of the particles charge as a function of the gas pressure.

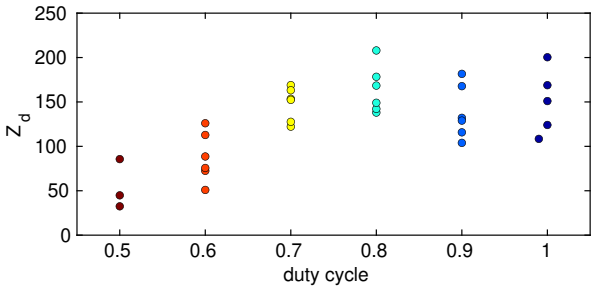

FIG. 7. Derived charge of the particles confined in the pulsed plasma environment at different duty cycles.

linear relation between charge and shift, and we find a relation of charge and the relative charge-dependent shift of

$$\Delta\lambda^{-1}(Z_\mathrm{d}) = 0.0365\,\mathrm{cm}^{-1} \cdot Z_\mathrm{d} \quad . \tag{12}$$

From that, now the charges on the SiO_2 particles can be retrieved.

In our measured FTIR spectra, the absorption peak of interest shows up around $1100\,\mathrm{cm}^{-1}$, and another smaller peak at around $730\,\mathrm{cm}^{-1}$, see Fig. 2a. The calculations show peaks at around $1175\,\mathrm{cm}^{-1}$, see Fig. 5d and $804\,\mathrm{cm}^{-1}$ see Fig. 5c. We see, that the measured spectra are shifted with respect to the calculations by about $72\,\mathrm{cm}^{-1}$. The calculations of the extinction efficiency are sensitive to the optical constants mentioned in Tab. I. The optical constants could be adjusted to match the observed position of the absorption features. However, the absolute position is not of such a vital importance as the relative shift due to the charging.

V. EXTRACTING THE PARTICLE CHARGES

A. Pressure variation

Returning to the measurements, we now will combine the calculated shifts with the experimental results to extract the dust charge. From the shift of the measured IR absorption $\Delta\lambda^{-1}$ in Fig. 3c, we find the relative dust charge ΔZ_d from (12) as shown in Fig. 6. As mentioned above, we have set the position of zero shift ($\Delta\lambda^{-1} = 0$) to the minimum at 30 Pa. The relative charge difference in comparison to the particle charge at 30 Pa is about 280 elementary charges at 4 Pa. For decreasing argon gas pressures, the relative charge increases nearly linearly. The ramping runs II to IV reproduce very similar results.

Measurements from Ratynskaia *et al.* [41] and calculations from Khrapak *et al.* [42] showed a clear inverse proportional dependence of the particles charge on the neutral gas pressure ($Z_\mathrm{d} \sim 1/p$). In our measurements such a clear $1/p$ dependency cannot be seen. Ratynskaia *et al.* investigated on a pressure range from 20 Pa to 100 Pa and Khrapak *et al.* between 20 Pa and 150 Pa, while our measurements take account for the pressure range from 4 Pa to 30 Pa. Hence, our used pressure range is only somewhat overlapping with the other studies. In addition, we are only investigating relative charge differences with respect to our measurement at 30 Pa, while the other studies determined absolute charges.

With these differences between the mentioned studies and our experiments it is hard to compare the results in detail. Nevertheless, the general trend of decreasing particle charges with increasing gas pressure can be confirmed.

B. Pulsed plasma

Since we expect a linear dependence of duty cycle and time averaged charge, the charge of the particles can be determined absolutely by assuming that at duty cycle 0 % the charge on the particles is $Z_\mathrm{d} = 0$, see Figs. 4 and 7. The resulting charge ranges for the particles in the continuously driven plasma environment (duty cycle of 1) between 150 and 200 elementary charges. With reduced duty cycle, the determined charge goes down to about 50 to 100 elementary charges at a minimal applied duty cycle of 0.5. Concerning the accuracy of the results it has to be mentioned, that the values scatter rather strongly with ranges of up to 80 elementary charges.

C. Discussion

To further put our results into perspective, we now study the particle charge from OML theory [5, 51]. We assess the electron temperature to be of the order of $T_\mathrm{e} = 3\,\mathrm{eV}$ [52]. This results in a charge of 168 elementary charges for our particles of 40 nm radius. With respect to our charge measurements, this fits rather fine into the range of the charges of the continuously driven plasma in the pulsing approach, see Fig. 7.

Considering ion-neutral collisions in the charging process, a change of the particle charge of about 40 elementary charges in the pressure range from 4 Pa to 30 Pa

would be expected following Khrapak *et al.* [42]. This is about half a magnitude smaller than our derived change in the particle charge.

Taking into account, that the electron temperature in the mentioned pressure range might also be of the order of up to $8 - 9\,\mathrm{eV}$ [42], the calculated OML charge would rather be in the order of 500 elementary charges for dense dust clouds. Hence, the charges derived from our experimental data seem to be rather in the lower range of the reasonable charges estimated from OML theory. Nevertheless, in such dense plasmas electron depletion also known as the Havnes effect [53] becomes important. This effect especially occurs in dusty plasmas with submicron to nanometer sized particles, where a large fraction of the free electrons is bound to the particles [17, 31, 39].

We now want to compare both of our measurements. From the experiment with varying duty cycles of the plasma power we have derived a charge of about 170 elementary charges at an argon gas pressure of 10 Pa. From our pressure variation measurement, a relative charge difference of about 200 elementary charges at 10 Pa in comparison to 30 Pa can be estimated. With regard to the uncertainties that can clearly be seen in the duty cycle variation measurements (Fig. 7), both results are generally in agreement with each other. Nevertheless, combining both results and extrapolating an absolute charge at 30 Pa by taking $Z \approx 170$ at 10 Pa and subtracting the relative charge change between 10 Pa and 30 Pa of $\Delta Z \approx 200$ would imply nearly no charges at argon gas pressures of 30 Pa. Assuming a small charge of about $Z_\mathrm{d} = 50$ at a pressure of 30 Pa would fulfill $Z_\mathrm{d} \sim 1/p$, which is in good agreement with Ref. [42]. Especially with the rather large scatter of the duty cycle variations both approaches (variation of the pressure and variation of the duty cycle) still seem to be reasonably compatible with each other.

Furthermore, in the pressure variation approach, the applied plasma power is only 15 W, while for the pulsing a power of 50 W at continuously driven plasma has been applied. Although the plasma power is not expected to change the electron temperature that drastically, the measurement conditions are still different. Therefore, the different conditions are additional potential factors for differences in the results of both methods.

In addition, it has been reported, that the particle temperature can also play a role on the absorption properties. In the study [35] the temperature of melamine-formaldehyde particles has been investigated in dependence of plasma exposure by FTIR spectrometer measurements. It has been shown, that with increasing temperature, some of the particles absorption peaks shift to lower wavenumbers, thus in the opposite direction of the shift of increasing charges. This might lower the shift caused by the charge of the particles. We have tested the temperature dependence of the absorption and did not find a significant dependence in a reasonable temperature range for the SiO_2 particles.

However, comparing our method with other charge diagnostics we still want to mention some advantages. As mentioned in Sec. I, a hand full of techniques for charge measurements are available and have been widely used for microparticles. But when it comes to nanodusty plasmas the diagnostics rely on the existence of dust-density waves in the plasma. With our approach not only systems without dust-density waves are examinable, but the diagnostic is also independent of the knowledge of other plasma parameters like the electron temperature or the particle densities of the several plasma species. Nevertheless, the technique is not applicable to all types of material, yet. The advantage of rather well known optical properties of silica allows us to develop this diagnostic for silica nanoparticles. In contrast, typical particle materials (e.g. melamine formaldehyde) are lacking the availability of the necessary parameters.

Besides laboratory plasmas the approach might also be useful for diagnostics in astrophysical dusty plasmas. The optical, non-invasive access to the particle charge by investigating the shift of the absorbing phonon resonance is a great advantage. In addition, the non-invasivity of our method can be of high interest especially for industrial manufacturing processes.

VI. CONCLUSIONS

To sum up, we have measured the IR absorption of SiO_2 nanoparticles of 40 nm radius confined in a plasma. Plasma conditions (pressure and duty cycle of the RF power) have been varied to cause a change of the particle charge. We have observed a clear change in the position of the particles' major absorption peaks with changing plasma conditions. Calculating the extinction efficiency of silica nanoparticles with respect to changes in the charge of the particles, we found a shift of the major absorption peaks towards higher wavenumbers with increasing particle charge. Combining experiment and theory, we were able to deduce a relative change in dust charge with changing gas pressure. By varying the duty cycle it was even possible to estimate the absolute charge of the particles. In general, the results of this novel approach of a charge estimation are in good agreement with OML theory and other experimental charge measurements. In conclusion, this technique provides us with a non-invasive charge diagnostic that is applicable to nanodusty plasmas.

ACKNOWLEDGMENTS

We would like to thank P. Druckrey for the technical support in the preparation phase of the experiments. We gratefully acknowledge previous work from R.L. Heinisch which provides a basis for the current study. This work was financially supported by the Deutsche Forschungsgemeinschaft via Project DFG 1534 Me8-1.

[1] F. Verheest, *Waves in dusty space plasmas* (Kluwer Academic Publishers, Dordrecht, 2000).
[2] P. K. Shukla and A. A. Mamun, *Introduction to dusty plasma physics* (Institute of Physics Publ., Bristol, 2002).
[3] P. M. Bellan, *Fundamentals of Plasma Physics* (Cambridge University Press, 2006).
[4] A. Piel, *Plasma Physics: An Introduction to Laboratory, Space, and Fusion Plasmas* (Springer, Cham, 2017).
[5] A. Melzer, *Physics of Dusty Plasmas: An Introduction* (Springer International Publishing, 2019).
[6] E. Thomas, Potential profiles obtained from applied dust cloud perturbations, Phys. Plasmas **9**, 17 (2002).
[7] V. Nosenko, J. Goree, and A. Piel, Laser method of heating monolayer dusty plasmas, Phys. Plasmas **13**, 032106 (2006).
[8] Y. Feng, J. Goree, and B. Liu, Accurate particle position measurement from images, Rev. Sci. Instrum. **78**, 053704 (2007).
[9] J. D. Williams, Application of tomographic particle image velocimetry to studies of transport in complex (dusty) plasma, Phys. Plasmas **18**, 050702 (2011).
[10] B. Buttenschön, M. Himpel, and A. Melzer, Spatially resolved three-dimensional particle dynamics in the void of dusty plasmas under microgravity using stereoscopy, New J. Phys. **13**, 059601 (2011).
[11] M. Himpel, C. Killer, B. Buttenschön, and A. Melzer, Three-dimensional single particle tracking in dense dust clouds by stereoscopy of fluorescent particles, Phys. Plasmas **19**, 123704 (2012).
[12] M. Himpel and A. Melzer, Three-dimensional reconstruction of individual particles in dense dust clouds: Benchmarking camera orientations and reconstruction algorithms, Journal of Imaging **5**, 28 (2019).
[13] C. Hollenstein, The physics and chemistry of dusty plasmas, Plasma Phys. Controlled Fusion **42**, R93 (2000).
[14] U. Kortshagen, Nonthermal plasma synthesis of nanocrystals: Fundamentals, applications, and future research needs, Plasma Chem. Plasma Process. **36**, 73 (2016).
[15] L. Boufendi, M. C. Jouanny, E. Kovacevic, J. Berndt, and M. Mikikian, Dusty plasma for nanotechnology, J Phys D: Appl Phys **44**, 174035 (2011).
[16] Thomas Jr. E, Merlino R L and Rosenberg M, Magnetized dusty plasmas: the next frontier for complex plasma research, Plasma Phys. Controlled Fusion **54**, 124034 (2012).
[17] B. Tadsen, F. Greiner, and A. Piel, On the amplitude of dust-density waves in inhomogeneous dusty plasmas, Phys Plasmas **24**, 033704 (2017).
[18] F. Greiner, A. Melzer, B. Tadsen, S. Groth, C. Killer, F. Kirchschlager, F. Wieben, I. Pilch, H. Krüger, D. Block, A. Piel, and S. Wolf, Diagnostics and characterization of nanodust and nanodusty plasmas, The European Physical Journal D **72**, 10.1140/epjd/e2017-80400-7 (2018).
[19] B. Tadsen, F. Greiner, and A. Piel, Probing a dusty magnetized plasma with self-excited dust-density waves, Phys. Rev. E **97**, 033203 (2018).
[20] A. Melzer, T. Trottenberg, and A. Piel, Experimental determination of the charge on dust particles forming coulomb lattices, Phys. Lett. A **191**, 301 (1994).
[21] T. Trottenberg, A. Melzer, and A. Piel, Measurement of the electric charge on particulates forming coulomb crystals in the sheath of a radiofrequency plasma, Plasma Sources Sci. Technol. **4**, 450 (1995).
[22] A. Homann, A. Melzer, and A. Piel, Measuring the charge on single particles by laser-excited resonances in plasma crystals, Phys. Rev. E **59**, R3835 (1999).
[23] J. Carstensen, H. Jung, F. Greiner, and A. Piel, Mass changes of microparticles in a plasma observed by a phase-resolved resonance method, Phys. Plasmas **18**, 033701 (2011).
[24] A. Melzer, M. Klindworth, and A. Piel, Normal modes of 2d finite clusters in complex plasmas, Phys. Rev. Lett. **87**, 115002 (2001).
[25] A. Melzer, Mode spectra of thermally excited two-dimensional dust coulomb clusters, Phys. Rev. E **67**, 016411 (2003).
[26] K. Qiao, J. Kong, E. V. Oeveren, L. S. Matthews, and T. W. Hyde, Mode couplings and resonance instabilities in dust clusters, Phys. Rev. E **88**, 043103 (2013).
[27] S. Nunomura, J. Goree, S. Hu, X. Wang, A. Bhattacharjee, and K. Avinash, Phonon spectrum in a plasma crystal, Phys. Rev. Lett. **89**, 035001 (2002).
[28] S. Nunomura, J. Goree, S. Hu, X. Wang, and A. Bhattacharjee, Dispersion relations of longitudinal and transverse waves in two-dimensional screened coulomb crystals, Phys. Rev. E **65**, 066402 (2002).
[29] V. Nosenko, J. Goree, Z. W. Ma, and A. Piel, Observation of shear-wave mach cones in a 2d dusty-plasma crystal, Phys. Rev. Lett. **88**, 135001 (2002).
[30] L. Couëdel, V. Nosenko, A. V. Ivlev, S. K. Zhdanov, H. M. Thomas, and G. E. Morfill, Direct observation of mode-coupling instability in two-dimensional plasma crystals, Phys. Rev. Lett. **104**, 195001 (2010).
[31] B. Tadsen, F. Greiner, S. Groth, and A. Piel, Self-excited dust-acoustic waves in an electron-depleted nanodusty plasma, Phys Plasmas **22**, 113701 (2015).
[32] R. L. Heinisch, F. X. Bronold, and H. Fehske, Mie scattering by a charged dielectric particle, Phys. Rev. Lett. **109**, 243903 (2012).
[33] R. L. Heinisch, F. X. Bronold, and H. Fehske, Optical signatures of the charge of a dielectric particle in a plasma, Phys. Rev. E **88**, 023109 (2013).
[34] A. P. Amrute, Z. Łodziana, H. Schreyer, C. Weidenthaler, and F. Schüth, High-surface-area corundum by mechanochemically induced phase transformation of boehmite, Science **366**, 485 (2019).
[35] H. Krüger, E. Sündermann, and A. Melzer, Investigation of the ir absorption of trapped mf particles in a dusty plasma, Plasma Sources Sci. Technol. (2021), submitted.
[36] *Goodfellow GmbH*, Product: Si616008 (2019).
[37] S. Kashu, E. Fuchita, T. Manabe, and C. Hayashi, Deposition of ultra fine particles using a gas jet, Japanese Journal of Applied Physics **23**, L910 (1984).
[38] D. To, R. Dave, X. Yin, and S. Sundaresan, Deagglomeration of nanoparticle aggregates via rapid expansion of supercritical or high-pressure suspensions, AIChE J. **55**, 2807 (2009).
[39] H. Krüger, C. Killer, S. Schütt, and A. Melzer, Characterization of injected aluminum oxide nanoparticle clouds in an rf discharge, Plasma Sources Sci. Technol. **27**, 025004

(2018).

[40] N. Kohlmann, F. Wieben, O. H. Asnaz, D. Block, and F. Greiner, High-precision in-situ size measurements of single microparticles in an rf plasma, Phys. Plasmas **26**, 053701 (2019).

[41] S. Ratynskaia, S. Khrapak, A. Zobnin, M. H. Thoma, M. Kretschmer, A. Usachev, V. Yaroshenko, R. A. Quinn, G. E. Morfill, O. Petrov, and V. Fortov, Experimental determination of dust-particle charge in a discharge plasma at elevated pressures, Phys. Rev. Lett. **93**, 085001 (2004).

[42] S. A. Khrapak, S. V. Ratynskaia, A. V. Zobnin, A. D. Usachev, V. V. Yaroshenko, M. H. Thoma, M. Kretschmer, H. Höfner, G. E. Morfill, O. F. Petrov, and V. E. Fortov, Particle charge in the bulk of gas discharges, Phys. Rev. E **72**, 016406 (2005).

[43] C. Cui and J. Goree, Fluctuations of the charge on a dust grain in a plasma, **22**, 151 (1994).

[44] T. Nitter, Levitation of dust in rf and dc glow discharges, Plasma Sources Science and Technology **5**, 93 (1996).

[45] C. F. Bohren and A. J. Hunt, Scattering of electromagnetic waves by a charged sphere, Can. J. Phys. **55**, 1930 (1977).

[46] I. Bronshtein, K. Semendyayev, G. Musiol, and H. Mühlig, *Handbook of Mathematics* (Springer-Verlag Berlin Heidelberg, 2015).

[47] W. G. Spitzer and D. A. Kleinman, Infrared lattice bands of quartz, Phys. Rev. **121**, 1324 (1961).

[48] Y. D. Glinka and M. Jaroniec, Shape-selective raman scattering from surface phonon modes in aggregates of amorphous sio2 nanoparticles, J. Appl. Phys. **82**, 3499 (1997).

[49] R. H. Lyddane, R. G. Sachs, and E. Teller, On the polar vibrations of alkali halides, Phys. Rev. **59**, 673 (1941).

[50] M. I. Vexler, S. E. Tyaginov, and A. F. Shulekin, Determination of the hole effective mass in thin silicon dioxide film by means of an analysis of characteristics of a MOS tunnel emitter transistor, J Phys : Condens Matter **17**, 8057 (2005).

[51] H. M. Mott-Smith and I. Langmuir, The theory of collectors in gaseous discharges, Phys. Rev. **28**, 727 (1926).

[52] M. Klindworth, O. Arp, and A. Piel, Langmuir probe diagnostics in the impf device and comparison with simulations and tracer particle experiments, J Phys D: Appl Phys **39**, 1095 (2006).

[53] O. Havnes, C. K. Goertz, G. E. Morfill, E. Grün, and W. Ip, Dust charges, cloud potential, and instabilities in a dust cloud embedded in a plasma, J. Geophys. Res. Space Phys. **92**, 2281 (1987).

6.3 A2 - Investigation of the IR absorption of trapped MF particles in a dusty plasma

Harald Krüger, Eric Sündermann, and André Melzer

Plasma Sources Science and Technology, in press (2021)

Plasma Sources Sci. Technol.

Investigation of the IR absorption of trapped MF particles in a dusty plasma

Harald Krüger, Eric Sündermann, André Melzer

University of Greifswald, 17489 Greifswald, Germany

E-mail: harald.krueger@physik.uni-greifswald.de

Abstract. Infrared (IR) absorption spectra of melamine-formaldehyde (MF) microparticles confined in an rf plasma are studied at different plasma conditions. Several absorption peaks have been analyzed in dependence of plasma power and their temporal evolution. For comparison, the IR absorption spectra of heated MF microparticles without plasma exposition are used to determine the general influence of the temperature on the IR spectra. Measuring the temperature of the particles inside the plasma shows that the temperature is not the only process changing the particles' IR spectra. Chemical changes of the MF particles with increasing plasma power influence the absorption peak structure.

1. Introduction

Plasmas with additional micron to submicron sized particles - so called colloidal or dusty plasmas - have been investigated in an increasing number of situations. Naturally occurring dusty plasmas are usually found in diverse environments like the rings of Saturn, in cometary tails or human-made in plasmas of manufacturing processes for e.g. the production of computer chips [1, 2, 3, 4, 5]. In technological situations particles formed and grown in low-pressure plasmas often emerge from carbon or silicon containing reactive gases. They usually are in the nanometer to submicron size range. For fundamental studies of colloidal plasmas a typical approach is to use externally manufactured micro- or nanoparticles. One of the most widely used particle material is melamine formaldehyde (MF) available in a large variety of sizes, typically in the micrometer range.

In general, inside the plasma the particles gain a negative charge from ion and electron fluxes to the particle. This negative charge results in a strong electrostatic interaction between particles. Hence, in such colloidal plasmas the particles can arrange in ordered structures, such as Coulomb crystals [6, 7, 8], Coulomb clusters [9, 10, 11], or 3D extended dust clouds [12, 13, 14]. The ordering process is counteracted by the random thermal motion of the dust particles as expressed by the kinetic temperature of the dust. Hence, the kinetic temperature is an important and widely studied quantity [15, 16, 17, 18].

Often, argon is used as a background gas in the plasma discharges. As a noble gas, chemical interactions with the microparticles are expected to be on a far lower level than in reactive gases like oxygen. Nevertheless, it has been reported, that argon plasmas can severely change the surface structure and also the size of particles [19]. Hence, it is of high interest to get an insight into the processes and changes happening to the chemical constitution of the particles during plasma exposition.

Here, we measure the power dependent infrared absorption spectra of melamine formaldehyde micorparticles confined in a plasma environment. The results are being compared to a heated sample without plasma exposition to study the influence of the particles temperature on the IR absorption. An additional measurement of the particles temperature in the plasma environment is used to get to know the impact of the temperature on the changes of the particles IR spectra in the plasma. Finally comparing the structure of the different IR absorption peaks, changes in the chemical bonds of the MF particles in the plasma are revealed.

2. Experiment

Using a Bruker Vertex 80v FTIR spectrometer, the IR absorption spectra of MF particles are measured both for particles trapped in a cloud in a gaseous plasma discharge and for dust in the internal sample compartment of the spectrometer under vacuum conditions, but without a plasma. For that purpose, the spectrometer is equipped with a decoupling device and an additional external detector to be able to use an external plasma chamber, see Fig. 1. This external plasma chamber has an inner diameter of 40 cm. In this plasma chamber, we ignite a capacitively coupled RF discharge (at 13.56 MHz). The MF particles are trapped in the sheath of the discharge. The chamber is equipped with four bigger ports to the side (two for the IR beam with KBr windows, two with regular windows) and a cover with several smaller ports. The lower part of the chamber offers access for power supply, vacuum and gas connections via several additional flanges. A turbo-molecular pump evacuates the device to a base pressure of $\sim 10^{-3}$ Pa. During the operation, a rotary vane pump is used in combination with a butterfly valve and a pressure controller to control the argon gas pressure and flow inside the device. The typical argon gas pressure ranges between 2 Pa and 6 Pa. The argon mass flow is adjusted accordingly to reach these small pressures between 3 sccm and 10 sccm.

In the plasma chamber, there is one single powered electrode with a diameter of 30 cm. Compared to other dusty plasma experiments, this is a rather large electrode. The goal of this large electrode is to be able to confine more particles in the line of sight of the FTIR spectrometer to enhance the absorption by the dust. The rest of the plasma chamber is grounded. Hence, the capacitively coupled RF discharge, powered by an RF generator with powers in the range of up to 60 W in connection with a matching network, is burning between the electrode and the chamber walls. To confine particles in this plasma, an additional metallic potential barrier of 1 cm height, 28 cm length and 10 cm width is located on the electrode. To insert the particles into the plasma environment a dust shaker is used. A dust cloud is formed and trapped in the sheath of this plasma (dust sample I).

MF particles of 3.93 µm diameter are used for the experiments presented here. The trapped dust in the plasma (sample I) is exposed to different plasma conditions. The different flux of electrons and ions to the dust is expected to result in a different heating and chemical changes of the bulk and surface material of the dust. The FTIR spectra are then recorded for the various plasma conditions.

For measuring the spectra of dust inside the chamber, the FTIR beam is guided under vacuum

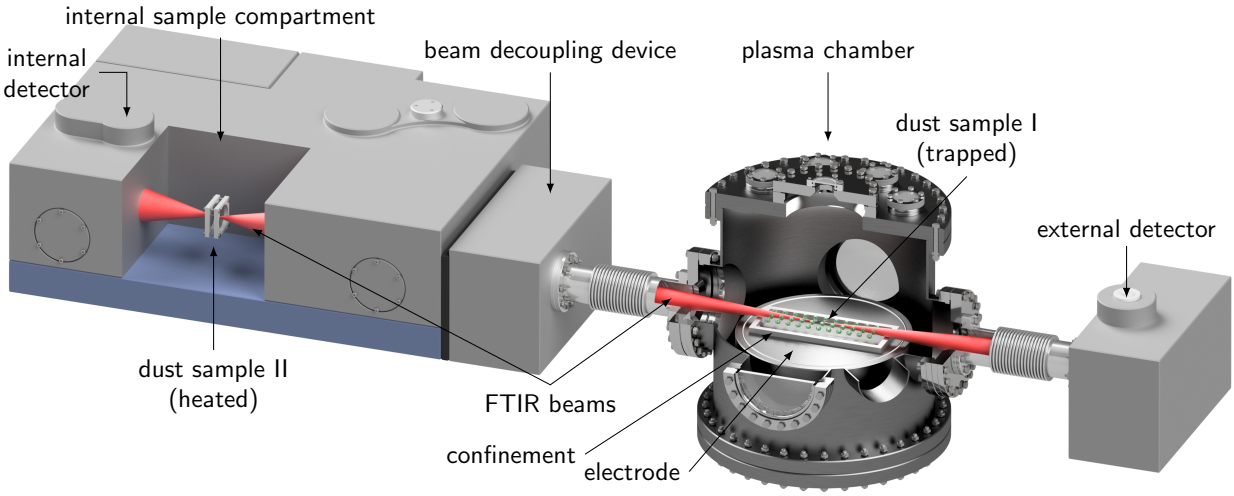

Figure 1. Scheme of the experimental setup with the Bruker Vertex 80v FTIR spectrometer, the FTIR decoupling device, the plasma chamber with one large powered electrode and the FTIR detector. The measurements are taken either on sample I trapped in the plasma environment or on sample II in the sample compartment without plasma.

conditions through the chamber to the external detector. Inside the plasma chamber, the IR beam has a focus of about 10 mm which is positioned about 15 mm above the electrode of the chamber.

A second dust sample (dust sample II) with the same type of particles as the trapped ones is placed on a sample holder in the evacuated internal sample compartment of the FTIR spectrometer (without any plasma). Then, the IR beam is guided through the internal chamber and the dust sample II. FTIR absorption measurements can easily be switched between sample I and II.

The sample holder consists of two KBr windows with a distance of 3 mm and a diameter of 50 mm. A small amount of the dust particles is sprinkled on one of the two windows. Despite the vertical alignment of the windows, a sufficient amount of particles stays attached to the window. The windows are separated from each other by a teflon ring. The dust sample in the holder can also be heated by resistors attached to the sample holder. The teflon separator contains two PT-1000 temperature sensors.

To obtain temperature-dependent absorption spectra without plasma, dust sample II is heated from room temperature to about 180°C by applying different voltages to the heating resistors. The absorption spectra are measured at various temperatures as obtained from the PT-1000 sensors.

We then measure the IR absorption spectra of the particles confined in the plasma as well as the IR spectra of the particles in the internal sample compartment. This way, the measurement of both samples (with and without plasma) can be done nearly simultaneously. Another advantage of using the same FTIR spectrometer is that we use the same IR source and internal beam path setup for both measurements and therefore minimize the risk of uncertainties by using different devices.

3. Results

Here, we present the results of our FTIR absorption measurements of the two dust samples. We start with the spectra of the particles trapped in the plasma, where we measured the absorption as a function of plasma power.

3.1. The IR spectrum of MF particles in the plasma environment

To investigate the behaviour of the MF particles under the influence of the flux of the plasma particles (ions and electrons) on the microparticle, FTIR absorption measurements are carried out with MF particles confined in the sheath of the plasma at different plasma powers in the range from 2 W to 60 W and gas pressures in the range from 2 Pa to 6 Pa. These power and pressure ranges have been found to be suitable to confine a reasonable number of particles in the pathway of the FTIR beam. Figure 2 shows the absorption spectra of the trapped particles (sample I) at an Ar gas pressure of 3 Pa. The interesting part of the spectrum is in the wavenumber range from 1800 cm^{-1} to 750 cm^{-1}, as shown in Fig. 2a). Here, we can see different absorption peaks with a strength of up to 20 %. From this, the particle density can be estimated

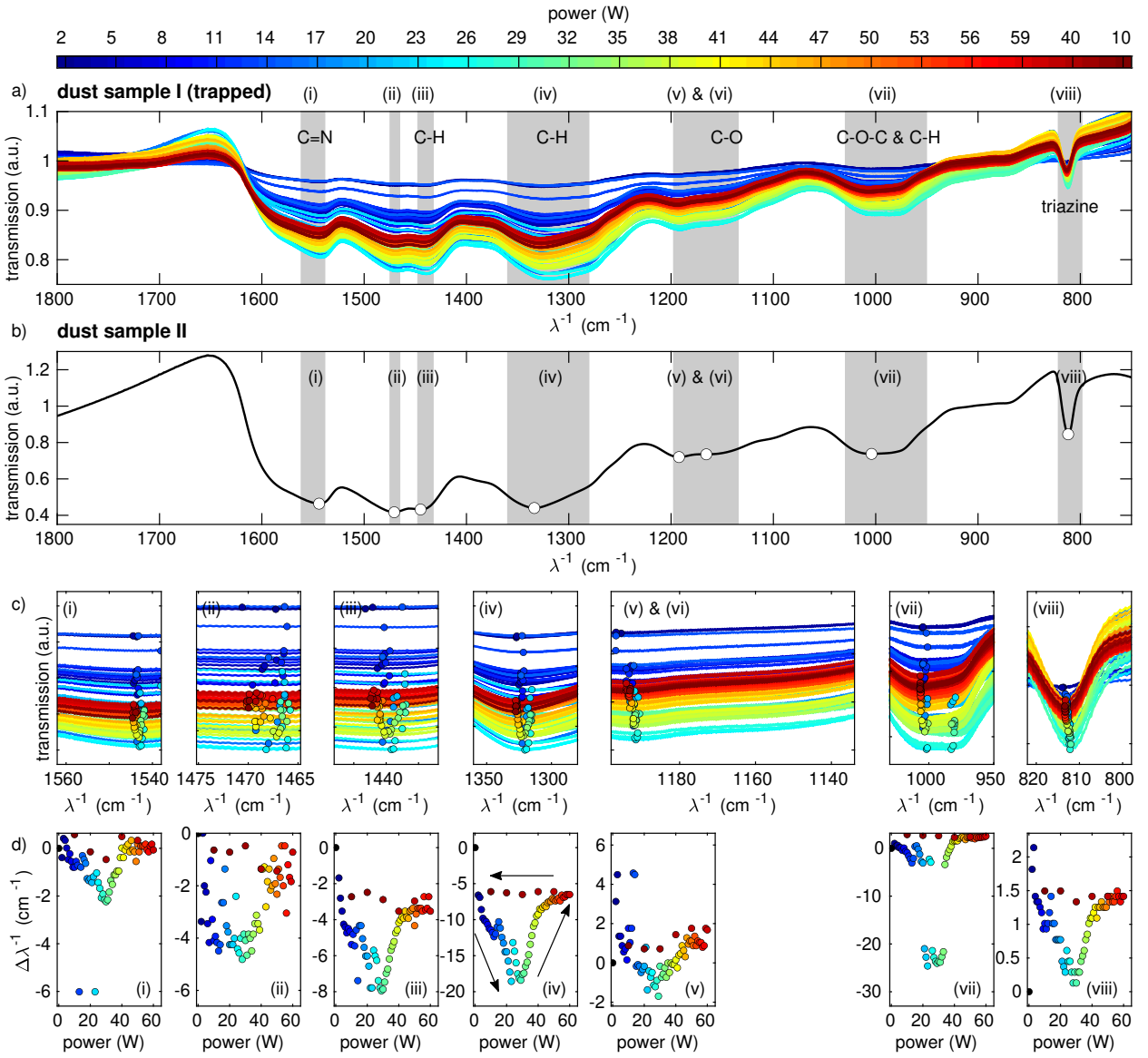

Figure 2. a) IR spectra of MF microparticles confined in an argon plasma (sample I) at different powers indicated by colors at an argon gas pressure of 3 Pa and b) MF microparticles in the sample compartment (sample II). c) Magnified view of the IR spectra in the regions (i)-(viii). The circles denote the minimum positions of the IR spectra for the different plasma powers. d)(i)-(viii) shift of the minimum position of each corresponding peak of sample I in relation to the position in the sample compartment (sample II taken as 0 W). Corresponding molecular vibrations in a) from Merline *et al* [20].

to be of the order of $n_d = 4 \times 10^{11}\,\mathrm{m}^{-3}$. This agrees with other measurements [21].

The chemical properties of the individual peaks will be discussed below in more detail. In the general overview, the spectra seem to differ not very much. The absolute transmission values usually change due to different particle numbers in the pathway of the FTIR beam. For comparison, the spectrum of the MF particles at room temperature in the internal sample compartment (sample II) shows a similar absorption, see Fig. 2b). We now want to investigate the position of the absorption peaks a little more in detail. Hence, in Fig. 2c) we have zoomed into the marked absorption regions (i) to (viii) of Fig. 2a) and b). First, we determine, for each absorption peak, the wavenumber position of maximum absorption. For that purpose, a polynomial of ninth‡ order has been fitted to each peak in the surrounding wavenumber region. From that the

‡ Due to the peaked and rather asymetric geometry of the peaks, ninth order polynomial fits have been used. By reducing the inspected interval, the order of the polynomial fit can be reduced as well, but this does not have an effect on the determined peak position.

position of maximum absorption has been determined for each peak. As mentioned before, the absolute transmission values depend on the actual number of particles in the FTIR beam path. Hence, we focus on the wavenumber position of those peaks. Figure 2d) shows the shift in the position of the absorption peak with respect to the internal dust sample II (zero position) for each peak.

Generally, we see a significant shift with plasma power variation in the range between 2 W and 60 W. Compared to the peak position at the lowest applied plasma power (2 W), the peaks shift to smaller wavenumbers with plasma power. The strongest (negative) shifts are found for plasma powers between 20 W and 30 W. For powers larger than 30 W, the absolute shift decreases again. At 60 W the peaks have shifted back nearly to the starting position at 2 W. The amplitudes of the shifts differ for all the peaks from about $2\,\mathrm{cm}^{-1}$ for peaks (i) and (viii), about $4\,\mathrm{cm}^{-1}$ for peak (ii), $6\,\mathrm{cm}^{-1}$ for peak (v), $8\,\mathrm{cm}^{-1}$ for peak (iii), $20\,\mathrm{cm}^{-1}$ for peak (iv) and up to $25\,\mathrm{cm}^{-1}$ for peak (vii). This extremely strong shift of peak (vii) is due to the double-well-like structure of the absorption. The rather flat and broad minimum of peak (vii) tilts to the other minimum in the power range between 20 W and 35 W and hence, causes a strong gap in the otherwise rather smooth behaviour of the shift.

After increasing the plasma power to 60 W in rather small steps, we decreased the plasma power back to 10 W in bigger steps. Here we see, that the shift stays rather constant over the whole power range. They do not follow the path during power increase. This hysteretic behaviour hints at non-reversible changes of the particles. Asnaz *et al* reported that deep grooves are being formed in the surface of plastic particles by plasma exposure [19]. A possible reason for the observed hysteretic behavior might be that the etched grooves are not refilled with material during the power reduction and hence, a non-reversible process can be assumed. It seems a little counter-intuitive that the shift decreases again for powers above 30 W. Being speculative, one might argue that chemical changes in the lower power range might be cured for higher powers due to the higher plasma activity.

Peak (vi) is clearly identifiable in dust sample II (which is not exposed to the plasma). This peak is hardly discernible in the spectra of the plasma exposed dust sample I. Thus, we have not shown a shift for this peak (vi), see also the discussion in Sec. 3.4.

The influence of the gas pressure of the plasma has also been investigated. We did not observe significant shifts of peaks with gas pressure. For all investigated gas pressures, the shifts of the peak positions with plasma power were very similar.

3.2. The IR spectrum of heated MF particles

It is known that, for materials like MgO and LiF [22] and MF [20, 23, 24], absorption peaks in the IR spectra shift and change structure with increasing temperature. To relate our observed trend of a shift of the different absorption peaks to smaller wavenumbers with increasing plasma power, we now study the influence of an increase of the particle temperature on the shifting of the peaks.

To determine the influence of the temperature, IR spectra of heated dust are measured in the internal chamber (sample II). Therefore, the KBr windows and the dust in between are placed into the internal sample compartment of the FTIR spectrometer and heated by applying a voltage to the mounted resistors to around 180°C. While heating up, several spectra are taken while measuring the sample temperature with a PT-1000 sensor. Figure 3 shows the results of these measurements. Similar as for the particles in the plasma environment, the interesting spectral range is again between $1800\,\mathrm{cm}^{-1}$ and $750\,\mathrm{cm}^{-1}$. Here, the most prominent peaks are marked again and are further analyzed as described in the previous section.

As can be seen in Fig. 3c) and d), some of the peaks' movement show a clear dependence on the temperature [peaks (ii)-(vii)], while for other peaks [(i), (viii)] only marginal shifts are observed.

Peaks (ii)-(vi) show a rather similar trend: the position of minimal transmission shifts towards smaller wavenumbers with increasing temperature. Again, the strength of this shift is different and ranges from $4\,\mathrm{cm}^{-1}$ for peak (iii) to a maximum of $20\,\mathrm{cm}^{-1}$ for peak (vi) in the temperature range from 26°C to 180°C.

Contrary to the peaks (ii) to (vi), peak (vii) shifts towards higher wavenumbers with increasing temperature. This will be further discussed in Sec. 3.4.

Comparing the IR spectra of the heated and the plasma-exposed samples, it can be seen, that the strength of the shift correlates in both samples. In both samples, peak (iv) shifts most strongly, for peaks (ii), (iii) and (v) moderate shifts are observed. Peaks (i) and (viii) that have nearly no shift when heated also show only weak shifts in the plasma environment. In the heated sample peak (vi) can be identified and tracked with temperature in contrast to the plasma-exposed situation.

These results imply, that the particle temperature may cause some of the changes in the absorption spectra in the plasma environment (Fig. 2). Hence, it is necessary to determine the particle temperature inside the plasma environment to judge the influence of temperature and power.

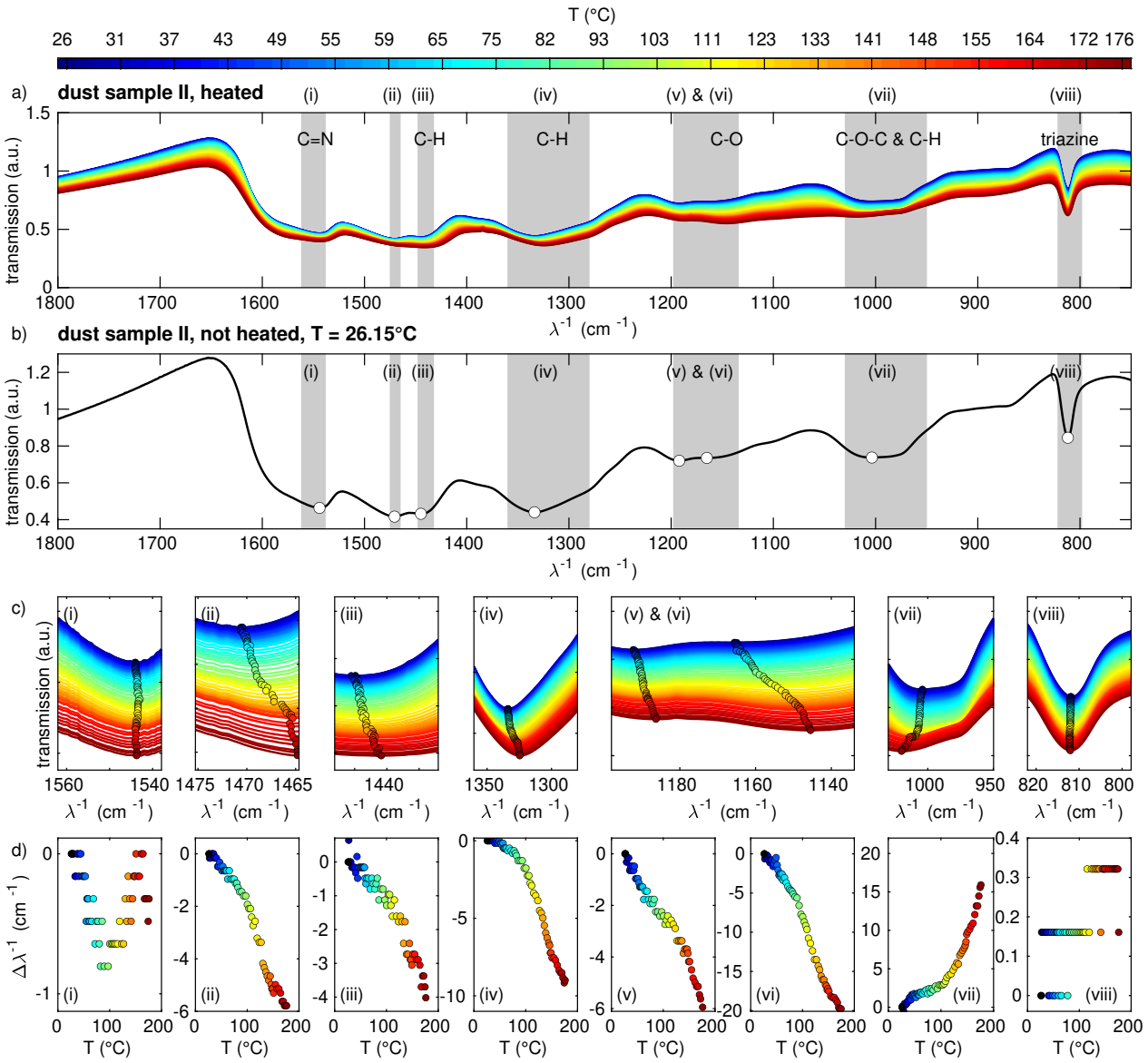

Figure 3. IR spectra of MF microparticles in the internal sample compartment (sample II) at a) different temperatures and b) at room temperature. c) Magnified view of the IR spectra in the regions (i)-(viii). The circles denote the minimum positions of the IR spectra for the different plasma powers. d)(i)-(viii) shift of the minimum position of each corresponding peak in relation to the position at room temperature.

3.3. Determination of the particle temperature inside the plasma

We have determined the particle bulk temperature using the fluorescence of Rhodamine B (RhB)-doped MF particles ($d = 3.87\,\mu m$). This technique has been previously applied to measure dust temperatures in the plasma [25, 26]. There, one exploits that the spectral width of the fluorescence light peak increases with bulk temperature. For such temperature measurements in the plasma, the doped particles are dropped into the discharge just as the regular MF particles. A 532 nm laser sheet illuminates the particles, and excites the fluorescence at around 580 nm. The resulting light emission is measured with a USB-spectrometer. For each measurement a background scan without laser illumination and a sample scan with laser illumination is recorded. We then use the difference of sample spectrum and background spectrum for further analyzing the flourescence emission peak. The absolute height of the fluorescence signal decreases with increasing temperature, while the general width of the peak increases with increasing temperature [25]. Hence, we determined the FWHM as a measure for the

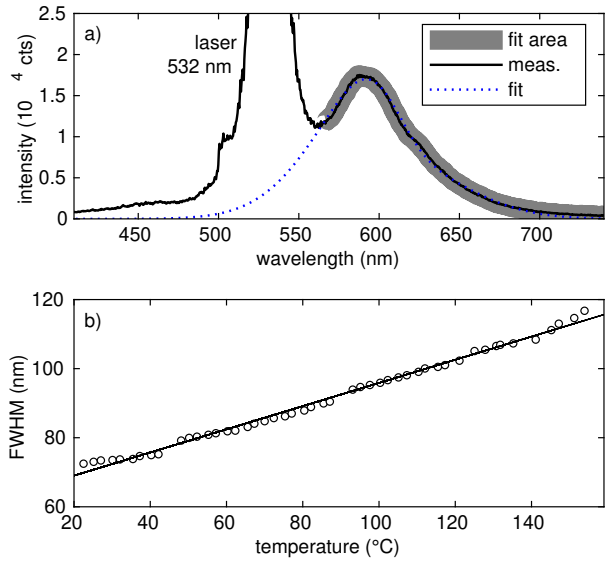

Figure 4. a) Measured emission spectrum of RhB doped MF particles in sample holder II enlightened by a 532 nm laser. In addition to the original measurement the fitted skew normal distribution and the corresponding fitting area are shown. b) Resulting FWHM in dependence of the temperature from the calibration measurements with linear fit.

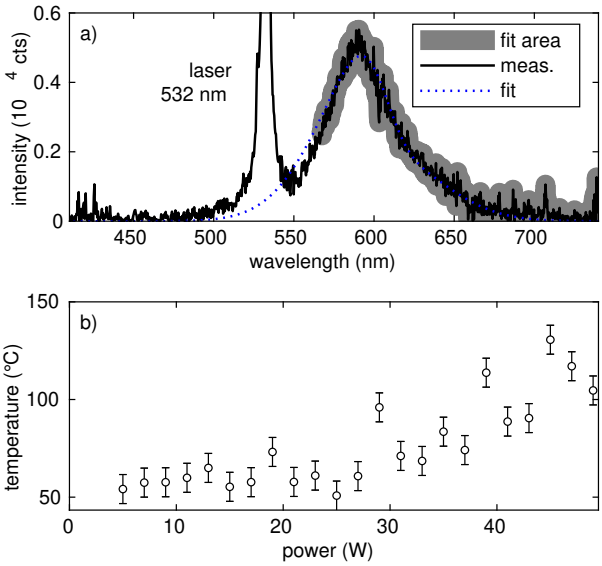

Figure 5. a) Emission spectrum of RhB doped MF particles in the plasma environment enlightened by a 532 nm laser - measurement, fit and fit area. b) Obtained particle temperatures in dependence of the plasma power the fluorescence method.

temperature by fitting a skew normal§ distribution to the peaks intensity

$$I(\lambda) = p_1 \exp\left(-\left(\frac{\lambda - p_2}{p_3}\right)^2\right)\left[1 + \mathrm{erfc}\left(p_4 \frac{\lambda - p_2}{p_3}\right)\right] \quad (1)$$

with the fit parameters p_i and the complementary error function $\mathrm{erfc}(\lambda)$. The FWHM is then derived from p_3 as

$$\mathrm{FWHM} = 2\sqrt{2\ln 2}\,p_3 \ . \quad (2)$$

To extract the temperature from the FWHM of the fluorescent signal, a calibration measurement with defined temperatures has to be done. Killer *et al* [26] dispersed the RhB doped MF particles in glycerol and water, used a heating plate with a magnetic stirrer and illuminated the solution with a laser of 532 nm. As they have shown, the resulting FWHM depends on the used solvent glycerol or water. To make our calibration measurement as comparable as possible with the measurement in the plasma environment, we use our heatable sample holder from the FTIR measurements, where the particles are only in contact with the surrounding air and the KBr windows. We then illuminate the RhB-doped MF particles in between the KBr windows with the same laser as for the measurements in the plasma and measure the temperature depending flourescence spectrum in the range from 20°C to 160°C, see Fig. 4. By comparing the plasma spectral width of the fluorescence of the particles trapped in the plasma and the externally heated particles, a bulk temperature can be obtained, see Fig. 5. Here, we see, that the temperature increases from about 50°C at 5 W to about 100°C at 50 W.

However, combining both FTIR measurements (sample I and II) to determine a temperature from these by using the heated sample (II) as a calibration, one would find significantly higher temperatures. For example, looking at peaks (iii) and (iv) in Figs. 2 and 3, we see a stronger shift of the peaks with the power than with the maximum temperature of 180°C. This would indicate particle temperatures exceeding at least 200°C. Now, one might argue that the temperatures obtained by both methods might be different, like one being the surface and one rather the bulk temperature. However, the particles are transparent in the visible wavelength range and the fluorescent dye is distributed in the particle [27]. Hence, the fluorescence should indicate the temperature of the particle bulk. For the FTIR measurements, the wavenumber range of interest corresponds to wavelengths of 5 µm to 13 µm. We assume, that the IR wave penetrates into the particle of the order of one wavelength. With a particle radius of roughly 4 µm that means, that the IR wave reaches through the whole particle and bulk properties are measured here as well. Hence, the seen changes in the IR absorption cannot only be described by changes in

§ We have fitted differently modified normal distributions to the data. This skew normal distribution has empirically been found to be best fitting for the fluorescent signal.

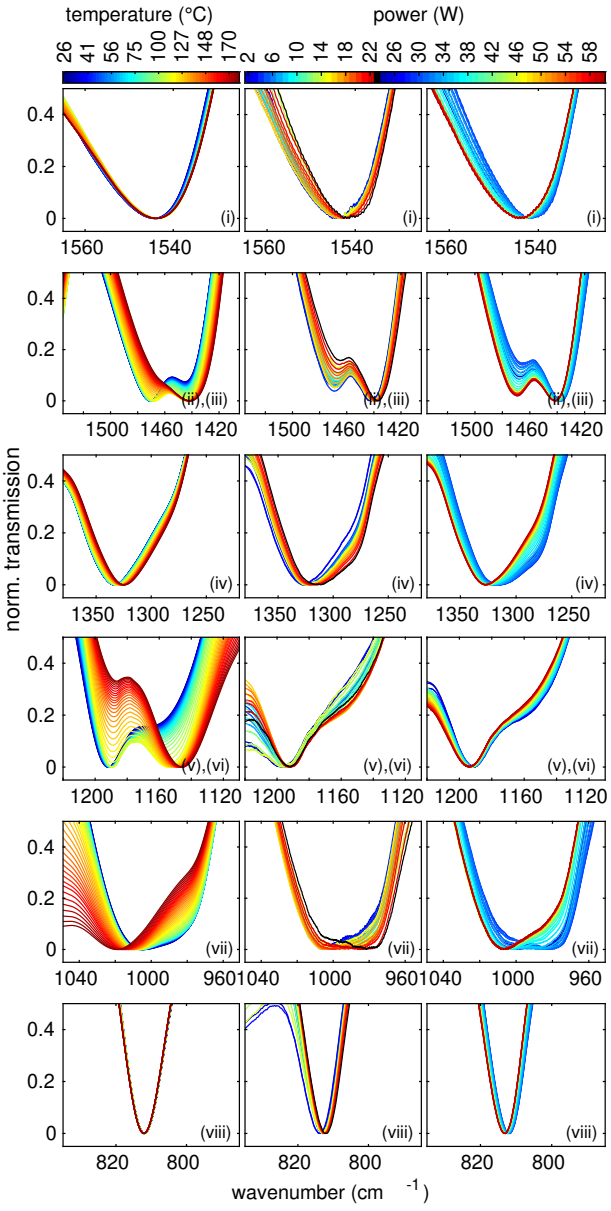

Figure 6. Structural analysis of the absorption peaks of the temperature resolved measurement (first column) and the power resolved measurement (center and right column).

the particle temperature.

3.4. The structure of the peaks

In addition to the temperature-induced shifts of absorption peaks we now take a deeper look into the (chemical) structure of the peaks. For that purpose, we have normalized the single peak structures in their wavenumber interval where the respective maximum transmission is set to 1 and the minimum transmission is set to 0. The normalized transmission is shown in Fig. 6. Here, the different absorption peaks are represented by rows (peaks (ii) and (iii), as well as (v) and (vi) are combined). The left column shows the normalized absorption peaks of the heated sample II. The second and third column show the absorption peaks of sample I in the plasma environment in dependency of the applied power. For the sake of clarity, the power behaviour is split into two columns. The second column shows the measurements in the power range from 2 W to 23 W and the third column for powers between 24 W and 60 W. In the following, we will discuss the change of the structure of the peaks:

For peak (i) the peak structures look quite similar. We see a small shift of the peak with temperature. For the measurement in the plasma environment with powers in the range from 2 W to 23 W a stronger shift with increasing plasma power can be seen. The shift is in the same direction as with temperature. For larger powers, this behaviour is turned around. The shift goes back towards larger wavenumbers again. The main shift seems to happen in the range from 24 W to 35 W. Above this power, the peak does not shift significantly anymore. This peak can be attributed to the C=N bond in the central triazine ring [23]. Here, bigger changes in the structure are not expected since large chemical changes of this central part seem unlikely. Nevertheless, the shift of the absorbance with plasma power is somewhat stronger than it would be expected from a change in the temperature, here. This could hint at changes to the chemical groups attached to the central ring.

Peaks (ii) and (iii) form a double peak structure. In the heated sample II it can be seen, that peak (ii) reduces in strength with rising temperature while peak (iii) becomes the dominant peak. In the plasma sample I peak (iii) is dominant for all powers and does not change that much with power. However, peak (ii) is getting less prominent with increasing power up to 23 W and is getting more prominent for higher powers, again. Both absorptions are caused by methylene (CH_2) and methyl (CH_3) vibrations. Although both bands somewhat overlap, the CH_2 absorption can be attributed to the peak with the higher wavenumber and the CH_3 to the peak at the lower wavenumber [28]. During heating the CH_2 bending seems to nearly vanish while during the plasma exposition both absorption peaks are present. It is interesting to note here that the peak structure even at the lowest plasma powers differs quite clearly from the heated sample. This hints at immediate chemical changes upon plasma exposure.

Similar to peak (i), peak (iv) shifts slightly towards smaller wavenumbers with increasing temperature. In the plasma sample I, this shift can also be seen in the lower power interval with increasing power. In the higher power interval, this shift goes back again

with increasing power. In addition, around a plasma power of 23 W, a knee at about 1275 cm^{-1} develops. This knee does only barely show up in the heated sample II. The main peak structure can be attributed to aromatic amines $C_{Ar}-N$ stretching vibrations in connection with methylene ether or methylene bridges [23]. The formation of the knee structure also clearly indicates chemical changes during plasma exposure.

In the heated sample II the peaks (v) and (vi) form a double peak structure very similar to peaks (ii) and (iii). With increasing temperature, peak (v) is getting less prominent, while peak (vi) evolves from a knee structure to the more prominent peak in this interval. For the plasma measurements (sample I), peak (v) stays the prominent (only) peak for all powers. Peak (vi) does only appear as a knee which is even less prominent at strongest prominence (23 W-24 W) than for the smallest temperature in sample II. This rather little knee gets clearer for powers around 23 W, and vanishes for higher powers, again. Here, peak (v) at 1190 cm^{-1} corresponds to a secondary amines C-N stretch [28]. Peak (vi) at 1150 cm^{-1} indicates the presence of C_R-N stretching vibrations and asymmetric C-O-C vibrations. These only occure dominantely during the heating, while during plasma exposition, an absorption band can hardly be indentified. It should be noted that the C-O-C peak at 1150 cm^{-1} occurs only in MF cured at low temperatures [24]. These C-O-C bridges seem to be destroyed immediately at plasma exposure.

For low temperatures, peak (vii) shows a rather broad structure with a minimum in transmission at roughly 1010 cm^{-1} in addition to a small, but noticeable knee at 980 cm^{-1}. With increasing temperature, this knee gets less prominent and the whole structure shifts towards larger wavenumbers. This is the only peak structure, where a shift towards larger wavenumbers can be seen. In the plasma sample I, it can be seen, that the knee at about 980 cm^{-1} gets more prominent with increasing power up to 23 W and decreases again for further increasing power. Due to this more prominent knee, the direction of shift with temperature is in the opposite direction to the general behaviour of the shift with the plasma power. The attributed C-O stretching vibration at 990 cm^{-1} indicates a loss of methylol functions with increasing temperature. In contrast, with increasing plasma power, it seems like methylol functions increase as well until the break point 23 W. For higher powers a loss of methylol functions can be detected, again [23]. It can be speculated that the missing C-O bonds of peak (vi) partially show up in peak (vii).

The triazine absorption, peak (viii), does not show any changes with the temperature. However, in the plasma sample I, peak (viii) shifts with increasing plasma power up to 23 W towards smaller wavenumbers and shifts back to larger wavenumbers for larger plasma powers, as seen in most other peaks as well. However, this shift is very small, but still larger than with heating. This again indicates changes not to the ring, but to groups attached to the triazine ring.

Concluding on this structure analysis, it can be seen, that the sample I in the plasma environment generally shifts with increasing power up to 23 W towards smaller wavenumbers and shifts back for higher wavenumbers. Changes in the appearance in the structures (ii) and (iii), as well as (v) and (vi) can be explained by the change in the temperature for powers up to 23 W. For higher powers, chemical processes seem to be more effective. Although the temperature has been measured to be rising for powers above 23 W, the shift goes generally back again and does not correlate with the temperature anymore. Hence, we assume, that the influence of the changing of the absorption of the particles is not only temperature induced, but also by plasma chemistry. Especially the changes in peaks (ii)-(vii) indicate chemical changes in the methylene ether and methylene bridges and C-O-C bridges. The absorption bands associated to bindings in or close to the central triazine ring change only little [peaks (i), (iv), (viii)], while the surrounding bindings do change significantly.

Previous studies have shown, that the plasma has significant influence on the particles' size and density distributions. For example, Asnaz *et al* investigated on dusty plasmas with PMMA microparticles [19]. Using different diagnostics, they found not only a decrease of the particles' radius, but also a strong loss of the mass density of the particles with time. Further analysis revealed a roughening of the surface structure, while the mass density of the particle core did not change significantly. An explanation for this behaviour is the impinging of ions accelerated in the plasma sheath. Those ions have a rather short penetration depth of only a few nanometers, but, nevertheless, form grooves in the particles' surface of up to 1 µm, as has been shown in experiments with PMMA foil exposed to non-reactive plasmas [29]. Due to their rather physical than chemical behaviour, we assume that similar processes occur in our experiments as well, although the used material differs from our used MF particles.

But also for experiments with MF microparticles changes in the mass and size have been detected [30, 31, 26, 32]. Kohlmann *et al* found etching rates from −1.25 nm/min to −1.69 nm/min for MF particles causing the particles to shrink [32].

In experiments performed by Killer *et al* [26], a quadrupole mass-spectrometer has been used to investigate on the outgassing/etching components of plasmas with MF particles. They have shown that

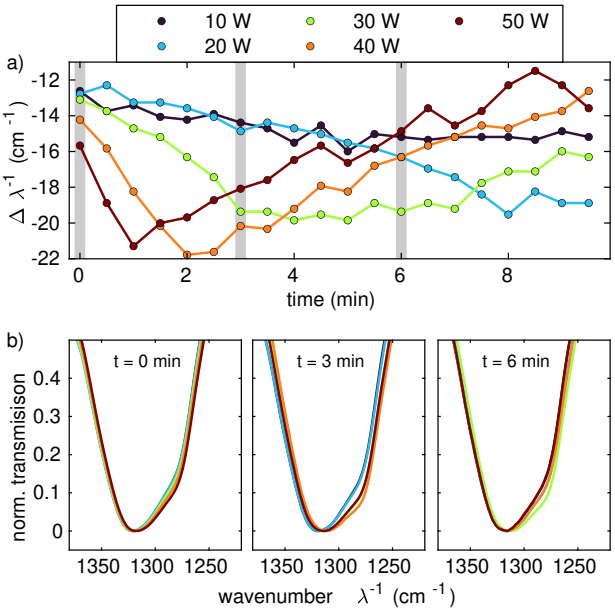

Figure 7. a) Temporal Evolution of the shift of peak structure (iv) at different applied plasma powers. b) Structural analysis of peak (iv) at different applied plasma power at $t = 0, 3, 6$ min.

molecules containing nitrogen, oxygen and carbon are being detected during plasma exposition of the particles. The detected changes in the IR spectra of our measurements can be easily attributed to those base elements and hence, underline our results. Changes in the density of the molecules appeared right after the injection of the MF microparticles. The biggest change of the density for all outgassing/etching components occured within a time scale of less than 5 min after particle injection [26]. Hence, an additional investigation of the temporal evolution of the IR spectra seems reasonable.

3.5. Temporal evolution

Next to the variation of the plasma power and gas pressure in the discharge, it is interesting to investigate the time evolution of the processes mentioned before. Hence, we repeatedly measured the IR absorption spectra at defined time intervals (every 30 s) for different, but constant plasma powers. Exemplarily, we have chosen peak (iv) to display the results in Fig. 7a). Here, we determined the position of minimal transmission in the same way as in Sec. 3.1. As can be seen, the strongest shift is reached right after 1 min of plasma exposition at the highest applied plasma power of 50 W. For lower applied powers, this point is reached later: For 40 W after 2 min, for 30 W after 4 min and for 20 W after 8 min. In the measurement with an applied power of 10 W the minimum has not been reached within the 10 min measurement interval.

In addition to the faster reactions with higher applied plasma powers, we also determined, that the absolute shift at minimal transmission is also depending on the power: The higher the power, the stronger the shift at minimal transmission.

In addition, we have looked at the normalized absorptions in analogy to Sec. 3.4 for the different applied powers at 0 min, 3 min and 6 min, see Fig. 7b). At 0 min, all structures look rather similar, only for the higher powers the knee at 1280 cm^{-1} is slightly stronger pronounced. This behaviour can be seen more clearly at 3 min, where for the two lowest powers (10 W and 20 W) the knee is still not clearly detectable, while for the higher powers this knee is strongly distinct. Here, we can see, that with increasing power a gain of methylol can be identified. After another 3 minutes, the most prominent knee is seen for the medium power of 30 W while for the lower powers the methylol knee did not form yet and for higher powers already formed back.

However, using both methods, it can be seen, that the processes changing the materials chemical structure is both time and power dependent.

4. Summary

We have presented measurements of IR absorption spectra of MF microparticles inside a colloidal plasma. The changes of the absorption with increasing plasma power have been studied. It has been shown, that single absorption peak positions shift and alter their structure during plasma exposition. These changes occured until a defined applied plasma power and were mainly reversed for higher plasma powers. Comparisons of IR absorption measurements with heated microparticles without plasma exposition have shown similar shifts and changes in the peaks' structures with rising temperature, although a reversal of this behaviour could not be indentified in the range of reasonable temperatures. An additional measurement of the particles' bulk temperature showed a general trend of increasing temperature of the particles for increasing plasma powers. Taking this into account, it can be shown, that the temperature is not the only factor for changes in the particles absorption features. The analysis of the chemical changes altering the MF material during heating and plasma exposition revealed a change of the materials chemical composition that shows only little variation of bonds around the central triazine ring of MF but rather the surrounding amine groups and C-H compounds. Especially the reversal of the features with further increasing plasma powers cannot be explained by changes in the temperature. Here, we expect other plasma chemical, etching and outgassing processes to

be accountable for the changes.

Acknowledgments

This work was financially supported by the Deutsche Forschungsgemeinschaft via Project DFG 1534 Me8-1. We would also like to thank P. Druckrey for the technical support in the preparation phase of the experiments.

References

[1] Verheest F 2000 *Waves in dusty space plasmas* (Kluwer Academic Publishers, Dordrecht)

[2] Shukla P K and Mamun A A 2002 *Introduction to dusty plasma physics* (Institute of Physics Publ., Bristol)

[3] Piel A 2017 *Plasma Physics: An Introduction to Laboratory, Space, and Fusion Plasmas* (Springer, Cham) URL https://doi.org/10.1007/978-3-319-63427-2

[4] Bellan P M 2006 *Fundamentals of Plasma Physics* (Cambridge University Press) URL https://www.cambridge.org/core/books/fundamentals-of-plasma-physics/4E88EC98AA7339A290AD0734641A7970

[5] Melzer A 2019 *Physics of Dusty Plasmas: An Introduction* (Springer International Publishing) URL https://www.springer.com/gp/book/9783030202590

[6] Chu J H and I L 1994 *Phys. Rev. Lett.* **72** 4009–4012 URL http://link.aps.org/doi/10.1103/PhysRevLett.72.4009

[7] Hayashi Y and Tachibana K 1994 *Jpn. J. Appl. Phys.* **33** L804 URL https://doi.org/10.1143/JJAP.33.L804

[8] Thomas H, Morfill G E, Demmel V, Goree J, Feuerbacher B and Möhlmann D 1994 *Phys. Rev. Lett.* **73** 652–655 URL https://link.aps.org/doi/10.1103/PhysRevLett.73.652

[9] Arp O, Block D, Piel A and Melzer A 2004 *Phys. Rev. Lett.* **93** 165004 URL http://link.aps.org/doi/10.1103/PhysRevLett.93.165004

[10] Arp O, Block D, Klindworth M and Piel A 2005 *Phys. Plasmas* **12** 122102 URL https://doi.org/10.1063/1.2147000

[11] Antonova T, Annaratone B M, Goldbeck D D, Yaroshenko V, Thomas H M and Morfill G E 2006 *Phys. Rev. Lett.* **96** 115001 URL https://link.aps.org/doi/10.1103/PhysRevLett.96.115001

[12] Morfill G E, Thomas H M, Konopka U, Rothermel H, Zuzic M, Ivlev A and Goree J 1999 *Phys. Rev. Lett.* **83** 1598–1601 URL http://link.aps.org/doi/10.1103/PhysRevLett.83.1598

[13] Himpel M, Killer C, Buttenschön B and Melzer A 2012 *Phys. Plasmas* **19** 123704 URL https://doi.org/10.1063/1.4771687

[14] Kretschmer M, Khrapak S A, Zhdanov S K, Thomas H M, Morfill G E, Fortov V E, Lipaev A M, Molotkov V I, Ivanov A I and Turin M V 2005 *Phys. Rev. E* **71** 056401 URL https://doi.org/10.1103/PhysRevE.71.056401

[15] Williams J D and Thomas E 2006 *Phys Plasmas* **13** 063509 URL https://doi.org/10.1063/1.2214640

[16] Williams J D and Thomas E 2007 *Phys Plasmas* **14** 063702 URL https://doi.org/10.1063/1.2741457

[17] Schmidt C and Piel A 2015 *Phys. Rev. E* **92** 043106 URL https://link.aps.org/doi/10.1103/PhysRevE.92.043106

[18] Schmidt C and Piel A 2016 *Phys Plasmas* **23** 083704 URL https://doi.org/10.1063/1.4960320

[19] Asnaz O H, Jung H, Greiner F and Piel A 2017 *Phys. Plasmas* **24** 083701 URL https://doi.org/10.1063/1.4986855

[20] Merline D J, Vukusic S and Abdala A A 2013 *Polymer Journal* **45** 413–419 ISSN 1349-0540 URL https://doi.org/10.1038/pj.2012.162

[21] Killer C, Greiner F, Groth S, Tadsen B and Melzer A 2016 *Plasma Sources Sci. Technol.* **25** 055004 URL http://stacks.iop.org/0963-0252/25/i=5/a=055004

[22] Jasperse J R, Kahan A, Plendl J N and Mitra S S 1966 *Phys. Rev.* **146** 526–542 URL https://link.aps.org/doi/10.1103/PhysRev.146.526

[23] Weiss S, Urdl K, Mayer H A, Zikulnig-Rusch E M and Kandelbauer A 2019 *J. Appl. Polym. Sci.* **136** 47691 URL https://onlinelibrary.wiley.com/doi/abs/10.1002/app.47691

[24] Weiss S, Seidl R, Kessler W, Kessler R W, Zikulnig-Rusch E M and Kandelbauer A 2020 *Polymers* **12** ISSN 2073-4360 URL https://www.mdpi.com/2073-4360/12/11/2569

[25] Swinkels G H P M, Kersten H, Deutsch H and Kroesen G M W 2000 *J. Appl. Phys.* **88** 1747–1755 URL https://doi.org/10.1063/1.1302993

[26] Killer C, Mulsow M and Melzer A 2015 *Plasma Sources Sci. Technol.* **24** 025029 URL https://doi.org/10.1088/0963-0252/24/2/025029

[27] GmbH M retrieved 2021-06-02 Product information page https://www.microparticles-shop.de/Fluorescent-Particles/Melamine-resin-fluorescent-particles/Melamine-resin-particles-Orange-fluorescent-MF-FluoOrange-Ex-Em-560-nm-584-nm:::7_42_19.html

[28] Coates J 2006 *Interpretation of Infrared Spectra, A Practical Approach* (American Cancer Society) ISBN 9780470027318 URL https://onlinelibrary.wiley.com/doi/abs/10.1002/9780470027318.a5606

[29] Collaud Coen M, Lehmann R, Groening P and Schlapbach L 2003 *Appl. Surf. Sci.* **207** 276–286 ISSN 0169-4332 URL https://www.sciencedirect.com/science/article/pii/S0169433202015039

[30] Pavlu J, Velyhan A, Richterova I, Nemecek Z, Safrankova J, Cermak I and Zilavy P 2004 *IEEE Trans. Plasma Sci.* **32** 704–708 ISSN 1939-9375 URL https://ieeexplore.ieee.org/document/1308537

[31] Carstensen J, Jung H, Greiner F and Piel A 2011 *Phys. Plasmas* **18** 033701 URL https://doi.org/10.1063/1.3556677

[32] Kohlmann N, Wieben F, Asnaz O H, Block D and Greiner F 2019 *Phys. Plasmas* **26** 053701 URL https://doi.org/10.1063/1.5091097

6.4 A3 - Finite dust clusters under strong magnetic fields

André Melzer, Harald Krüger, Stefan Schütt, and Matthias Mulsow

Physics of Plasmas **26**, 093702 (2019)

Physics of Plasmas ARTICLE scitation.org/journal/php

Finite dust clusters under strong magnetic fields

Cite as: Phys. Plasmas **26**, 093702 (2019); doi: 10.1063/1.5116523
Submitted: 25 June 2019 · Accepted: 4 August 2019 ·
Published Online: 9 September 2019

A. Melzer,[1,a)] H. Krüger,[1] S. Schütt,[1] and M. Mulsow[2]

AFFILIATIONS

[1]Institute of Physics, University Greifswald, Felix-Hausdorff-Str. 6, 17489 Greifswald, Germany
[2]Max Planck Institute for Plasma Physics, Wendelsteinstr. 1, 17489 Greifswald, Germany

[a)]melzer@physik.uni-greifswald.de

ABSTRACT

Experiments on dust clusters trapped in the sheath of a radio frequency discharge have been performed for different magnetic field strengths ranging from a few milliteslas to 5.8 T. The dynamics of the dust clusters are analyzed in terms of their normal modes. From that, various dust properties such as the kinetic temperature, the dust charge, and the screening length are derived. It is found that the kinetic temperature of the cluster rises with the magnetic field, whereas the dust charge nearly remains constant. The screening length increases slightly at intermediate magnetic field strengths. Generally, the dust properties seem to correlate with magnetization parameters of the plasma electrons and ions, however only to a small degree.

I. INTRODUCTION

The effects of magnetic fields on dusty plasmas have attracted huge interest recently due to the availability of superconductive magnets for such experiments.[1] Dusty plasmas consist of charged dust particles immersed in a discharge plasma with electrons, ions, and neutrals. The dust acquires its charge from the steady inflow of electrons and ions onto the particle surface. The main advantage of dusty plasmas is that the dust component is easily visualized, and its dynamics can be followed at the kinetic level of individual particles.[2,3]

The very different charge-to-mass ratios of the dusty plasma components lead to different plasma regimes when magnetic fields are applied. At low magnetic fields of the order of a few milliteslas, the light electrons will be magnetized. Ions become magnetized at field strengths of the order of hundreds of milliteslas. The ultimate goal would be to visualize magnetization effects of the dust component. However, with available magnetic fields of up to about 5 T, probably only small (submicrometers) dust particles can be magnetized (together with the electrons and ions).[4] Nevertheless, it is already intriguing to study the dynamics of larger (micrometer-sized) dust particles at strong magnetic fields since their dynamics will be influenced by the behavior of the magnetized electrons and ions.

The magnetization of a plasma component (electron, ion, or dust) can be described by different parameters.[4] First, the Hall parameter

$$h_\alpha = \frac{\omega_{c\alpha}}{\nu_{\alpha n}} \tag{1}$$

relates the cyclotron frequency

$$\omega_{c\alpha} = \frac{Q_\alpha B}{m_\alpha} \tag{2}$$

of the species $\alpha = \mathrm{e}, \mathrm{i}, \mathrm{d}$ to its collision frequency $\nu_{\alpha n}$ with the neutral gas background of the plasma. When h_α becomes of the order of 1, the charged particle, on average, performs a full gyro-orbit before being perturbed by a collision.

A second parameter is the magnetization

$$M_\alpha = \frac{\omega_{c\alpha}}{\omega_{p\alpha}}, \tag{3}$$

which compares the gyrofrequency with the plasma frequency $\omega_{p\alpha}$ of the species. This parameter is particularly suited for the characterization of the collective modes in magnetized plasmas.[5]

At low magnetic fields B, even though the ions are not magnetized, i.e., $h_\mathrm{i} \ll 1$, it has been observed that the Hall component of the ion motion leads to a slow rotation of the dust cloud.[6–12] In situations where the magnetic field is applied horizontally, perpendicular to the sheath electric field, a complex sideway motion of the dust is seen.[13–16]

Under stronger fields, when the ion dynamics is influenced by magnetic fields ($h_\mathrm{i} \geq 1$), the wakefield formation will be affected. The wakefield is formed by ions streaming past a dust particle. The ions are scattered into a region downstream of the dust where they form a positive space charge region.[17–19] The ion gyromotion then interferes with the scattering process. Experiments[20,21] and simulations of the wakefield[22–26] under magnetic field demonstrate a weakening of the

Physics of Plasmas ARTICLE scitation.org/journal/php

wakefield effect. Further, filamentary structures are formed in plasma discharges.[21,27–29] Also, patterns of the electrode are found to be mapped onto the dust cloud due to the directionality imposed by the magnetic field.[30,31]

It is now very interesting to study the charging and interaction properties of the dust component when the dynamics of the plasma species (electrons and ions) are governed by magnetic field effects. Although some experiments on dusty plasmas under magnetic fields have already been performed, an analysis of the dynamical properties of a dust system over a wide range of magnetic field strengths has not been done so far.

Hence, here we like to study the behavior of a finite ensemble of (micrometer-sized) dust particles trapped in the sheath of a radio frequency (rf) discharge under an axial magnetic field up to nearly 6 T. The dynamics of the dust particles will be analyzed in terms of the clusters' normal modes. From the normal mode dynamics, the governing parameters such as the dust charge and the screening length are determined. The dust component itself has a too low charge-to-mass ratio to be magnetized. However, the dust will react to the magnetization of the electrons at lower fields and ions at higher fields. The influence of these magnetized plasma species on the dust dynamics will be investigated.

II. EXPERIMENTAL SETUP

The experiments have been performed in an asymmetric radio frequency (rf) discharge, see Fig. 1. The discharge vessel has an outer diameter of 12 cm (14 cm including the side windows and their frames). The height of the vessel is also 12 cm. The lower electrode has a diameter of 80 mm. The distance to the top plate of the chamber is about 70 mm. The top plate and the side walls of the chamber are grounded. The chamber fits into the 14 cm bore of a superconductive magnet that provides an axial magnetic field with up to 5.8 T. The magnet has a single coil, and the chamber is placed in the region of the highest magnetic field within the bore. The magnetic field changes by about 5% over the height of the chamber.

The discharge was operated at a frequency of 13.56 MHz in argon, the gas pressure was set to 6 Pa, and the discharge power was 5 W. Melamine formaldehyde (MF) particles of diameter 9.55 μm have been dropped into the discharge. The beam of an illumination laser (wavelength 532 nm) is expanded into a light sheet and guided through a top window into the chamber. The light is deflected into the horizontal plane by a mirror inside the chamber and illuminates the particles. The scattered light from the dust is recorded through another top window using a CMOS camera at a frame rate of about 200 frames per second.

For the experiments described here, about 30 MF particles have been dropped into the discharge. Vertically, they are trapped in the plasma sheath by an upward electric field force that balances the weight of the particles. Horizontally, the particles are confined by a shallow parabolic depression in the electrode, which, due to bending of the equipotential lines, provides a radially inward confining force. The particles then arrange in a highly ordered two-dimensional finite dust cluster, see Fig. 1(b) and Refs. 32–35. By vertically scanning the laser illumination, we have confirmed that the particles arrange in a single layer at low magnetic fields (at higher fields, a particle of the upper layer jumps into a second, lower layer, see below). The cluster dynamics has been recorded at varying magnetic field strengths between 0 and 5.8 T. For each magnetic field setting, 1000 frames have been recorded.

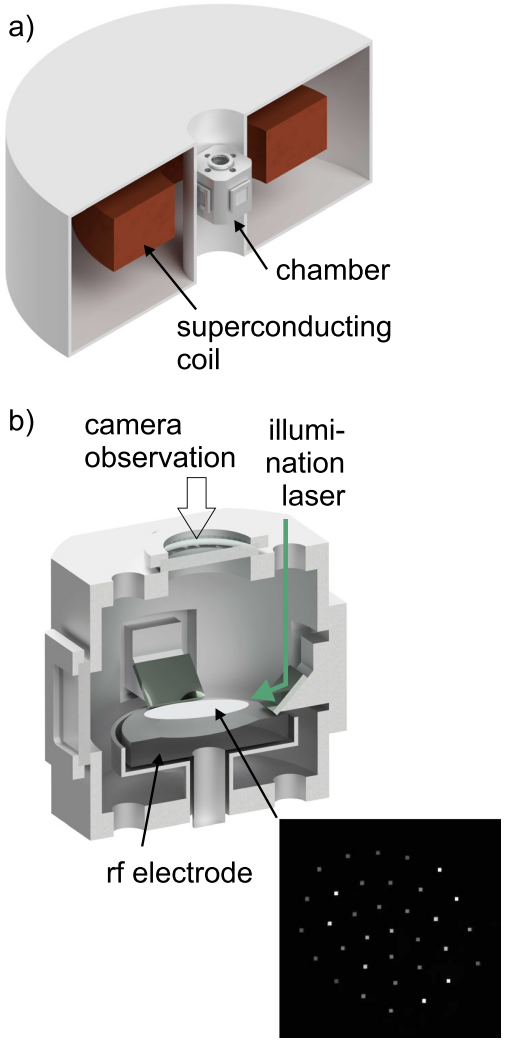

FIG. 1. Scheme of the experimental setup. (a) Overview of the superconductive magnet and discharge chamber; (b) details of the chamber and observation and illumination geometry. The inset shows, as an example, a snapshot of the dust cluster with 34 particles at a field strength of 94 mT.

III. ANALYSIS

The thermal Brownian motion of the $N \approx 34$ particles in the dust cluster around their equilibrium positions is analyzed to retrieve interaction parameters like the dust charge, screening length, or dust kinetic temperature.

First, from the video sequence, the positions $\vec{r}_i(t)$ and corresponding velocities $\vec{v}_i(t)$ of all particles i have been determined.[36–38] From that, the interaction parameters have been derived via a normal mode analysis.

The normal mode analysis starts from the total energy of a dust cluster given as[39,40]

Physics of Plasmas ARTICLE scitation.org/journal/php

$$E = \frac{1}{2} m\omega_0^2 \sum_{i=1}^{N} r_i^2 + \frac{Q^2}{4\pi\epsilon_0} \sum_{i>j} \frac{1}{r_{ij}} e^{-r_{ij}/\lambda_D}. \quad (4)$$

Here, it is assumed that the particles interact via a screened mutual Coulomb interaction and that the particles are confined by two-dimensional harmonic confinement of confinement frequency ω_0^2. The particle positions relative to the cluster center are denoted by $r_i = |\vec{r}_i|$ and the relative particle positions by $r_{ij} = |\vec{r}_i - \vec{r}_j|$. Further, N is the particle number, Q is the particle charge, m is the particle mass, ϵ_0 is the vacuum permittivity, and λ_D is the Debye shielding length.

In normalized units of radius[39,40]

$$r_0 = \left[\frac{Q^2}{4\pi\epsilon_0} \frac{2}{m\omega_0^2} \right]^{1/3} \quad (5)$$

and energy

$$E_0 = \frac{1}{2} m\omega_0^2 r_0^2, \quad (6)$$

the total energy can be written as

$$\hat{E} = \sum_{i=1}^{N} \hat{r}_i^2 + \sum_{i>j} \frac{1}{\hat{r}_{ij}} e^{-\hat{r}_{ij}\kappa}, \quad (7)$$

where $\kappa = r_0/\lambda_D$ is the screening strength and $\hat{E} = E/E_0$ and $\hat{r} = r/r_0$ are the normalized values of energy and position. It is seen that the full behavior of the cluster dynamics only depends on particle number N and κ. However, from the absolute values of r_0 and ω_0, i.e., the absolute cluster size scale and the cluster mode frequencies, the particle charge Q and the screening length λ_D can be extracted as shown below.

The dynamics of a finite cluster is then described in terms of its normal modes.[40,41] These modes ℓ are determined from the dynamical matrix (which contains the second derivative of the total energy with respect to all particles and coordinates) in terms of the eigenvector $\vec{e}_\ell$ and eigenvalue λ_ℓ of the dynamical matrix. The eigenvector characterizes the mode oscillation pattern and the eigenvalue its oscillation frequency $\omega_\ell^2 = \lambda_\ell \omega_0^2/2$. There are $2N$ eigenmodes for a 2D system of N particles.

Now, the experimentally obtained Brownian motion of the particles is decomposed into its respective contribution to each eigenmode as[34]

$$v_\ell(t) = \sum_{i=1}^{N} \vec{v}_i(t) \cdot \vec{e}_{\ell,i}, \quad (8)$$

where $\vec{e}_{\ell,i}$ is the eigenvector for particle i in mode number ℓ. From this time series of the mode velocities $v_\ell(t)$, the spectrum can be derived in the form of the spectral power density as

$$S_\ell(\omega) = \frac{2}{T} \left| \int_{-T/2}^{T/2} v_\ell(t) e^{i\omega t} dt \right|^2. \quad (9)$$

Since $\int_0^\infty S_\ell(\omega) d\omega = \langle v_\ell^2 \rangle$, we can assign an energy E_ℓ (or temperature T_ℓ) to each mode via

$$E_\ell = \frac{1}{2} m \langle v_\ell^2 \rangle = \frac{1}{2} m \int_0^\infty S_\ell(\omega) d\omega = \frac{1}{2} k_B T_\ell \quad (10)$$

(with k_B being Boltzmann's constant). This spectral power density is determined from the trajectory data and contains the full dynamic information from the measured clusters.

This experimentally obtained mode spectrum is compared with the theoretical mode spectrum, i.e., the eigenvalues of the dynamical matrix. As already mentioned (for a known particle number N), the theoretical spectrum only depends on κ. To disentangle the unknown quantities, particle charge Q, screening length λ_D, and the confinement frequency ω_0 from the experimental data, two approaches have been followed, here.

The first method starts from the two sloshing modes where the entire cluster oscillates in the confining potential well (in two perpendicular directions). These modes do not involve any relative particle motion, and so they are independent of Q and λ_D. Specifically, these sloshing oscillations occur just at the confinement frequency ω_0. Hence, these two modes yield ω_0. From the (λ_D-dependent) minimum of $\hat{E}$ of Eq. (7), i.e., the force equilibrium, and from the (Q and λ_D-dependent) frequency scaling of all normal modes, the charge Q and the screening length λ_D are found.

The sloshing mode oscillation frequency could not always be extracted with sufficient accuracy from the experimental data. So, for comparison, we used a second method where we have prescribed a value of κ. Then, the value of ω_0 is determined by fitting the theoretical mode frequencies (which scale proportionally to ω_0) to the observed ones. Again, using the minimum of $\hat{E}$ of Eq. (7), the scaling r_0 is obtained. In this way, the charge Q and the screening length $\lambda_D = r_0/\kappa$ are determined.

It should be noted that only these three values, Q, ω_0, and λ_D, determine the behavior of all $2N \approx 70$ modes. Hence, a comparison of the measured mode spectrum with all $2N$ theoretical modes allows us to reliably identify these parameters.

IV. RESULTS

The experiments described here have been performed using a cluster of $N = 34$ particles trapped in the sheath of the rf discharge. The magnetic field has then been ramped up from zero field to 5.8 T. For each field setting, the particle motion has been recorded.

For the conditions of our experiment, we estimated the magnetic field strengths at which the magnetization parameters given in Eqs. (1) and (3) equal unity. The corresponding magnetic field values are compiled in Table I and are marked by arrows in Figs. 3, 5, and 6.

A. Trajectories and energies

To start the description of the experimental results, the particle trajectories are shown in Fig. 2 for several magnetic field settings. First, the size of the cluster is not strongly affected by the magnetic field.

TABLE I. Relevant magnetic field strength B in milliteslas for magnetization parameters at our experimental conditions with the estimated plasma density of $n_{e,i} = 3 \times 10^{14}$ m^{-3}, electron temperature of $T_e = 3$ eV, and ion temperature of $T_i = 0.03$ eV.

	Electrons		Ions	
	$h_e = 1$	$M_e = 1$	$h_i = 1$	$M_i = 1$
B (mT)	0.4	6	130	1500

Physics of Plasmas ARTICLE scitation.org/journal/php

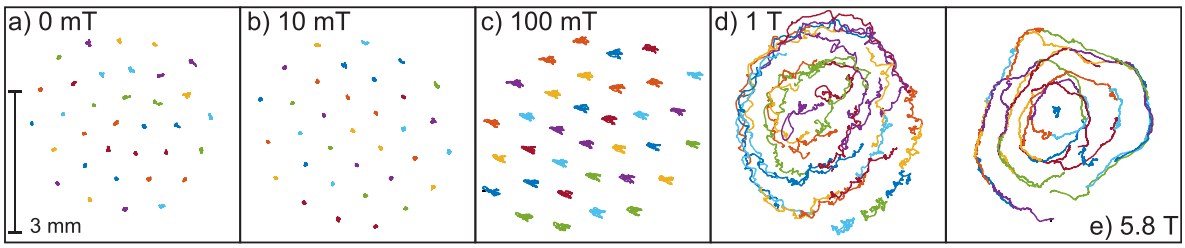

FIG. 2. Trajectories of the dust cluster at various field strengths over a time span of about 5 s.

Further, it is seen that at low magnetic field strengths, the particles form a highly ordered dust cluster with only small (Brownian) excursions around the equilibrium positions. At elevated fields, in the range between $B \approx 100$ mT and $B \approx 150$ mT, one sees a common excursion of all particles on a slightly larger scale with a preferential direction. Judging from the video images, one could speculate that the motion seems to be driven by a plasma instability. The cluster structure is nevertheless still preserved.

At larger fields, a rotary motion of the cluster is seen. It is mainly a rotation of the entire cluster; only a few particle exchanges are seen where particles hop between different shells of the cluster. This behavior is found up to the highest field strengths of $B = 5.8$ T. To quantify the rotary motion, the energy stored in this mode is shown in Fig. 3, using Eq. (10) for the rotation mode. Up to a field strength of about 50 mT, the energy E_{rot} of the rotary mode is small, equivalent to a temperature of about $T_{rot} = 1000$ K. After that, one finds a gradual increase in rotation energy up to $T_{rot} = 4000$ K at 170 mT. This is followed by a sudden increase to $T_{rot} = 670 \times 10^3$ K at 2 T and then a final drop to somewhat smaller values at further increased fields. The noticeable change in rotation energy for fields larger than 170 mT is accompanied by a slight change in the cluster structure, see below.

For comparison, the mean mode temperature of all modes is also shown in Fig. 3. The mean mode energy generally shows the same trend with nearly constant temperatures up to 50 mT and further

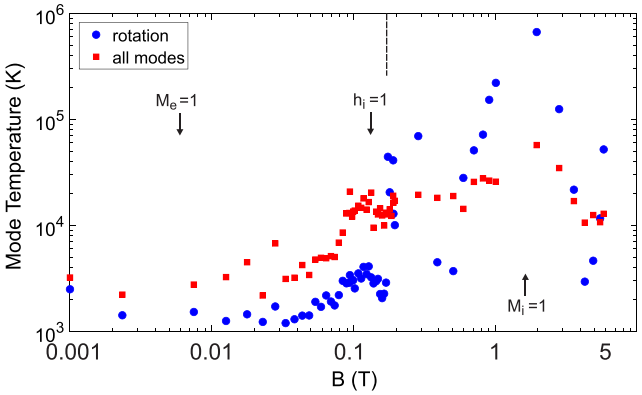

FIG. 3. Energy of the rotation mode as a function of magnetic field strength (circles). The energy is given in temperature units. For comparison, the mean energy of all modes as a function of magnetic field strength is also shown. To allow for a logarithmic field strength axis, here and in the following figures, the data point at $B = 0$ is shown arbitrarily at 10^{-3} T. The dashed vertical line indicates where the structural change occurs.

increasing temperatures up to 170 mT. The subsequent temperature increase above 170 mT is not as strong as for the rotation. It should be noted that even at very low fields (below 50 mT), the cluster temperature is decisively above room temperature which we attribute to the influence of stochastic heating processes, e.g., from charge fluctuations which become noticeable at low gas pressures.[42,43] The energy increase between 50 mT and 170 mT is not due to changes of the cluster structure, but probably due to increased plasma fluctuations.

Further, it is interesting to see that the energy of the rotation mode is decisively below the mean mode temperature up to a field strength of 170 mT. This correlates well with the trajectories that do not show any sign of rotary motion. Only after the change in the cluster structure, the rotary mode is predominantly excited with energies that are far above those of the other modes. In our other experiments with other particle sizes or particle number in the cluster, we always find no rotation at low magnetic fields. Rotation only sets in at fields decisively larger than 100 mT. Hence, in our experiment, cluster rotation seems to be hindered. However, there is no electrode structure that deliberately pins the particle motion, e.g., as in Refs. 30 and 31.

The absence of rotation is insofar unusual as in many other experiments, a clear rotation of the dust ensemble is observed, even at very low magnetic fields, see e.g., Refs. 6, 7, 10, 35, and 44–46. For example, for small dust clusters, in rf discharges, angular velocities of the order of $\Omega \approx 0.2$ s^{-1} have been reported for magnetic field strengths as low as 5 mT, see, e.g., Refs. 10 and 35. For dust clusters in dc discharges, $\Omega \approx 0.1$ s^{-1} at $B = 20$ mT has been observed.[46] Here, in our experiment, noteworthy rotation velocities are found only for $B > 180$ mT. For example, $\Omega = 0.28$ s^{-1} at $B = 1$ T, see Fig. 2(d).

As already mentioned above, during the step-by-step increase in the magnetic field strength, a change in the cluster structure has occurred in our experimental sequence at a field strength of 170 mT. Up to that field, the cluster consisted of $N = 34$ particles arranged in a single layer. Then, one of the particles switched to a layer below the layer of the other particles. Hence, only $N = 33$ particles are in the actual cluster layer (which is further analyzed here and in the following). The lower-layer particle, due to wakefield attraction, became aligned below one of the other cluster particles.[17,18,47–61] At this vertically aligned position, the lower-layer particle performs small-amplitude self-excited oscillations.[62,63] These lower layer oscillations due to Coulomb interaction also excite oscillations in the upper layer. However, in contrast to previous experiments without the magnetic field,[64,65] these oscillations were not very violent which might be an effect of the reduced wakefield strength due to magnetic field effects.[20,21,66,67] Hence, these lower layer oscillations only weakly affect the normal mode spectrum as shown below.

Physics of Plasmas ARTICLE scitation.org/journal/php

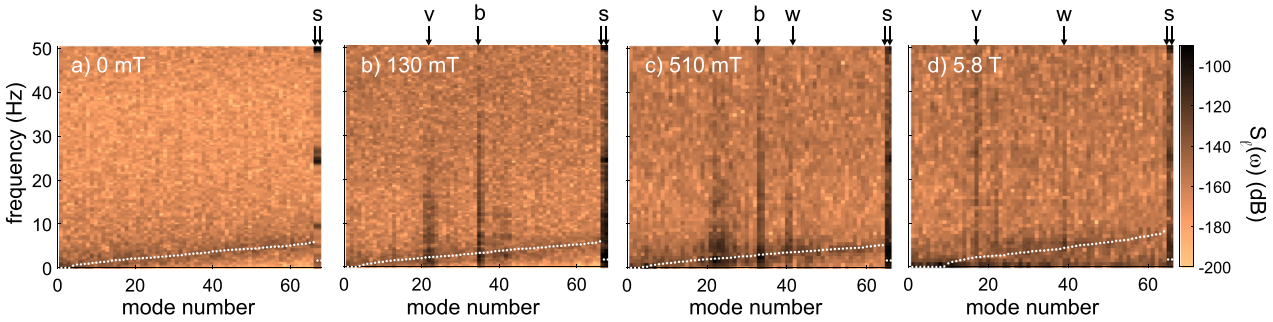

FIG. 4. Normal mode spectrum of the cluster for different magnetic field strengths. The spectral power density $S_\ell\omega$ is shown color-coded for the $2N$ eigenmodes of the system. The vertical axis denotes the frequency. The white circles indicate the theoretical mode spectrum fitted to the measured spectral power density. The last two modes of each spectrum are the two sloshing modes, indicated by s. Further, the breathing mode is denoted by b, vortex-antivortex oscillation by v, and localized wakefield modes by w; see the text for details.

Nevertheless, this structural change seems to trigger the rotary motion of the cluster and the second jump in mode energy.

B. Normal modes

We now look at the normal modes of the cluster, which have been derived according to the procedure described in Sec. III. Figure 4 shows the measured spectral power density $S_\ell(\omega)$ for the $2N$ eigenmodes of the cluster. Starting with the power spectrum at no magnetic field [Fig. 4(a)], it is seen that the highest power density is found in a narrow frequency band, which increases from small frequencies to about 8 Hz at the highest mode numbers. The final two modes in the spectrum indicate the sloshing modes. From that, the confinement strength ω_0 is derived. Then, the particle charge Q and the screening length λ_D are varied to fit the theoretical mode frequencies to the measured spectrum. It is reminded here that only these values, charge Q and screening strength λ_D, are used to fit the frequencies for "all" the modes. The fitted mode frequencies are shown by the circles. It is seen that the theoretical mode frequencies closely follow the measured spectrum. Hence, the charge and screening length can be extracted with confidence. Further, as one would expect from the equipartition theorem, the energy stored in each of the modes is very similar.

When looking at the mode spectra of the cluster at various magnetic field strengths, one always finds these frequency bands that increase in frequency with the mode number. Also, the theoretical mode frequencies follow the frequency bands quite nicely. However, additional features appear in the spectrum.

The sloshing modes (denoted by "s" in Fig. 4) increase in energy up to a field strength of about 130 mT and remain strong up to fields of 2.5 T. After that, the energy of the sloshing modes is decisively reduced.

In the spectra at $B = 130$ mT [Fig. 4(b)] and $B = 510$ mT [Fig. 4(c)], a few modes around the mode number of 20 as well as a mode around the mode number of 35 are preferably excited which can be seen from the high spectral power density of these modes. Also, at 510 mT (and much weaker at 130 mT), a mode around the mode number of 40 is excited. The modes around mode numbers of 20 and 40 are also excited at the highest field of 5.8 T.

The mode around the mode number of 35 is the breathing mode ("b" in Fig. 4) where all particles oscillate radially inward and outward. The breathing mode becomes a dominant feature in the spectrum starting at about 30 mT up to about 2.5 T. For higher fields, the breathing mode loses its dominance again.

The modes around the mode number of 20 describe vortex-antivortex motion ("v" in Fig. 4). There, a fraction of the cluster rotates clockwise and the other fraction of the cluster anticlockwise. This type of motion becomes prominent in the field range between 50 mT and 2.5 T.

The mode around the mode number of 40 is a localized mode that is associated with the wakefield instability and the structural change ("w" in Fig. 4). This mode reflects the oscillations of the lower layer particle that couples to the upper layer. The mode becomes clearly observable above the structural change ($B \approx 170$ mT) and is found up to the highest field.

In summary, certain modes (sloshing, vortex-antivortex, and breathing) are preferably excited in this experiment. The sloshing and breathing modes are susceptible to global plasma fluctuations; also see the trajectories in Fig. 2(c). This is due to the fact that plasma fluctuations might shift the center and the strength of the confinement for the dust cluster. A shift of the central position would excite sloshing modes, and a change in confinement strength would excite breathing modes.

Since, in our experiment, the rotation of the entire cluster is hindered up to field strengths of about 170 mT, the next least stable mode is often the vortex-antivortex formation.[34,40] So, instead of global rotation, the vortex-antivortex formation is excited.

The influence of these modes decreases at field strengths above 2.5 T in our experiment. At these field strengths, the plasma becomes filamented[21,27–29] where localized regions of higher and lower electron density (and plasma emission) are found. In accompanying experiments under similar conditions where we have focused at the plasma glow (and the interaction with particles), we have seen the appearance of filaments. The typical size of filaments in our discharge is about 2–3 mm which just corresponds to the cluster size. Judging from the plasma-glow experiments, we assume that in the experiments presented here, the cluster indeed is trapped in the high-density part of a filament at the highest magnetic field strengths. Also from the mode behavior, the dust clusters in this experiment become confined in the higher-density filament suppressing the above-mentioned modes above 2.5 T. A possible influence of the presence of filaments might

Physics of Plasmas ARTICLE scitation.org/journal/php

also be seen from the particle trajectories in Fig. 2(e) at 5.8 T where the cluster is not exactly circular any more.

C. Dust cluster properties

Finally, the dust properties have been extracted from the normal modes of the dust cluster. Figures 5 and 6 show the derived dust charge and screening length as a function of magnetic field strength. As described above, two different methods have been employed. For the first method, ω_0 has been determined from the sloshing modes and then the charge $Q = Z_d e$ and λ_D have been derived from the fit of the theoretical mode frequencies to the measured data. For the second method, a value of κ has been prescribed ($\kappa = 1$ in this case) and then $Q = Z_d e$ and ω_0 are found from the fit to the data. It should be noted that, in this second method, also a slightly varying screening length $\lambda_D = r_0/\kappa$ is derived due to a slightly varying r_0, which in turn is determined from the minimum energy condition.

When looking at the dust charge in Fig. 5, it is seen that both methods arrive at very similar dust charges. Moreover, surprisingly, the dust charge shows only modest variation with magnetic field strength. The dust charge is found in the range between 9000 and 12 000 elementary charges with a mean of 10 500 elementary charges. This charge value is typical for dust particles of this size, see, e.g., Refs. 34, 68, and 69. The data from the first method (using ω_0 from the sloshing modes) show a slight dip of dust charges around 100 mT. From the other method, this is not seen as clearly.

Here, the dust charges from the method with a prescribed $\kappa = 1$ are shown. When using a different prescribed κ, the charges show very similar overall behavior as for $\kappa = 1$. Only the absolute values of the dust charges are somewhat larger by about 20% when using $\kappa = 3$ and larger by about 10% when using $\kappa = 2$. For $\kappa = 0$, the retrieved charges are 5% smaller than for $\kappa = 1$.

Generally, both methods (the one using the sloshing modes to derive ω_0 and the one with a prescribed κ) agree well with each other (within about 5%–10%). From that, we estimate that the dust charges are also accurate within this error range. The relative error between the charge values determined within each method might then be at the lower limit of the error range. However, for magnetic field strength above 0.5 T, the scatter in the data is somewhat larger compared to lower field strengths. This might result from the fact that the normal mode spectrum is not as defined as for the lower field strengths.

That the dust charge is nearly constant with the magnetic field has already previously been observed by Carstensen *et al.*[20] but has here been extended toward even higher field strengths. In simulations under realistic experimental conditions, the dust charge has been calculated for particles trapped in the sheath of a plasma discharge including ion-neutral collisions. There, the dust charge is found to decrease by about 5% when the magnetic field is varied from 0 T to 10 T.[25,26] In other recent numerical studies of particles in a collisionless plasma with flowing ions under strong magnetic fields,[70] a slightly larger variation of dust charge with the magnetic field (and flow velocity) of the order of 25% was found. There, the smallest dust charges are expected near $M_i \approx 1$. Our experiments generally agree with these simulations in that the dust charge variation is small, less than 20% compared to the case of no field. However, in our experiments, there seems to be a trend to slightly larger charges with the increasing magnetic field and a minimum of dust charges near $M_i \approx 1$ cannot be identified.

Finally, the screening length derived from the normal modes is shown in Fig. 6, again for the two methods described above. In both cases, the retrieved screening length is somewhat larger for medium field strengths compared to small and large fields. When prescribing $\kappa = 1$, the retrieved screening length varies between 800 and 1000 μm due to the variation of r_0 determined from the minimum energy condition. For the method relying on the determination of ω_0 from the sloshing modes, the variation of the screening length is larger (700–3000 μm). However, for both methods, the screening length is decisively larger than the interparticle distance of about 500 μm. Hence, the screening of the dust charges is only moderate. The somewhat stronger screening seen using the method with a prescribed κ can easily be made up by a slightly increased dust charge. This is seen from the fact that, as mentioned above, using a prescribed screening strength $\kappa = 0$ (i.e., infinite screening length) leads only to 5% smaller retrieved charges. For comparison, using the estimated values of plasma density and temperature given in the caption of Table I, the

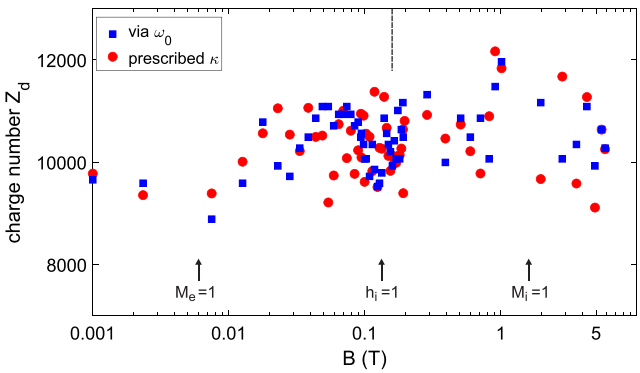

FIG. 5. Charge number retrieved from the normal mode as a function of magnetic field strength. The charges are obtained either from determining ω_0 from the sloshing modes or from prescribing a value of κ (see the text for details). The dashed vertical line indicates where the structural change occurs.

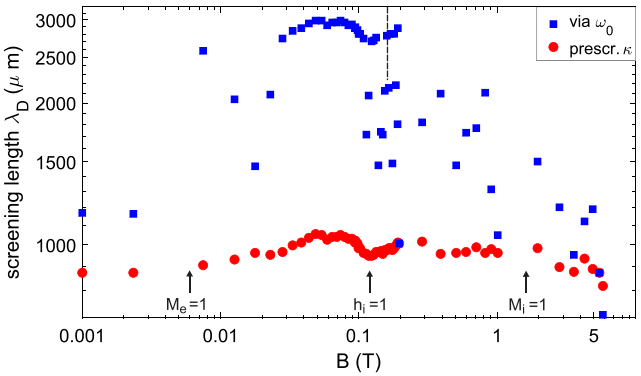

FIG. 6. Screening length retrieved from the normal mode as a function of magnetic field strength. The screening lengths are obtained either from determining ω_0 from the sloshing modes or from prescribing a value of κ (see the text for details). The dashed vertical line indicates where the structural change occurs.

Physics of Plasmas ARTICLE scitation.org/journal/php

electron Debye length is about $\lambda_{De} = 750\,\mu$m, which corresponds well to the values obtained from the method with the prescribed κ.

As a final point, we look at the characteristic magnetic fields where the Hall parameters h_e and h_i as well as the ion magnetization M_i reach unity, compare Table I. Another field strength of interest might be where the electron gyroradius equals the dust particle size. This is found at about 900 mT. This magnetic field strength is not too far off from the situation where $M_i = 1$, and so the observed features near $M_i = 1$ might also be due to the small electron gyroradius.

In nearly all cases, these characteristic magnetic field values coincide with features in the behavior of the different quantities. In Fig. 3, the mode temperatures increase until $h_i = 1$, and then, the temperatures start to decrease again. The next increase in temperature above 170 mT is due to the structural change. But, then, the maximum of these mode temperatures is again found at field strengths where $M_i = 1$. Similarly, the dust particle charges in Fig. 5 show a slight decrease until $M_e = 1$ followed by a modest increase for higher fields. The dip in the dust charges seen for the method of determining ω_0 from the sloshing mode just coincides with h_i being unity. In the same way, the screening length in Fig. 6 starts to increase beyond $M_e = 1$ and declines around $M_i = 1$. Further, a slight dip in the retrieved screening lengths is seen near $h_i = 1$.

The change in the measured quantities is not very large, and the coincidence with the characteristic magnetization parameters might be accidental. Nevertheless, this coincidence is intriguing. However, an explanation in terms of the microscopic physical processes is very difficult since the dust particles are trapped in the sheath where, in addition to the complexities of the magnetic field effects, strong electric fields and a directed supersonic ion flow prevail.

V. SUMMARY

To summarize, we have trapped a dust cluster in the sheath of an rf discharge and have analyzed the cluster dynamics using a normal mode approach. The discharge was placed into the bore of a superconductive magnet where the magnetic field strength has been ramped from 0 to 5.8 T. We were able to reconstruct the normal mode spectrum up to the highest field strengths.

With the increasing field, the kinetic temperatures of the mode generally increased. At larger field strength, this increase was supported by a structural change of the cluster where a particle dropped to a lower, second layer. There, the particle was susceptible to the wakefield instabilities, leading to additional heating. Nevertheless, these wakefield instabilities influenced the mode spectrum much less than in previous experiments (without the magnetic field).[64,65] A rotation of the cluster was observed only at relatively high fields (above 170 mT), in contrast to many previous findings.[6,7,10,44–46]

From the mode spectrum, it was seen that at the lowest field strengths, the cluster shows a thermal excitation with energy equipartition between the modes. Then, certain modes (breathing, sloshing, and vortex-antivortex modes) become preferably excited at field strengths larger than 30–50 mT. These modes remain strong up to fields of about 2.5 T. At even higher fields, again, a more homogenous energy distribution is found, which might reflect the influence of plasma filaments.

From the normal modes, the dust particle charge was extracted. The charge was found to show only little variation with magnetic field strength in general agreement with other experiments.[20] With our experiments, however, we could extend the range of magnetic field strengths for dust charge measurements. A slight decrease in dust charge with the magnetic field was expected from simulations,[25,26,70] whereas our data seem to favor a trend toward slightly larger charges.

Finally, the screening length derived from the normal mode spectrum is found somewhat larger than the interparticle distance. The derived screening lengths exhibit a certain variation with magnetic field strength but suggest a relatively weak screening effect throughout the magnetic field range.

Some features of the measured quantities seem to correlate with the magnetization parameters of the plasma species. However, the changes in the dust properties were relatively small, and so it is difficult to reliably relate the measured changes to the plasma magnetization. Finally, the role of filamentation has to be further clarified.

ACKNOWLEDGMENTS

This work was supported by the German Aerospace Center under No. DLR 50 WM 1638 and Deutsche Forschungsgemeinschaft under No. 1534 Me 8-1. The superconductive D-Mag magnet is operated in cooperation with the group of Thomas Sunn Pedersen at IPP Greifswald. We would like to thank P. Druckrey for technical support.

REFERENCES

[1]D. Block and A. Melzer, "Dusty (complex) plasmas—routes towards magnetized and polydisperse systems," J. Phys. B **52**, 063001 (2019).
[2]A. Piel, *Plasma Physics: An Introduction to Laboratory, Space, and Fusion Plasmas* (Springer, Heidelberg, 2010).
[3]P. K. Shukla and A. A. Mamun, *Introduction to Dusty Plasma Physics* (Institute of Physics Publishing, Bristol, 2002).
[4]E. Thomas, R. L. Merlino, and M. Rosenberg, "Magnetized dusty plasmas: the next frontier for complex plasma research," Plasma Phys. Controlled Fusion **54**, 124034 (2012).
[5]H. Kählert, A. Melzer, M. Puttscher, T. Ott, and M. Bonitz, "Magnetic field effects and waves in complex plasmas," Eur. Phys. J. D **72**, 83 (2018).
[6]U. Konopka, D. Samsonov, A. V. Ivlev, J. Goree, V. Steinberg, and G. Morfill, "Rigid and differential plasma crystal rotation induced by magnetic fields," Phys. Rev. E **61**, 1890 (2000).
[7]N. Sato, G. Uchida, T. Kaneko, S. Shimizu, and S. Iizuka, "Dynamics of fine particles in magnetized plasmas," Phys. Plasmas **8**, 1786–1790 (2001).
[8]P. K. Kaw, K. Nishikawa, and N. Sato, "Rotation in collisional strongly coupled dusty plasmas in a magnetic field," Phys. Plasmas **9**, 387 (2002).
[9]F. M. H. Cheung, C. Brunner, A. A. Samarian, and B. W. James, "Coulomb clusters in dusty plasmas: Rotation and stability," AIP Conf. Proc. **799**, 185 (2005).
[10]J. Carstensen, F. Greiner, L.-J. Hou, H. Maurer, and A. Piel, "Effect of neutral gas motion on the rotation of dust clusters in an axial magnetic field," Phys. Plasmas **16**, 013702 (2009).
[11]V. Y. Karasev, E. S. Dzlieva, A. I. Eikhval'd, M. A. Ermolenko, M. S. Golubev, and A. Y. Ivanov, "Single dust-particle rotation in glow-discharge plasma," Phys. Rev. E **79**, 026406 (2009).
[12]T. Reichstein, J. Wilms, F. Greiner, A. Piel, and A. Melzer, "Experiments and simulations of particle flows in a magnetized dust torus," Contrib. Plasma Phys. **52**, 813 (2012).
[13]M. Puttscher and A. Melzer, "Paramagnetic dust particles in rf-plasmas with weak external magnetic fields," New J. Phys. **16**, 043026 (2014).
[14]M. Puttscher and A. Melzer, "Dust particles under the influence of crossed electric and magnetic fields in the sheath of an rf discharge," Phys. Plasmas **21**, 123704 (2014).
[15]M. Puttscher and A. Melzer, "Vertically aligned dust particles under the influence of crossed electric and magnetic fields in the sheath of a radio frequency discharge," Phys. Plasmas **22**, 073701 (2015).

[16]A. Melzer and M. Puttscher, "Transverse forces on dust particles in a magnetized sheath with crossed electric and magnetic fields," Phys. Plasmas **24**, 053701 (2017).
[17]S. V. Vladimirov and M. Nambu, "Attraction of charged particles in plasmas with finite flows," Phys. Rev. E **52**, R2172–R2174 (1995).
[18]M. Nambu, S. V. Vladimirov, and P. K. Shukla, "Attractive forces between charged particulates in plasmas," Phys. Lett. A **203**, 40–42 (1995).
[19]M. Lampe, G. Joyce, G. Ganguli, and V. Gavrishchaka, "Interactions between dust grains in a dusty plasma," Phys. Plasmas **7**, 3851–3861 (2000).
[20]J. Carstensen, F. Greiner, and A. Piel, "Ion-wake-mediated particle interaction in a magnetized-plasma flow," Phys. Rev. Lett. **109**, 135001 (2012).
[21]H. Jung, F. Greiner, A. Piel, and W. J. Miloch, "Experiments on wake structures behind a microparticle in a magnetized plasma flow," Phys. Plasmas **25**, 073703 (2018).
[22]J.-P. Joost, P. Ludwig, H. Kählert, C. Arran, and M. Bonitz, "Screened Coulomb potential in a flowing magnetized plasma," Plasma Phys. Controlled Fusion **57**, 025004 (2015).
[23]W. J. Miloch, D. Darian, and M. Mortensen, "Wake potential of a dust particle in magnetised plasmas," Phys. Scr. **92**, 114006 (2017).
[24]W. J. Miloch, H. Jung, D. Darian, F. Greiner, M. Mortensen, and A. Piel, "Dynamic ion shadows behind finite-sized objects in collisionless magnetized plasma flows," New J. Phys. **20**, 073027 (2018).
[25]A. Piel, F. Greiner, H. Jung, and W. J. Miloch, "Molecular dynamics simulations of wake structures behind a microparticle in a magnetized ion flow. I. Collisionless limit with cold ion beam," Phys. Plasmas **25**, 083702 (2018).
[26]A. Piel, H. Jung, and F. Greiner, "Molecular dynamics simulations of wake structures behind a microparticle in a magnetized ion flow. ii. Effects of velocity spread and ion collisions," Phys. Plasmas **25**, 083703 (2018).
[27]M. Schwabe, U. Konopka, P. Bandyopadhyay, and G. E. Morfill, "Pattern formation in a complex plasma in high magnetic fields," Phys. Rev. Lett. **106**, 215004 (2011).
[28]B. Tadsen, F. Greiner, and A. Piel, "Preparation of magnetized nanodusty plasmas in a radio frequency-driven parallel-plate reactor," Phys. Plasmas **21**, 103704 (2014).
[29]E. Thomas, U. Konopka, R. L. Merlino, and M. Rosenberg, "Initial measurements of two- and three-dimensional ordering, waves, and plasma filamentation in the magnetized dusty plasma experiment," Phys. Plasmas **23**, 055701 (2016).
[30]E. Thomas, B. Lynch, U. Konopka, R. L. Merlino, and M. Rosenberg, "Observations of imposed ordered structures in a dusty plasma at high magnetic field," Phys. Plasmas **22**, 030701 (2015).
[31]E. Thomas, U. Konopka, B. Lynch, S. Adams, S. LeBlanc, R. L. Merlino, and M. Rosenberg, "Quasi-discrete particle motion in an externally imposed, ordered structure in a dusty plasma at high magnetic field," Phys. Plasmas **22**, 113708 (2015).
[32]W.-T. Juan, Z.-H. Huang, J.-W. Hsu, Y.-J. Lai, and I. Lin, "Observation of dust Coulomb clusters in a plasma trap," Phys. Rev. E **58**, R6947(R) (1998).
[33]M. Klindworth, A. Melzer, A. Piel, and V. Schweigert, "Laser-excited intershell rotation of finite Coulomb clusters in a dusty plasma," Phys. Rev. B **61**, 8404 (2000).
[34]A. Melzer, "Mode spectra of thermally excited 2d dust Coulomb clusters," Phys. Rev. E **67**, 016411 (2003).
[35]F. Cheung, A. Samarian, and B. James, "The rotation of planar-2 to planar-12 dust clusters in an axial magnetic field," New J. Phys. **5**, 75 (2003).
[36]J. C. Crocker and D. G. Grier, "When like charges attract: The effects of geometrical confinement on long-range colloidal interactions," Phys. Rev. Lett. **77**, 1897–1900 (1996).
[37]A. Melzer, M. Himpel, C. Killer, and M. Mulsow, "Stereoscopic imaging of dusty plasmas," J. Plasma Phys. **82**, 615820102 (2016).
[38]A. Melzer, *Physics of Dusty Plasmas: An Introduction*, Lecture Notes (Springer, Frankfurt/Main, 2019).
[39]V. M. Bedanov and F. Peeters, "Ordering and phase transitions of charged particles in a classical finite two-dimensional system," Phys. Rev. B **49**, 2667 (1994).
[40]V. A. Schweigert and F. Peeters, "Spectral properties of classical two-dimensional clusters," Phys. Rev. B **51**, 7700 (1995).
[41]K. Nelissen, A. Matulis, B. Partoens, M. Kong, and F. M. Peeters, "Spectrum of classical two-dimensional Coulomb clusters," Phys. Rev. E **73**, 016607 (2006).
[42]C. Schmidt and A. Piel, "Stochastic heating of a single Brownian particle by charge fluctuations in a radio-frequency produced plasma sheath," Phys. Rev. E **92**, 043106 (2015).
[43]R. Quinn and J. Goree, "Single-particle langevin model of particle temperature in dusty plasmas," Phys. Rev. E **61**, 3033 (2000).
[44]S. Nunomura, N. Ohno, and S. Takamura, "Effects of ion flow by e × b drift on dust particle behaviour in magnetized cylindrical electron cyclotron resonance plasmas," Jpn. J. Appl. Phys., Part 1 **36**, 877 (1997).
[45]S. Jaiswal, T. Hall, S. LeBlanc, R. Mukherjee, and E. Thomas, "Effect of magnetic field on the phase transition in a dusty plasma," Phys. Plasmas **24**, 113703 (2017).
[46]E. S. Dzlieva, L. G. Dyachkov, L. A. Novikov, S. I. Pavlov, and V. Y. Karasev, "Complex plasma in glow discharge in a strong magnetic field," Europhys. Lett. **123**, 15001 (2018).
[47]V. A. Schweigert and M. S. Obrekht, "Structure of the wigner crystal of the microparticles in plasma," Pis'ma Zh. Tekh. Fiz. **21**, 57 (1995) [Tech. Phys. Lett. **21**, 377 (1995)].
[48]A. Melzer, V. A. Schweigert, I. V. Schweigert, A. Homann, S. Peters, and A. Piel, "Structure and stability of the plasma crystal," Phys. Rev. E **54**, R46–R49 (1996).
[49]K. Takahashi, T. Oishi, K. Shimomai, Y. Hayashi, and S. Nishino, "Analyses of attractive forces between particles in Coulomb crystal of dusty plasmas by optical manipulations," Phys. Rev. E **58**, 7805 (1998).
[50]G. A. Hebner, M. E. Riley, and B. M. Marder, "Dynamic probe of dust wake-field interactions using constrained collisions," Phys. Rev. E **68**, 016403 (2003).
[51]A. A. Samarian, S. V. Vladimirov, and B. James, "Wake-induced symmetry-breaking of dust particle arrangements in a complex plasma," JETP Lett. **82**, 758 (2005).
[52]S. K. Zhdanov, A. V. Ivlev, and G. E. Morfill, "Mode-coupling instability of two-dimensional plasma crystals," Phys. Plasmas **16**, 083706 (2009).
[53]L. Couëdel, S. K. Zhdanov, A. V. Ivlev, V. Nosenko, H. M. Thomas, and G. E. Morfill, "Wave mode coupling due to plasma wakes in two-dimensional plasma crystals: In-depth view," Phys. Plasmas **18**, 083707 (2011).
[54]L. Couëdel, V. Nosenko, A. V. Ivlev, S. K. Zhdanov, H. M. Thomas, and G. E. Morfill, "Direct observation of mode-coupling instability in two-dimensional plasma crystals," Phys. Rev. Lett. **104**, 195001 (2010).
[55]B. Liu, J. Goree, and Y. Feng, "Mode coupling for phonons in a single-layer dusty plasma crystal," Phys. Rev. Lett. **105**, 085004 (2010).
[56]M. Kroll, J. Schablinski, D. Block, and A. Piel, "On the influence of wakefields on three-dimensional particle arrangements," Phys. Plasmas **17**, 013702 (2010).
[57]I. H. Hutchinson, "Forces on a small grain in the nonlinear plasma wake of another," Phys. Rev. Lett. **107**, 095001 (2011).
[58]I. H. Hutchinson, "Intergrain forces in low-Mach-number plasma wakes," Phys. Rev. E **85**, 066409 (2012).
[59]P. Ludwig, W. J. Miloch, H. Kählert, and M. Bonitz, "On the wake structure in streaming complex plasmas," New J. Phys. **14**, 053016 (2012).
[60]T. B. Röcker, A. V. Ivlev, R. Kompaneets, and G. E. Morfill, "Mode coupling in two-dimensional plasma crystals: Role of the wake model," Phys. Plasmas **19**, 033708 (2012).
[61]K. Qiao, J. Kong, E. V. Oeveren, L. S. Matthews, and T. W. Hyde, "Mode couplings and resonance instabilities in dust clusters," Phys. Rev. E **88**, 043103 (2013).
[62]V. A. Schweigert, I. V. Schweigert, A. Melzer, A. Homann, and A. Piel, "Alignment and instability of 'dust' crystals in plasmas," Phys. Rev. E **54**, 4155 (1996).
[63]V. A. Schweigert, I. V. Schweigert, A. Melzer, A. Homann, and A. Piel, "Plasma crystal melting: A nonequilibrium phase transition," Phys. Rev. Lett. **80**, 5345 (1998).
[64]R. Ichiki, Y. Ivanov, M. Wolter, Y. Kawai, and A. Melzer, "Melting and heating of 2d Coulomb clusters in dusty plasmas," Phys. Rev. E **70**, 066404 (2004).
[65]Y. Ivanov and A. Melzer, "Melting dynamics of finite clusters in dusty plasmas," Phys. Plasmas **12**, 072110 (2005).
[66]M. Nambu, M. Salimullah, and R. Bingham, "Effect of a magnetic field on the wake potential in a dusty plasma with streaming ions," Phys. Rev. E **63**, 056403 (2001).

Physics of Plasmas ARTICLE scitation.org/journal/php

[67]M. Salimullah, M. Torney, P. K. Shukla, and A. K. Banerjee, "Three-dimensional wakefields in a magnetized dusty plasma with streaming ions," Phys. Scr. **67**, 534 (2003).
[68]S. Nunomura, J. Goree, S. Hu, X. Wang, and A. Bhattacharjee, "Dispersion relations of longitudinal and transverse waves in two-dimensional screened Coulomb crystals," Phys. Rev. E **65**, 066402 (2002).
[69]V. Nosenko, S. K. Zhdanov, A. V. Ivlev, C. A. Knapek, and G. E. Morfill, "2d melting of plasma crystals: Equilibrium and nonequilibrium regimes," Phys. Rev. Lett. **103**, 015001 (2009).
[70]D. Darian, W. J. Miloch, M. Mortensen, Y. Miyake, and H. Usui, "Numerical simulations of a dust grain in a flowing magnetized plasma," Phys. Plasmas **26**, 043701 (2019).

Bibliography

[1] C. K. Goertz and G. Morfill. "A model for the formation of spokes in Saturn's ring". In: *Icarus* **53** 2 (1983), pp. 219–229. DOI: 10.1016/0019-1035(83)90143-4.

[2] C. K. Goertz. "Dusty plasmas in the solar system". In: *Rev. Geophys.* **27** 2 (1989), pp. 271–292. DOI: 10.1029/RG027i002p00271.

[3] P. Bliokh, V. Sinitsin, and V. Yaroshenko. *Dusty and Self-Gravitational Plasmas in Space*. Springer Netherlands, 1995. DOI: 10.1007/978-94-015-8557-6.

[4] M. Horányi and T. E. Cravens. "The structure and dynamics of Jupiter's ring". In: *Nature* **381** 6580 (1996), pp. 293–295. DOI: 10.1038/381293a0.

[5] M. Horányi. "Dust streams from Jupiter and Saturn". In: *Phys. Plasmas* **7** 10 (2000), pp. 3847–3850. DOI: 10.1063/1.1288909.

[6] M. Fulle. "Motion of Cometary Dust". In: Comets II. University of Arizona Press, 2004. Chap. Motion of Cometary Dust, pp. 565–575.

[7] G. S. Selwyn, J. Singh, and R. S. Bennett. "In situ laser diagnostic studies of plasma-generated particulate contamination". In: *Journal of Vacuum Science & Technology A: Vacuum, Surfaces, and Films* **7** 4 (1989), pp. 2758–2765. DOI: 10.1116/1.576175.

[8] G. M. Jellum and D. B. Graves. "Particulates in aluminum sputtering discharges". In: *J. Appl. Phys.* **67** 10 (1990), pp. 6490–6496. DOI: 10.1063/1.346081.

[9] G. S. Selwyn. "Optical characterization of particle traps". In: *Plasma Sources Sci. Technol.* **3** 3 (1994), pp. 340–347. DOI: 10.1088/0963-0252/3/3/016.

[10] A. Bouchoule. *Dusty Plasmas, Physics, Chemistry and Technological Impacts*. Ed. by A. Bouchoule. John Wiley & Sons, 1999. 420 pp.

[11] F. Verheest. *Waves in Dusty Space Plasmas*. Springer Netherlands, 2000. DOI: 10.1007/978-94-010-9945-5.

[12] P. K. Shukla and A. A. Mamun. *Introduction to dusty plasma physics*. Bristol: Institute of Physics Publ., Bristol, 2002.

[13] P. M. Bellan. *Fundamentals of Plasma Physics*. Cambridge University Press, 2006. DOI: 10.1017/CBO9780511807183.

[14] A. Piel. *Plasma Physics: An Introduction to Laboratory, Space, and Fusion Plasmas*. Springer, Cham, 2017. DOI: 10.1007/978-3-319-63427-2.

[15] J. H. Chu and L. I. "Direct observation of Coulomb crystals and liquids in strongly coupled rf dusty plasmas". In: *Phys. Rev. Lett.* **72** 25 (1994), pp. 4009–4012. DOI: 10.1103/PhysRevLett.72.4009.

[16] H. Thomas, G. E. Morfill, V. Demmel, J. Goree, B. Feuerbacher, and D. Möhlmann. "Plasma Crystal: Coulomb Crystallization in a Dusty Plasma". In: *Phys. Rev. Lett.* **73** 5 (1994), pp. 652–655. DOI: 10.1103/PhysRevLett.73.652.

[17] Y. Hayashi and K. Tachibana. "Observation of Coulomb crystal formation from carbon particles grown in a methane plasma". In: *Jpn. J. Appl. Phys.* **33** (1994), p. L804. DOI: 10.1143/JJAP.33.L804.

[18] A. Melzer, T. Trottenberg, and A. Piel. "Experimental determination of the charge on dust particles forming Coulomb lattices". In: *Phys. Lett. A* **191** 3 (1994), pp. 301 –308. DOI: 10.1016/0375-9601(94)90144-9.

[19] T. Trottenberg, A. Melzer, and A. Piel. "Measurement of the electric charge on particulates forming Coulomb crystals in the sheath of a radiofrequency plasma". In: *Plasma Sources Sci. Technol.* **4** 3 (1995), p. 450. DOI: 10.1088/0963-0252/4/3/015.

[20] A. Homann, A. Melzer, and A. Piel. "Measuring the charge on single particles by laser-excited resonances in plasma crystals". In: *Phys. Rev. E* **59** 4 (1999), R3835–R3838. DOI: 10.1103/PhysRevE.59.R3835.

[21] J. Carstensen, H. Jung, F. Greiner, and A. Piel. "Mass changes of microparticles in a plasma observed by a phase-resolved resonance method". In: *Phys. Plasmas* **18** 3 (2011), p. 033701. DOI: 10.1063/1.3556677.

[22] V. Nosenko, J. Goree, Z. W. Ma, and A. Piel. "Observation of Shear-Wave Mach Cones in a 2D Dusty-Plasma Crystal". In: *Phys. Rev. Lett.* **88** 13 (2002), p. 135001. DOI: 10.1103/PhysRevLett.88.135001.

[23] S. Nunomura, J. Goree, S. Hu, X. Wang, and A. Bhattacharjee. "Dispersion relations of longitudinal and transverse waves in two-dimensional screened Coulomb crystals". In: *Phys. Rev. E* **65** 6 (2002), p. 066402. DOI: 10.1103/PhysRevE.65.066402.

[24] S. Nunomura, J. Goree, S. Hu, X. Wang, A. Bhattacharjee, and K. Avinash. "Phonon Spectrum in a Plasma Crystal". In: *Phys. Rev. Lett.* **89** 3 (2002), p. 035001. DOI: 10.1103/PhysRevLett.89.035001.

[25] K. Qiao, J. Kong, E. V. Oeveren, L. S. Matthews, and T. W. Hyde. "Mode couplings and resonance instabilities in dust clusters". In: *Phys. Rev. E* **88** 4 (2013), p. 043103. DOI: 10.1103/PhysRevE.88.043103.

[26] O. Havnes, C. K. Goertz, G. E. Morfill, E. Grün, and W. Ip. "Dust charges, cloud potential, and instabilities in a dust cloud embedded in a plasma". In: *J. Geophys. Res. Space Phys.* **92** A3 (1987), pp. 2281–2287. DOI: 10.1029/JA092iA03p02281.

[27] B. Tadsen, F. Greiner, and A. Piel. "On the amplitude of dust-density waves in inhomogeneous dusty plasmas". In: *Phys. Plasmas* **24** 3 (2017), p. 033704. DOI: 10.1063/1.4977901.

[28] F. Greiner et al. "Diagnostics and characterization of nanodust and nanodusty plasmas". In: *Eur. Phys. J. D* **72** 5 (2018). DOI: 10.1140/epjd/e2017-80400-7.

[29] B. Tadsen, F. Greiner, S. Groth, and A. Piel. "Self-excited dust-acoustic waves in an electron-depleted nanodusty plasma". In: *Phys. Plasmas* **22** 11, 113701 (2015). DOI: 10.1063/1.4934927.

[30] R. L. Heinisch, F. X. Bronold, and H. Fehske. "Mie Scattering by a Charged Dielectric Particle". In: *Phys. Rev. Lett.* **109** 24 (2012), p. 243903. DOI: 10.1103/PhysRevLett.109.243903.

[31] R. L. Heinisch, F. X. Bronold, and H. Fehske. "Optical signatures of the charge of a dielectric particle in a plasma". In: *Phys. Rev. E* **88** 2 (2013), p. 023109. DOI: 10.1103/PhysRevE.88.023109.

[32] B. Liu, J. Goree, V. Nosenko, and L. Boufendi. "Radiation pressure and gas drag forces on a melamine-formaldehyde microsphere in a dusty plasma". In: *Phys. Plasmas* **10** 1 (2003), pp. 9–20. DOI: 10.1063/1.1526701.

[33] J. Pavlu, A. Velyhan, I. Richterova, Z. Nemecek, J. Safrankova, I. Cermak, and P. Zilavy. "Mass-loss rate for MF resin microspheres". In: *IEEE Trans. Plasma Sci.* **32** 2 (2004), pp. 704–708. DOI: 10.1109/TPS.2004.826120.

[34] L. Schepers, J. Beckers, and W. IJzerman. "Determination of microparticle characteristics in an etching plasma". In: *Contrib. Plasma Phys.* **58** 10 (2018), pp. 985–994. DOI: 10.1002/ctpp.201700217.

[35] C. Killer, M. Mulsow, and A. Melzer. "Spatio-temporal evolution of the dust particle size distribution in dusty argon rf plasmas". In: *Plasma Sources Sci. Technol.* **24** (2015), p. 025029. DOI: 10.1088/0963-0252/24/2/025029.

[36] N. Kohlmann, F. Wieben, O. H. Asnaz, D. Block, and F. Greiner. "High-precision in-situ size measurements of single microparticles in an RF plasma". In: *Phys. Plasmas* **26** 5 (2019), p. 053701. DOI: 10.1063/1.5091097.

[37] S. Weiss, K. Urdl, H. A. Mayer, E. M. Zikulnig-Rusch, and A. Kandelbauer. "IR spectroscopy: Suitable method for determination of curing degree and crosslinking type in melamine–formaldehyde resins". In: *J. Appl. Polym. Sci.* **136** 25 (2019), p. 47691. DOI: 10.1002/app.47691.

[38] S. Weiss, R. Seidl, W. Kessler, R. W. Kessler, E. M. Zikulnig-Rusch, and A. Kandelbauer. "Unravelling the Phases of Melamine Formaldehyde Resin Cure by Infrared Spectroscopy (FTIR) and Multivariate Curve Resolution (MCR)". In: *Polymers* **12** 11 (2020). DOI: 10.3390/polym12112569.

[39] U. Konopka, D. Samsonov, A. V. Ivlev, J. Goree, V. Steinberg, and G. E. Morfill. "Rigid and differential plasma crystal rotation induced by magnetic fields". In: *Phys. Rev. E* **61** 2 (2000), pp. 1890–1898. DOI: 10.1103/PhysRevE.61.1890.

[40] E. Thomas Jr., R. L. Merlino and M. Rosenberg. "Magnetized dusty plasmas: the next frontier for complex plasma research". In: *Plasma Phys. Control. Fusion* **54** 12 (2012), p. 124034. DOI: 10.1088/0741-3335/54/12/124034.

[41] M. Choudhary, R. Bergert, S. Mitic, and M. H. Thoma. "Three-dimensional dusty plasma in a strong magnetic field: Observation of rotating dust tori". In: *Phys. Plasmas* **27** 6 (2020), p. 063701. DOI: 10.1063/5.0004842.

[42] D. Block and A. Melzer. "Dusty (complex) plasmas—routes towards magnetized and polydisperse systems". In: *J. Phys. B: At., Mol. Opt. Phys.* **52** 6 (2019), p. 063001. DOI: 10.1088/1361-6455/ab023f.

[43] V. A. Schweigert and F. M. Peeters. "Spectral properties of classical two-dimensional clusters". In: *Phys. Rev. B* **51** 12 (1995), pp. 7700–7713. DOI: 10.1103/PhysRevB.51.7700.

[44] K. Nelissen, A. Matulis, B. Partoens, M. Kong, and F. M. Peeters. "Spectrum of classical two-dimensional Coulomb clusters". In: *Phys. Rev. E* **73** 1 (2006), p. 016607. DOI: 10.1103/PhysRevE.73.016607.

[45] M. Klindworth, A. Melzer, A. Piel, and V. A. Schweigert. "Laser-excited intershell rotation of finite Coulomb clusters in a dusty plasma". In: *Phys. Rev. B* **61** 12 (2000), pp. 8404–8410. DOI: 10.1103/PhysRevB.61.8404.

[46] A. Schella, M. Mulsow, A. Melzer, J. Schablinski, and D. Block. "From transport to disorder: Thermodynamic properties of finite dust clouds". In: *Phys. Rev. E* **87** 6 (2013), p. 063102. DOI: 10.1103/PhysRevE.87.063102.

[47] M. Mulsow and A. Melzer. "Experimental determination of phase transitions by means of configurational entropies in finite Yukawa balls". In: *Phys. Rev. E* **96** 5 (2017), p. 053202. DOI: 10.1103/PhysRevE.96.053202.

[48] I. Langmuir. "Oscillations in Ionized Gases". In: *Proc. Natl. Acad. Sci.* **14** 8 (1928), pp. 627–637. DOI: 10.1073/pnas.14.8.627.

[49] S. A. Khrapak et al. "Particle charge in the bulk of gas discharges". In: *Phys. Rev. E* **72** (2005), p. 016406. DOI: 10.1103/PhysRevE.72.016406.

[50] A. Melzer. *Physics of Dusty Plasmas: An Introduction*. Springer International Publishing, 2019. DOI: 10.1007/978-3-030-20260-6.

[51] J. E. Allen, R. L. F. Boyd, and P. Reynolds. "The Collection of Positive Ions by a Probe Immersed in a Plasma". In: *Proc. Phys. Soc. London, Sect. B* **70** 3 (1957), p. 297. DOI: 10.1088/0370-1301/70/3/303.

[52] H. M. Mott-Smith and I. Langmuir. "The Theory of Collectors in Gaseous Discharges". In: *Phys. Rev.* **28** 4 (1926), pp. 727–763. DOI: 10.1103/PhysRev.28.727.

[53] M. Lampe, R. Goswami, Z. Sternovsky, S. Robertson, V. Gavrishchaka, G. Ganguli, and G. Joyce. "Trapped ion effect on shielding, current flow, and charging of a small object in a plasma". In: *Phys. Plasmas* **10** 5 (2003), pp. 1500–1513. DOI: 10.1063/1.1562163.

[54] M. A. Lieberman and A. J. Lichtenberg. *Principles of Plasma Discharges and Materials Processing*. John Wiley & Sons, 2005. 794 pp.

[55] N. Meyer-Vernet. "Flip-flop of electric potential of dust grains in space". In: *Astron. Astrophys.* **105** 1 (1982), pp. 98–106.

[56] E. C. Whipple. "Potentials of surfaces in space". In: *Rep. Prog. Phys.* **44** 11 (1981), pp. 1197–1250. DOI: 10.1088/0034-4885/44/11/002.

[57] M. S. Barnes, J. H. Keller, J. C. Forster, J. A. O'Neill, and D. K. Coultas. "Transport of dust particles in glow-discharge plasmas". In: *Phys. Rev. Lett.* **68** 3 (1992), pp. 313–316. DOI: 10.1103/PhysRevLett.68.313.

[58] S. A. Khrapak, A. V. Ivlev, S. K. Zhdanov, and G. E. Morfill. "Hybrid approach to the ion drag force". In: *Phys. Plasmas* **12** 4 (2005), p. 042308. DOI: 10.1063/1.1867995.

[59] I. H. Hutchinson. "Collisionless ion drag force on a spherical grain". In: *Plasma Phys. Control. Fusion* **48** 2 (2006), pp. 185–202. DOI: 10.1088/0741-3335/48/2/002.

[60] P. S. Epstein. "On the Resistance Experienced by Spheres in their Motion through Gases". In: *Phys. Rev.* **23** 6 (1924), pp. 710–733. DOI: 10.1103/PhysRev.23.710.

[61] H. Vestner and L. Waldmann. "Generalized hydrodynamics of thermal transpiration, thermal force and friction force". In: *Phys. A* **86** 2 (1977), pp. 303–336. DOI: 10.1016/0378-4371(77)90033-4.

[62] A. Ashkin. "Acceleration and Trapping of Particles by Radiation Pressure". In: *Phys. Rev. Lett.* **24** 4 (1970), pp. 156–159. DOI: 10.1103/PhysRevLett.24.156.

[63] M. Schwabe, U. Konopka, P. Bandyopadhyay, and G. E. Morfill. "Pattern Formation in a Complex Plasma in High Magnetic Fields". In: *Phys. Rev. Lett.* **106** 21 (2011), p. 215004. DOI: 10.1103/PhysRevLett.106.215004.

[64] J. Carstensen, F. Greiner, and A. Piel. "Ion-Wake-Mediated Particle Interaction in a Magnetized-Plasma Flow". In: *Phys. Rev. Lett.* **109** 13 (2012), p. 135001. DOI: 10.1103/PhysRevLett.109.135001.

[65] B. Tadsen, F. Greiner, and A. Piel. "Preparation of magnetized nanodusty plasmas in a radio frequency-driven parallel-plate reactor". In: *Phys. Plasmas* **21** 10 (2014), p. 103704. DOI: 10.1063/1.4897169.

[66] E. Thomas, U. Konopka, D. Artis, B. Lynch, S. Leblanc, S. Adams, R. L. Merlino, and M. Rosenberg. "The magnetized dusty plasma experiment (MDPX)". In: *J. Plasma Phys.* **81** 2 (2015), p. 345810206. DOI: 10.1017/S0022377815000148.

[67] A. Melzer, H. Krüger, S. Schütt, and M. Mulsow. "Dust-density waves in radio-frequency discharges under magnetic fields". In: *Phys. Plasmas* **27** 3 (2020), p. 033704. DOI: 10.1063/1.5144591.

[68] A. Melzer, H. Krüger, D. Maier, and S. Schütt. "Physics of Magnetized Dusty Plasmas". In: *Rev. Mod. Plasma Phys.* **5** 1 (2021). DOI: 10.1007/s41614-021-00060-2.

[69] H. Kählert, A. Melzer, M. Puttscher, T. Ott, and M. Bonitz. "Magnetic field effects and waves in complex plasmas". In: *Eur. Phys. J. D* **72** 5 (2018). DOI: 10.1140/epjd/e2017-80409-x.

[70] P. K. Kaw, K. Nishikawa, and N. Sato. "Rotation in collisional strongly coupled dusty plasmas in a magnetic field". In: *Phys. Plasmas* **9** 2 (2002), pp. 387–390. DOI: 10.1063/1.1435367.

[71] J. Carstensen, F. Greiner, L.-J. Hou, H. Maurer, and A. Piel. "Effect of neutral gas motion on the rotation of dust clusters in an axial magnetic field". In: *Phys. Plasmas* **16** 1 (2009), p. 013702. DOI: 10.1063/1.3063059.

[72] J.-P. Joost, P. Ludwig, H. Kählert, C. Arran, and M. Bonitz. "Screened Coulomb potential in a flowing magnetized plasma". In: *Plasma Physics and Controlled Fusion* **57** 2 (2014), p. 025004. DOI: 10.1088/0741-3335/57/2/025004.

[73] W. J. Miloch, D. Darian, and M. Mortensen. "Wake potential of a dust particle in magnetised plasmas". In: *Physica Scripta* **92** 11 (2017), p. 114006. DOI: 10.1088/1402-4896/aa90a5.

[74] E. Thomas, U. Konopka, R. L. Merlino, and M. Rosenberg. "Initial measurements of two- and three-dimensional ordering, waves, and plasma filamentation in the Magnetized Dusty Plasma Experiment". In: *Phys. Plasmas* **23** 5 (2016), p. 055701. DOI: 10.1063/1.4943112.

[75] H. Jung, F. Greiner, A. Piel, and W. J. Miloch. "Experiments on wake structures behind a microparticle in a magnetized plasma flow". In: *Physics of Plasmas* **25** 7 (2018), p. 073703. DOI: 10.1063/1.5040838.

[76] E. Thomas, B. Lynch, U. Konopka, R. L. Merlino, and M. Rosenberg. "Observations of imposed ordered structures in a dusty plasma at high magnetic field". In: *Phys. Plasmas* **22** 3 (2015), p. 030701. DOI: 10.1063/1.4914089.

[77] E. Thomas, U. Konopka, B. Lynch, S. Adams, S. LeBlanc, R. L. Merlino, and M. Rosenberg. "Quasi-discrete particle motion in an externally imposed, ordered structure in a dusty plasma at high magnetic field". In: *Phys. Plasmas* **22** 11 (2015), p. 113708. DOI: 10.1063/1.4936244.

[78] R. H. Lyddane, R. G. Sachs, and E. Teller. "On the Polar Vibrations of Alkali Halides". In: *Phys. Rev.* **59** 8 (1941), pp. 673–676. DOI: 10.1103/PhysRev.59.673.

[79] W. G. Spitzer and D. A. Kleinman. "Infrared Lattice Bands of Quartz". In: *Phys. Rev.* **121** 5 (1961), pp. 1324–1335. DOI: 10.1103/PhysRev.121.1324.

[80] Y. D. Glinka and M. Jaroniec. "Shape-selective Raman scattering from surface phonon modes in aggregates of amorphous SiO2 nanoparticles". In: *J. Appl. Phys.* **82** 7 (1997), pp. 3499–3507. DOI: 10.1063/1.365667.

[81] M. I. Vexler, S. E. Tyaginov, and A. F. Shulekin. "Determination of the hole effective mass in thin silicon dioxide film by means of an analysis of characteristics of a MOS tunnel emitter transistor". In: *J Phys : Condens Matter* **17** 50 (2005), pp. 8057–8068. DOI: 10.1088/0953-8984/17/50/023.

[82] C. F. Bohren and A. J. Hunt. "Scattering of electromagnetic waves by a charged sphere". In: *Can. J. Phys.* **55** 21 (1977), pp. 1930–1935. DOI: 10.1139/p77-235.

[83] I. Bronshtein, K. Semendyayev, G. Musiol, and H. Mühlig. *Handbook of Mathematics*. Springer-Verlag Berlin Heidelberg, 2015. DOI: 10.1007/978-3-662-46221-8.

[84] G. Mie. "Beiträge zur Optik trüber Medien, speziell kolloidaler Metallösungen". In: *Ann. Phys. (Berlin)* **330** 3 (1908), pp. 377–445. DOI: 10.1002/andp.19083300302.

[85] C. F. Bohren and D. R. Huffman. *Absorption and Scattering of Light by Small Particles*. Wiley, New York, 1983.

[86] H. C. van de Hulst. *Light Scattering by Small Particles*. Dover Publications, Inc. New York, 1981.

[87] A. P. Amrute, Z. Łodziana, H. Schreyer, C. Weidenthaler, and F. Schüth. "High-surface-area corundum by mechanochemically induced phase transformation of boehmite". In: *Science* **366** 6464 (2019), pp. 485–489. DOI: 10.1126/science.aaw9377.

[88] M. Klindworth, O. Arp, and A. Piel. "Langmuir probe system for dusty plasmas under microgravity". In: *Rev. Sci. Instrum.* **78** 3, 033502 (2007). DOI: 10.1063/1.2714036.

[89] H. M. Thomas et al. "Complex plasma laboratory PK-3 Plus on the International Space Station". In: *New J. Phys.* **10** 3 (2008), p. 033036. DOI: 10.1088/1367-2630/10/3/033036.

[90] S. Groth, F. Greiner, B. Tadsen, and A. Piel. "Kinetic Mie ellipsometry to determine the time-resolved particle growth in nanodusty plasmas". In: *J Phys D: Appl Phys* **48** 46 (2015), p. 465203. DOI: 10.1088/0022-3727/48/46/465203.

[91] G. E. Morfill, H. M. Thomas, U. Konopka, H. Rothermel, M. Zuzic, A. Ivlev, and J. Goree. "Condensed Plasmas under Microgravity". In: *Phys. Rev. Lett.* **83** 8 (1999), pp. 1598–1601. DOI: 10.1103/PhysRevLett.83.1598.

[92] S. Kashu, E. Fuchita, T. Manabe, and C. Hayashi. "Deposition of ultra fine particles using a gas jet". In: *Jpn. J. Appl. Phys.* **23** 12A (1984), p. L910. DOI: 10.1143/JJAP.23.L910.

[93] D. To, R. Dave, X. Yin, and S. Sundaresan. "Deagglomeration of nanoparticle aggregates via rapid expansion of supercritical or high-pressure suspensions". In: *AIChE J.* **55** 11 (2009), pp. 2807–2826. DOI: 10.1002/aic.11887.

[94] H. Krüger, C. Killer, S. Schütt, and A. Melzer. "Characterization of injected aluminum oxide nanoparticle clouds in an rf discharge". In: *Plasma Sources Sci. Technol.* **27** 2 (2018), p. 025004. DOI: 10.1088/1361-6595/aaa7d5.

[95] P. R. Griffiths and J. A. de Haseth. *Fourier Transform Infrared Spectrometry*. John Wiley & Sons, Inc., 2007. DOI: 10.1002/047010631x.

[96] G. H. P. M. Swinkels, H. Kersten, H. Deutsch, and G. M. W. Kroesen. "Microcalorimetry of dust particles in a radio-frequency plasma". In: *J. Appl. Phys.* **88** 4 (2000), pp. 1747–1755. DOI: 10.1063/1.1302993.

[97] H. Krüger, E. Sündermann, and A. Melzer. "Investigation of the IR absorption of trapped MF particles in a dusty plasma". In: *Plasma Sources Sci. Technol.* **30** 10 (2021), p. 105005. DOI: 10.1088/1361-6595/ac1d33.

[98] Y. Feng, J. Goree, and B. Liu. "Accurate particle position measurement from images". In: *Rev. Sci. Instrum.* **78** 5 (2007), p. 053704. DOI: 10.1063/1.2735920.

[99] J. C. Crocker and D. G. Grier. "Methods of Digital Video Microscopy for Colloidal Studies". In: *Journal of Colloid and Interface Science* **179** 1 (1996), pp. 298–310. DOI: 10.1006/jcis.1996.0217.

[100] W.-T. Juan, Z.-H. Huang, J.-W. Hsu, Y.-J. Lai, and L. I. "Observation of dust Coulomb clusters in a plasma trap". In: *Phys. Rev. E* **58** 6 (1998), R6947–R6950. DOI: 10.1103/PhysRevE.58.R6947.

[101] A. Melzer, M. Klindworth, and A. Piel. "Normal Modes of 2D Finite Clusters in Complex Plasmas". In: *Phys. Rev. Lett.* **87** 11 (2001), p. 115002. DOI: 10.1103/PhysRevLett.87.115002.

[102] A. Melzer. "Mode spectra of thermally excited two-dimensional dust Coulomb clusters". In: *Phys. Rev. E* **67** 1 (2003), p. 016411. DOI: 10.1103/PhysRevE.67.016411.

[103] L. Couëdel, V. Nosenko, A. V. Ivlev, S. K. Zhdanov, H. M. Thomas, and G. E. Morfill. "Direct Observation of Mode-Coupling Instability in Two-Dimensional Plasma Crystals". In: *Phys. Rev. Lett.* **104** 19 (2010), p. 195001. DOI: 10.1103/PhysRevLett.104.195001.

[104] H. Krüger, E. Thiessen, F. X. Bronold, H. Fehske, and A. Melzer. "Charge measurement of SiO_2 nanoparticles in an rf plasma by ir absorption". In: *Phys. Rev. E* **104** 4 (2021), p. 045208. DOI: 10.1103/PhysRevE.104.045208.

[105] M. Klindworth, O. Arp, and A. Piel. "Langmuir probe diagnostics in the IMPF device and comparison with simulations and tracer particle experiments". In: *J Phys D: Appl Phys* **39** 6 (2006), p. 1095. DOI: 10.1088/0022-3727/39/6/015.

[106] S. Ratynskaia et al. "Experimental Determination of Dust-Particle Charge in a Discharge Plasma at Elevated Pressures". In: *Phys. Rev. Lett.* **93** 8 (2004), p. 085001. DOI: 10.1103/PhysRevLett.93.085001.

[107] Microparticles GmbH. Product information page. https://www.microparticles-shop.de/Fluorescent-Particles/Melamine-resin-fluorescent-particles/Melamine-resin-particles-Orange-fluorescent-MF-FluoOrange-Ex-Em-560-nm-584-nm:::7_42_19.html. retrieved 2021-06-02.

[108] O. H. Asnaz, H. Jung, F. Greiner, and A. Piel. "Size and density evolution of a single microparticle embedded in a plasma". In: *Phys. Plasmas* **24** 8 (2017), p. 083701. DOI: 10.1063/1.4986855.

[109] D. J. Merline, S. Vukusic, and A. A. Abdala. "Melamine formaldehyde: curing studies and reaction mechanism". In: *Polymer Journal* **45** 4 (2013), pp. 413–419. DOI: 10.1038/pj.2012.162.

[110] J. R. Jasperse, A. Kahan, J. N. Plendl, and S. S. Mitra. "Temperature Dependence of Infrared Dispersion in Ionic Crystals LiF and MgO". In: *Phys. Rev.* **146** 2 (1966), pp. 526–542. DOI: 10.1103/PhysRev.146.526.

[111] J. Coates. *Interpretation of Infrared Spectra, A Practical Approach*. American Cancer Society, 2006. DOI: 10.1002/9780470027318.a5606.

[112] N. Sato, G. Uchida, T. Kaneko, S. Shimizu, and S. Iizuka. "Dynamics of fine particles in magnetized plasmas". In: *Phys. Plasmas* **8** 5 (2001), pp. 1786–1790. DOI: 10.1063/1.1342229.

[113] S. V. Vladimirov and M. Nambu. "Attraction of charged particulates in plasmas with finite flows". In: *Phys. Rev. E* **52** 3 (1995), R2172–R2174. DOI: 10.1103/PhysRevE.52.R2172.

[114] M. Nambu, S. V. Vladimirov, and P. K. Shukla. "Attractive forces between charged particulates in plasmas". In: *Phys. Lett. A* **203** 1 (1995), pp. 40–42. DOI: 10.1016/0375-9601(95)00380-L.

[115] A. Melzer, H. Krüger, S. Schütt, and M. Mulsow. "Finite dust clusters under strong magnetic fields". In: *Phys. Plasmas* **26** 9 (2019), p. 093702. DOI: 10.1063/1.5116523.

[116] V. Nosenko, S. K. Zhdanov, A. V. Ivlev, C. A. Knapek, and G. E. Morfill. "2D Melting of Plasma Crystals: Equilibrium and Nonequilibrium Regimes". In: *Phys. Rev. Lett.* **103** 1 (2009), p. 015001. DOI: 10.1103/PhysRevLett.103.015001.

[117] A. Piel, F. Greiner, H. Jung, and W. J. Miloch. "Molecular dynamics simulations of wake structures behind a microparticle in a magnetized ion flow. I. Collisionless limit with cold ion beam". In: *Phys. Plasmas* **25** 8 (2018), p. 083702. DOI: 10.1063/1.5039587.

[118] A. Piel, H. Jung, and F. Greiner. "Molecular dynamics simulations of wake structures behind a microparticle in a magnetized ion flow. II. Effects of velocity spread and ion collisions". In: *Phys. Plasmas* **25** 8 (2018), p. 083703. DOI: 10.1063/1.5039606.

[119] D. Darian, W. J. Miloch, M. Mortensen, Y. Miyake, and H. Usui. "Numerical simulations of a dust grain in a flowing magnetized plasma". In: *Phys. Plasmas* **26** 4 (2019), p. 043701. DOI: 10.1063/1.5089631.

[120] A. Melzer, M. Himpel, H. Krüger, M. Mulsow, and S. Schütt. "Optical diagnostics of dusty plasmas". In: *Plasma Phys. Control. Fusion* **61** 1 (2018), p. 014029. DOI: 10.1088/1361-6587/aad652.

A Scientific Contributions

Publications in peer-reviewed journals

1. H. Krüger, C. Killer, S. Schütt, and A. Melzer. "Characterization of injected aluminum oxide nanoparticle clouds in an rf discharge". In: *Plasma Sources Sci. Technol.* **27** 2 (2018), p. 025004. DOI: 10.1088/1361-6595/aaa7d5.

2. F. Greiner, A. Melzer, B. Tadsen, S. Groth, C. Killer, F. Kirchschlager, F. Wieben, I. Pilch, H. Krüger, D. Block, A. Piel, and S. Wolf. "Diagnostics and characterization of nanodust and nanodusty plasmas". In: *Eur. Phys. J. D* **72** 5 (2018). DOI: 10.1140/epjd/e2017-80400-7.

3. A. Melzer, M. Himpel, H. Krüger, M. Mulsow, and S. Schütt. "Optical diagnostics of dusty plasmas". In: *Plasma Phys. Control. Fusion* **61** 1 (2018), p. 014029. DOI: 10.1088/1361-6587/aad652.

4. A. Melzer, H. Krüger, S. Schütt, and M. Mulsow. "Finite dust clusters under strong magnetic fields". In: *Phys. Plasmas* **26** 9 (2019), p. 093702. DOI: 10.1063/1.5116523.

5. A. Melzer, H. Krüger, S. Schütt, and M. Mulsow. "Dust-density waves in radio-frequency discharges under magnetic fields". In: *Phys. Plasmas* **27** 3 (2020), p. 033704. DOI: 10.1063/1.5144591.

6. H. Krüger, E. Sündermann, and A. Melzer. "Investigation of the IR absorption of trapped MF particles in a dusty plasma". In: *Plasma Sources Sci. Technol.* **30** 10 (2021), p. 105005. DOI: 10.1088/1361-6595/ac1d33.

7. H. Krüger, E. Thiessen, F. X. Bronold, H. Fehske, and A. Melzer. "Charge measurement of SiO_2 nanoparticles in an rf plasma by ir absorption". In: *Phys. Rev. E* **104** 4 (2021), p. 045208. DOI: 10.1103/PhysRevE.104.045208.

8. A. Melzer, H. Krüger, D. Maier, and S. Schütt. "Physics of Magnetized Dusty Plasmas". In: *Rev. Mod. Plasma Phys.* **5** 1 (2021). DOI: 10.1007/s41614-021-00060-2.

Oral presentations at Conferences

1. Harald Krüger and André Melzer. Size, density and charge analysis of Al_2O_3 nanoparticles in argon discharges. *DPG Spring Meeting*, München (2019).

2. Harald Krüger and André Melzer. Charge measurement of SiO_2 nanoparticles in an RF-plasma by IR absorption. *virtual DPG Meeting*, online (2021).

Poster presentations at Workshops and Conferences

1. Harald Krüger, Carsten Killer und André Melzer. Einbringung und Untersuchung von Nanopartikeln in RF-Entladungen. *DPG Spring Meeting*, Hannover (2016).

2. Harald Krüger and André Melzer. Optical Charge Analysis of Nanoparticles in RF Discharges. *DPG Spring Meeting*, Bremen (2017).

3. Harald Krüger and André Melzer. Trapping and Charging of Aluminum Oxide Nanoparticles in RF Discharges. *8th International Conference on the Physics of Dusty Plasmas*, Praha (2017).

4. Harald Krüger and André Melzer. Diagnostics of Nanodusty Plasmas: Size, Density and charge analysis. *Bad Honnef School on Physics of Strongly Coupled Systems*, Bad Honnef (2019).

5. Harald Krüger and André Melzer. Characterization of Aluminum Oxide Nanoparticle Clouds in an RF Discharge *46th EPS Conference on Plasma Physics*, Milano (2019).